March 2018

A Study of Potential Organometallic Photosensitizers for TiO2 Using Density Functional Theory

Gillian Ceridwen Colman
Worcester Polytechnic Institute

Peter L. Melendez
Worcester Polytechnic Institute

A Study of Potential Organometallic Photosensitizers for TiO_2 Using Density Functional Theory

A Major Qualifying Project
submitted to the Faculty of
WORCESTER POLYTECHNIC INSTITUTE
in partial fulfillment of the requirements for the
degree of Bachelor of Science

by

Gillian Colman

Peter Melendez

Date:
20 March 2018

Approved by:

_____
Professor Aaron Deskins, Advisor

Table of Contents

Table of Figures

Table of Tables

Abstract

Sunlight is ubiquitous and reliable. Photocatalysis is a promising use for it, with many environmental benefits. One issue with titanium dioxide, a desirable photocatalyst, is an inability to absorb visible light. Attaching organometallics to titanium dioxide may improve photoexcitation. We used density functional theory to model an anatase surface and adsorbates. Our results indicate that carbonyl, as in iron pentacarbonyl and chromium hexacarbonyl, binds poorly to anatase. Halides such as in iron(II) tricarbonyl dibromide improve bonding and reduce required photoexcitation energy. Cyanide, as in tetracyanonickelate and tetracyanopalladate, has greater potential, reducing required energy further. Our results also indicate photocatalysis can be fine-tuned through choice of metal center.

Executive Summary

As recently as 2015, around 81.4%, of the world's energy is produced from abundant fossil fuels (1). Although other sources of energy are currently under development, the most powerful and steady source remains solar energy. If all light at ground level could be absorbed and converted to energy, a solar panel one and a half square meters in size could power an American home (2). One other possibility for capturing and harnessing light is using the energy to drive a chemical reaction in a process called photocatalysis, demonstrated in Figure i (3).

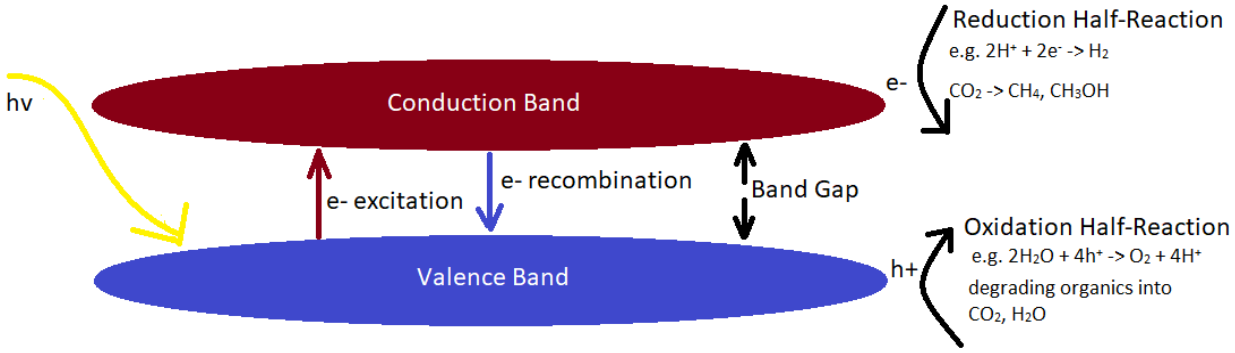

Figure i: Once sunlight of sufficient energy strikes an electron, it is excited to the conduction band (blue arrow). This photoexcited electron (e-) might recombine with a hole (h+) in an undesired process (red arrow). The excited electrons and holes may transfer to molecules or atoms, to reduce or oxidize them.

One major issue faced in photocatalytic processes is finding the correct material to receive light. The potential of a material as a photocatalyst is generally dictated by its unique band gap, the energy cost for an electron to move from the valence band into the conduction band. Due to its inexpensive and durable nature, titanium dioxide is considered to be an ideal candidate for photocatalysis; however, its large band gap prohibits all but ultraviolet light from causing electron excitation. To enable titanium dioxide as a powerful photocatalyst, the band gap must be reduced so more abundant visible light can cause photoexcitation (4).

The goal of our project was to identify organometallic materials that could potentially be used as photosensitizers, which decrease the band gap by providing other bands for electrons to jump to when excited. We used a program called the Vienna ab initio Simulations Package (VASP), which uses a theory called density functional theory (DFT), to predict molecular and electronic structures, and the ability of these organometallic materials to bind with titanium dioxide was determined, as well as their effectiveness as photosensitizers.

We determined and tested potential organometallic photosensitizers with three objectives:

1. To accurately model the properties of TiO_2, such as the band gap and electron energies
2. To simulate a number of potential organometallic compounds and ensure our results agree with literature results
3. To determine which compounds could be optimal photosensitive materials

The first objective focused on generating an accurate model of titanium dioxide. We determined lattice parameters for bulk titanium dioxide as $a = 3.81$ Å and $c = 9.51$ Å, exceptionally close to the literature values of $a = 3.78$ Å and $c = 9.51$ Å (5). We used VASP to calculate the electronic structure, or density of states, which includes the band gap, of both forms of titanium dioxide. Our bulk titanium dioxide calculation indicated that the band gap was 2.80 eV, lower than the literature accepted values of 3.0 - 3.2 eV (6), but fairly close. When converting from the bulk titanium dioxide into the anatase slab, we determined the surface energy to be 0.38 J/m^2, close to the literature 0.49 J/m^2 (7). The thin nature of the anatase slab reduced the band gap to 2.58 eV, as well, indicating that our results would not predict the actual band gap well, but could still be used to determine relative effectiveness of photosensitizers.

The second objective began with modeling several organometallic compounds in gas phase. Compounds such as ferrocyanide, a known photosensitizer, as well as others such as chromium hexacarbonyl and tetracyanonickelate, were modeled. For seventeen organometallic molecules, we calculated optimized geometries and electronic density of states using VASP. For many of these molecules bond lengths and HOMO-LUMO gaps were very close to literature values. We chose seven of those molecules, including chromium hexacarbonyl, iron pentacarbonyl, iron(II) tricarbonyl diiodide, iron(II) tricarbonyl dibromide, nickel tetracarbonyl, tetracyanonickelate, and tetracyanopalladate, which we then adsorbed to the titanium dioxide surface, and calculated the combined energy and electronic density of states.

Our third objective involved assessing potential photosensitizers when adsorbed to titanium dioxide, or the anatase (101) surface. Several geometries were tested for each molecule, and the most energetically favorable was determined for each molecule studied. Iron(II) tricarbonyl dibromide, for instance, was found to twist into an octahedral geometry so the iron atom could bond to an oxygen atom on titanium dioxide (see Figure ii). This Fe-O bond has a length of 2.25 Å and binding energy of 0.59 eV, which could hold the molecule to the surface with reasonable strength.

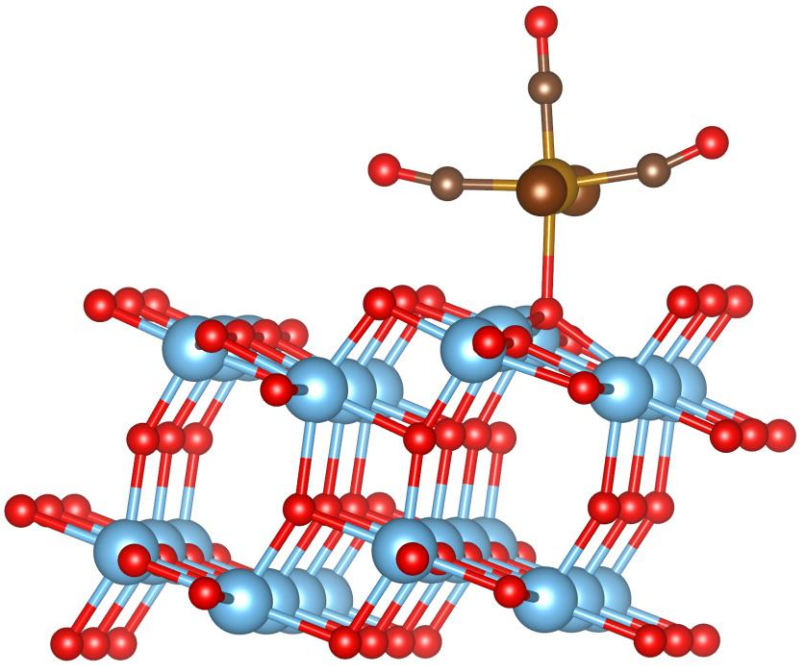

Figure ii: Iron(II) tricarbonyl dibromide's best bonding geometry with titanium dioxide.

Among the molecules studied, most formed a molecular geometry that created a ligand-to-surface bond in a bidentate fashion to allow for the most ligand-to-surface contact, such as in octahedral chromium hexacarbonyl and square planar tetracyanonickelate and tetracyanopalladate. The trigonal bipyramidal geometry of iron pentacarbonyl and tetrahedral geometry of nickel tetracarbonyl only had stable monodentate bonds. Iron(II) tricarbonyl diiodide bound metal-to-surface in the same way as iron(II) tricarbonyl dibromide, but with significantly lower binding energy, likely due to the size of the iodide atoms. Ligands determined the strength and distance of bonds; carbonyl groups bonded around 2.50 Å away and with less than 0.25 eV of energy, while cyanide groups bonded closer, about 2.15 Å away.

As an example, the electronic density of states for iron(II) tricarbonyl dibromide showed that it has some promise as a photosensitizer. The gap between the highest occupied molecular orbital (HOMO) and lowest unoccupied molecular orbital (LUMO) of $Fe(CO)_3Br_2$ is significantly smaller than that of titanium dioxide at 1.83 eV (see Figure iii). This indicates that $Fe(CO)_3Br_2$ provides electron states that make photoexcitation significantly easier, as light of lower energy is capable of exciting electrons. Of the molecules studied, iron(II) tricarbonyl dibromide was the most promising as a photosensitizer due to both a fairly strong bond and significantly reduced band gap.

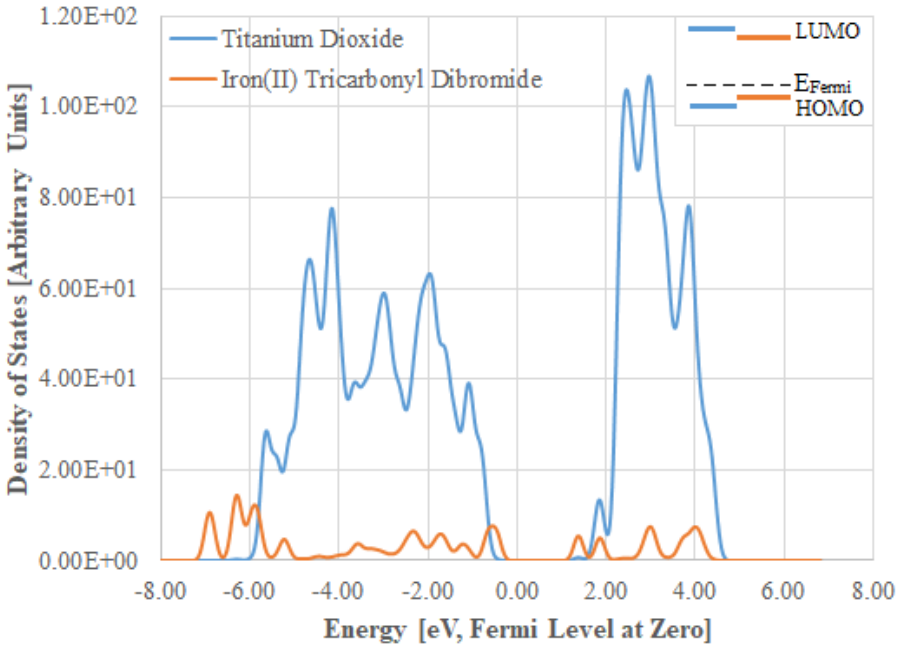

Figure iii: Calculated density of states for iron(II) tricarbonyl dibromide adsorbed to the titanium dioxide surface. State contributions from titanium dioxide are shown in blue, while contributions from iron(II) tricarbonyl dibromide are shown in orange.

Among the molecules studied, there is little correlation between the molecule's geometry (e.g. octahedral, tetrahedral, etc.) and the electronic density of states upon adsorption. Chromium hexacarbonyl, iron pentacarbonyl, and nickel tetracarbonyl all provided no benefit for photoexcitation since they required more energy for electrons to jump from their HOMO to their LUMO or the LUMO of TiO_2 than from the HOMO of TiO_2 to the LUMO of TiO_2. On the other hand, iron(II) tricarbonyl diiodide provided an even smaller band gap than iron(II) tricarbonyl dibromide at 1.53 eV, although its inability to bond to the surface well (binding energy of 0.16 eV) hinders its potential as a photosensitizer. Tetracyanonickelate provided a yet smaller gap at 1.03 eV, tetracyanopalladate reduced the gap to 0.50 eV, and hexacyanotitanate provided a larger band gap of 2.07 eV. How strongly molecules with cyanide ligands, such as these, bonded to the surface could not be determined due to a known issue with VASP introducing an error into the total energy of charged systems (8). This error can be minimized by increasing the size of the unit cell, such as increasing the size of the vacuum above the adsorbate.

We found multiple general trends about how these organometallic molecules act as photosensitizers. For instance, carbonyl groups bonded poorly to the anatase surface and provided no useful benefits for photoexcitation. On the other hand, halides are a promising choice to induce photoexcitation, often generating a smaller band gap than naturally found in anatase. Iodine is a superior photosensitizer to bromine, as it generates a yet smaller band gap, but it does not bond as well to the surface, so it is overall a poorer choice than bromine. The ionic nature of halides may contribute to their photosensitization benefits. We could not determine how well cyanide groups bonded to the surface due to the previously mentioned error inherent in charged surface

calculations (8). Two of the three molecules involving cyanide groups, tetracyanonickelate and tetracyanopalladate, provided strong benefits for photosensitization.

In conclusion, our work suggests that cyanide and other charged ligands such as bromine and iodine are very promising ligands for organometallic photosensitization. The success of bromine in an iron-titanium bond indicates they form decently strong bonds with the anatase surface, as well. Furthermore, choice of metal can greatly influence the light energy required for photosensitization; comparison of molecules indicates palladium is a more effective photosensitizer than nickel or titanium. On the other hand, carbonyl and neutrally charged ligands are less likely to be useful photosensitizers, and do not bond to the anatase surface well. Therefore, further research into organometallic photosensitization should focus on comparison of metals and use of charged ligands.

1 Introduction & Background

1.1 The Current Energy Landscape

1.1.1 Current Energy Usage

The modern world is dominated by the need for energy. According to the International Energy Agency in a report published in 2017, the world consumed 110,000 terawatt-hours of power in 2015, and this number has only grown. In 2015, 31.7% of the world's power was produced from oil, 21.6% from natural gas, and 28.1% from coal. These fuels are used because they are plentiful and easy to extract; the same report indicates 4,321 metric tons of crude oil were produced in 2016 (1).

Because fossil fuels produce electricity by combustion, they release harmful pollutants into the air. Industrial-level combustion reactions release a myriad of harmful chemicals into the atmosphere including chlorinated hydrocarbons, organosulfur compounds, dioxins, furans, and even carcinogens such as derivatives of benzene. Nearly 33,000 megatons of carbon dioxide were also produced in 2015 (1). Carbon dioxide is a greenhouse gas, trapping heat from solar radiation in the atmosphere, and contributing to global climate change. While other pollutants are released in relatively low concentration, they can cause a number of health problems in humans from skin disorders to cancer and render water and food supplies poisonous for animal and plant alike (9).

Alternatives such as nuclear, hydro, and biofuels are also fairly significant sources of power in the modern world. In 2015, nuclear power, extracted from the fission of heavy atoms, accounted for 4.9% of power generation across the world. Hydro power, generated from the momentum of flowing water, made up an additional 2.5% of power generation. Biofuels such as biodiesel and ethanol accounted for 9.8%. Other sources of power, including geothermal, wind, and solar power, only produced 1.5% of the global total, but this amount is increasing. In 2017, 55% of new power generation was from renewable energy sources (10). Nevertheless, these sources pale in comparison to the abundance of fossil fuels, which continue to provide 81.4% of power worldwide (1). One source of energy that remains abundant and avoids pollution is solar radiation. Solar energy use is increasing, but it still has much potential for growth.

1.2 Solar Energy

1.2.1 Abundance of Solar Energy

The sun is potentially one of the strongest, most reliable sources of energy available. About 1000 maximum watts of light energy reach the Earth's surface per square meter. If all of this light could be harnessed as energy, a solar panel one and a half square meters in size would be more than sufficient to power an average American home (2). This amount varies due to the curvature

of the Earth; the poles receive about a fifth as much energy (11). Regardless, the flow of energy from sunlight is still usually steady and reliable (12).

Efficient ways to capture energy from the sun could push the world toward energy stability and independence from fossil fuels. While the most effective photovoltaic panels were about 15% efficient just a few years ago (13), newer panels can be as efficient as 22.5% (14). As technologies for capturing solar power become more effective and energy efficient, solar energy in turn becomes a more attractive, reliable, and flexible option. Using solar energy to make chemicals is also a promising way to utilize solar energy.

1.2.2 Current Uses of Solar Energy

Solar power is useful in a wide array of applications today. Solar panels absorb light to generate electricity. This technology is constantly improving and becoming cheaper, but currently is not especially efficient (14). Absorbed light can also be used to store heat in water, powering both water-based heating systems or adsorption chiller cooling systems. Systems that provide both space or water heating have efficiencies ranging anywhere from 10-60%. While solar panels and assemblies can be quite large compared to the amount of energy generated, they can also be positioned on roofs and walls, allowing excellent collection while creatively using real estate (15). Photocatalysis can also be used to generate chemicals and fuels. Photocatalysis enables a reaction where light provides energy, driving the chemical reaction.

1.2.3 Potential of Photocatalysis

Solar energy is abundant and delivers plentiful light and heat to the earth, but it is intermittent, only available during certain times or weather conditions. Using energy from sunlight to synthesize chemicals could enable long-term utilization of solar energy. Converting the energy to matter, or chemical bonds, through photocatalysis can be a powerful way to efficiently store energy for transportation and later consumption. For instance, oil is one of the most used energy sources because it can be transported and stored easily with negligible energy losses (16); electricity, on the other hand, can lose power during storage and transit. Photocatalyzed reactions, such as the reduction of CO_2 into alcohol or hydrocarbon products, create renewable fuels from plentiful resources without harm to the environment (4).

1.3 Photocatalysis

1.3.1 What is Catalysis?

The IUPAC Compendium of Chemical Terminology states that a catalyst is any substance that increases the rate of a chemical reaction without modifying the overall standard Gibbs energy change (17). This means that a catalyst facilitates a chemical reaction but is neither consumed nor produced. The alternative pathway a catalyst provides in a reaction lowers the activation energy required without changing the end products (see Figure 1).

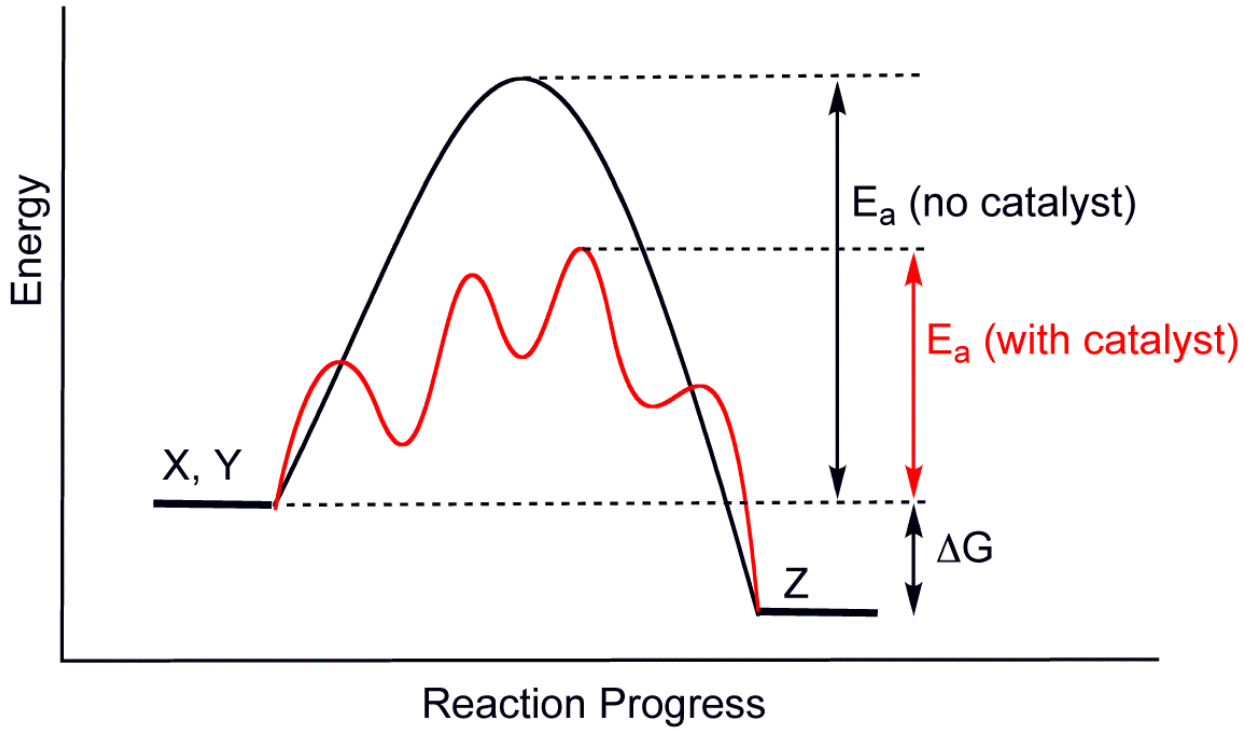

Figure 1: A demonstration of how a catalyst makes a reaction possible with a lower activation energy. As the reaction proceeds an energy barrier must be overcome to form products. A catalyst lowers this energy barrier through an alternative chemical pathway. Lower activation energy leads to a faster reaction (18).

In Figure 1, the reaction X + Y -> Z is considered; the standard Gibbs energy change is given by ΔG. In the standard reaction, X and Y might simply collide and react, but this interaction requires a relatively high energy to overcome the bonds and electromagnetic forces preventing this exchange. The addition of a catalyst, however, provides favorable conditions lowering the activation energy (E_a) required. Due to these conditions, more molecules of X and Y have enough energy to undergo the reaction, and the rate increases. Notably, however, the catalyst does not prevent in itself the reverse reaction, Z -> X + Y. Other methods must be considered to avoid this back reaction if Z is the desired product (19).

1.3.2 Choosing Semiconductors for Photocatalysts

In attempting to catalyze a reaction using light, choosing the right catalyst is essential. W. J. Hehre describes the physics of light absorption and electron excitation in solid materials (20). Electrons orbiting an atom are normally bound to that atom, unable to transfer to other atoms. These electrons reside in a low-energy state called the valence band. When sufficiently energetic light strikes an electron, it can jump to a higher energy level called the conduction band, where it can move more or less freely through the substance. The minimum energy needed to move from the valence band to the conduction band is called the band gap (see Figure 2).

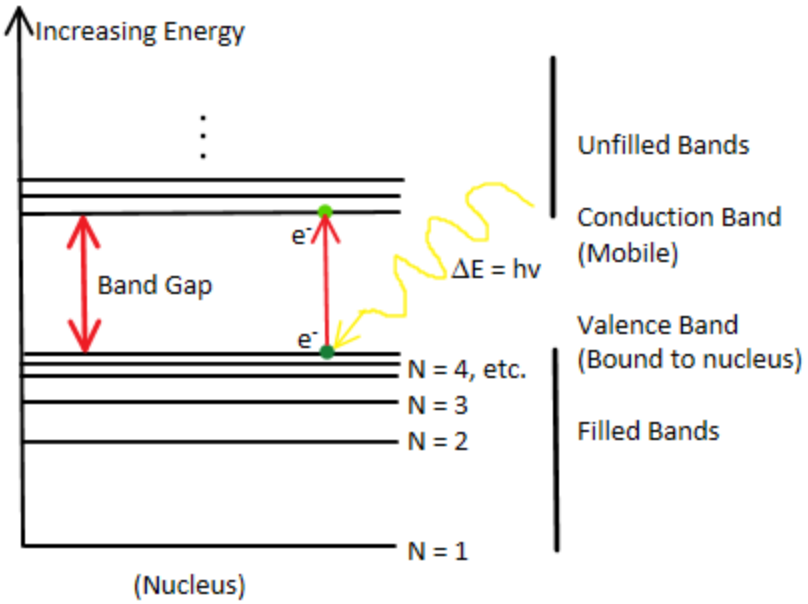

Figure 2: A demonstration of light absorption by an electron; the absorbed light excites the electron from the valence band into the conduction band.

Since an electron in the conduction band is mobile, it can migrate to the catalyst surface and participate in chemical reactions. Sometimes, however, the electron might relax to its previous energy level, emitting another photon or producing heat. With the exception of metals, each material has a unique band gap dictating the energy required for photoexcitation. Figure 3 demonstrates the different possibilities (21).

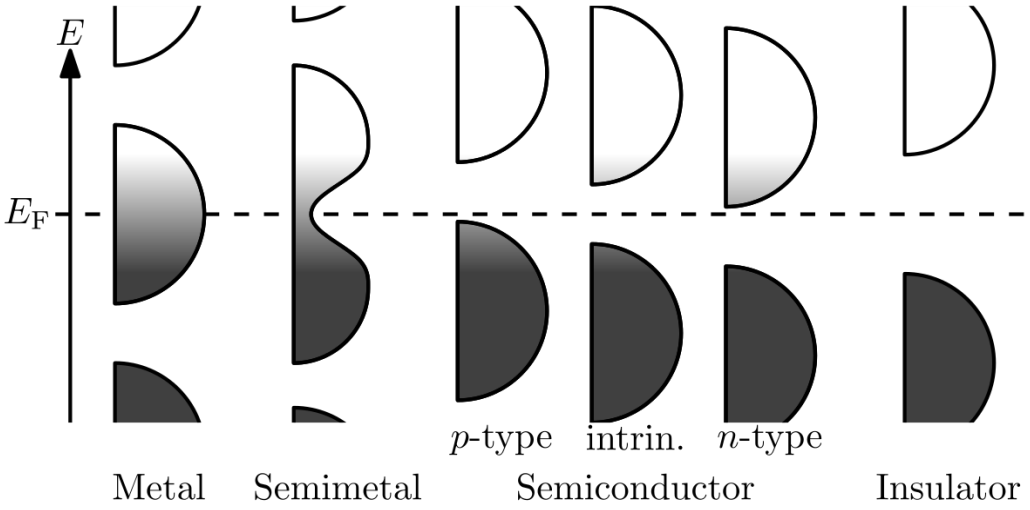

Figure 3: Demonstration of energy bands of different types of conductors; semicircular regions indicate available energy states for electrons. Dark regions indicate filled states at low temperature or ambient temperature. P-type and n-type semiconductors are doped with electron donors and acceptors, respectively, while intrinsic semiconductors are not doped (22).

The Fermi level (denoted by E_F in Figure 3) corresponds to a hypothetical energy level which has a 50% probability of being occupied at thermodynamic equilibrium. Occupied energy states in an unexcited atom are below the Fermi level at low temperatures. In semiconductors, the Fermi level lies between the valence band (below) and the conduction band (above). In the case of metals and semimetals, no band gap exists, so electrons routinely move between atoms (i.e. conduction). The high reflectivity of metals and semimetals leads to large reflection of light, making them unsuitable for light excitation. Insulators have a very large band gap and are also unsuitable for applications requiring light excitation, because light would need a large amount of energy to excite an electron across the gap (23).

1.3.3 How Photocatalysts Work

The basic mechanism by which photocatalysts enable a reaction is shown in Figure 4. An electron leaving its atom also creates a "hole," the now positively charged region the electron came from. Once free, the electron may recombine with the hole it created (the opposite of photoexcitation), or it can travel through the semiconductor. The hole can also "move" through the semiconductor by attracting electrons from other atoms, creating a new hole in the atom that donated the electron (3).

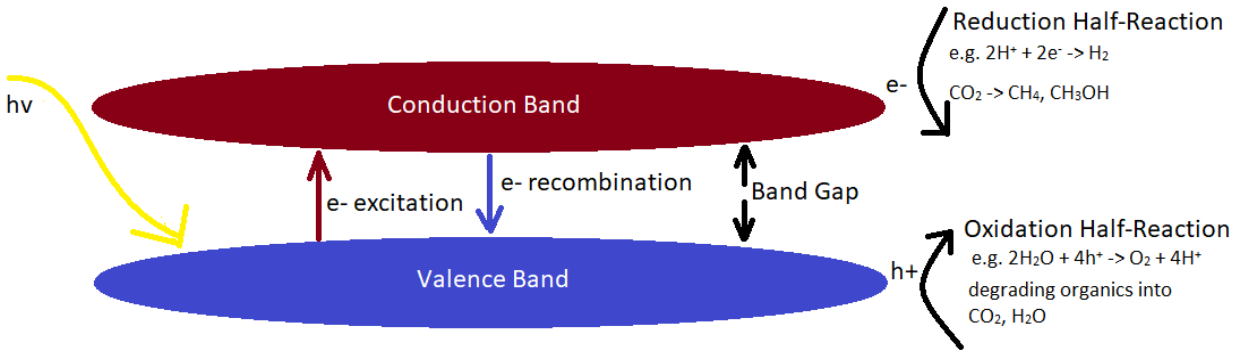

Figure 4: Once sunlight of sufficient energy strikes an electron, it is excited to the conduction band (red arrow). This photoexcited electron (e-) might recombine with a hole (h+) in an undesired process (blue arrow). The excited electrons and holes may transfer to molecules or atoms, to reduce or oxidize them.

When an electron or hole is at the surface of a semiconductor, it becomes available to catalyze reactions. Reactants such as carbon dioxide and water will occasionally attach to the surface of the photocatalyst. The electron can be captured by an oxidizing agent, such as carbon dioxide, and facilitate the reduction half of a reaction. Meanwhile, the hole can be captured by a reducing agent such as water and facilitate the oxidation half of a reaction.

The above figure demonstrates how the oxidation and reduction halves of a reaction can occur. In order to conserve charge, both halves of the reaction occur near-simultaneously. The reduction reaction removes the original electron while the hole is filled in the oxidation reaction, resulting in no net change in charge and regeneration of the catalyst. These reactions are potentially

very promising for a variety of applications; for instance, carbon dioxide and water could be catalyzed to produce methanol or other hydrocarbons as well as oxygen and hydrogen, giving us a sustainable fuel source from abundant materials and helping reduce pollution in the atmosphere.

1.3.4 Common Photocatalyst Materials and Reactions

A small number of semiconductor materials are frequently used in photocatalysis. For instance, metal oxides such as titanium dioxide and zinc oxide are good candidates as semiconductors due to their ease of production and overall stability (4, 25, 26, 27, 28). Titanium dioxide has a band gap of about 3.1 eV, allowing it to be excited by some violet and blue light, while zinc oxide has a band gap of nearly 3.4 eV, allowing it only to be excited by ultraviolet light. Silicon crystals are also used (29, 30, 31, 32), but their band gap is 1.1 eV, allowing it to be easily excited by visible light. However, silicon can react with water leading to photocatalyst deactivation, hindering its catalytic ability.

An often-sought use for photocatalysts is the ability to reduce carbon dioxide into heavier hydrocarbons, providing an excellent way to store solar energy while removing a greenhouse gas from the atmosphere (4, 33). Photocatalysts can also be used to produce fuel by splitting water into hydrogen and oxygen (34). Photocatalysts are also effective in decontamination processes such as dechlorinating organic pollutants in water (26, 35) or treating waste streams such as hydrogen sulfide (36).

1.3.5 Limitations of Current Photocatalysts

Several issues limit the use of semiconductors in photocatalysis. In most semiconductors, the band gap is so large that only ultraviolet light can excite electrons into the conduction band. Ultraviolet light accounts for a very small fraction of solar energy, limiting the number of electrons that are excited. Visible light, on the other hand, is much more abundant, and therefore preferable to use for photocatalysis (see Figure 5); however, it is often cannot excite electrons in most semiconductors alone such as TiO_2.

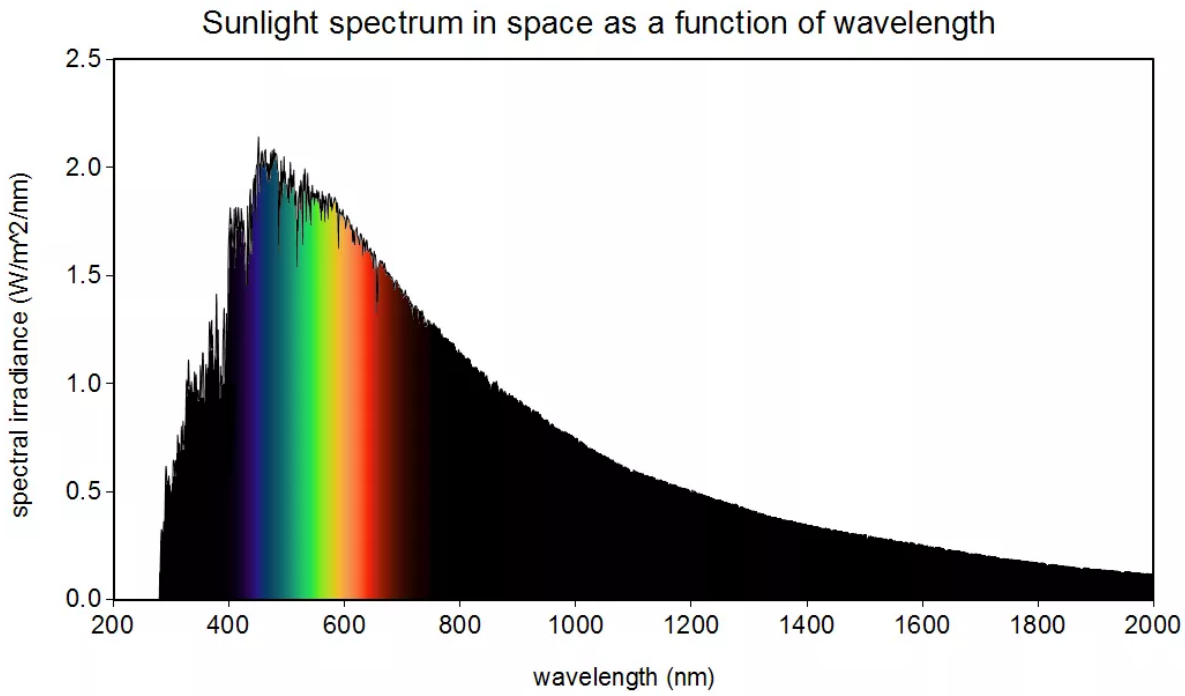

Figure 5: Natural light intensity versus wavelength of typical sunlight. Note that the visible spectrum (~400 nm to ~700 nm) is far more abundant than UV light (>400 nm) (37).

To access this visible light, a molecule called a photosensitizer may be added to the semiconductor. Photosensitizers often have large delocalized pi bonds, enabling them to absorb ultraviolet and visible light and easily transfer electrons or energy to another molecule. A photosensitizer that is added to the surface of a semiconductor can allow more excitation of electrons into the semiconductor's conduction band. Because photosensitizers are able to enable a greater absorption wavelength spectrum than a semiconductor alone, this leads to using more than just ultraviolet light being used (38, 39).

Several other issues hinder photocatalyst development. Firstly, photoexcited electrons often have a small lifespan, recombining easily with available holes. This limits the rate of reactions because few electrons reach the surface of the semiconductor. The use of photosensitizers produces more of these free electrons but does not directly combat their short life. Secondly, many of these photocatalytic reactions take place in aqueous solution, limiting the kinds of semiconductors that can be used. Crystals such as silicon, for instance, react with water, swiftly reducing the effectiveness of the photocatalyst. Photosensitizers can sometimes shield the semiconductor from reactions, but the effect may not be significant (19, 40).

1.4 Organometallic Functionalization

1.4.1 Why Organometallics?

Organometallic materials bound to the surface of semiconductors can act as photosensitizers, lowering the band gap of the semiconductor and increasing light absorption. Potentially, the band gap could be pushed into the visible spectrum of light, increasing the energy that can be harnessed. Anchoring an organometallic complex to the semiconductor therefore makes electrons more available (4, 31, 32, 41). As an example, one study (42) examined tricarbonyl rhenium complexes attached to the surface of silica through modelling. These complexes enhanced the ability of the semiconductor/photosensitizer to absorb light and provided a reaction site for the reduction of carbon dioxide.

1.4.2 Structure of Organometallic Compounds

Organometallic molecules consist of metal atoms bonded to a number of inorganic or organic molecules in a coordination complex (23) (see Figure 6). Transition organometallics are candidates for photosensitizers due to their wide range of electronic properties based on the metal and ligands. Since most transition metals have one s, three p, and five d orbitals in the valence level, these compounds attempt to bond to molecules, known as ligands, to fill these nine orbitals and reach 18 electrons. This phenomenon is known as the 18-electron rule. In some cases, ligands that are too large prevent the metal from bonding to molecules to completely fill these orbitals; in other cases, ligands contribute odd number of electrons that add up to 17, 19, or rarely 20 electrons. In these cases, the organometallic complex may attract or shed electrons in order to stabilize itself to a full 18 electrons (18, 43).

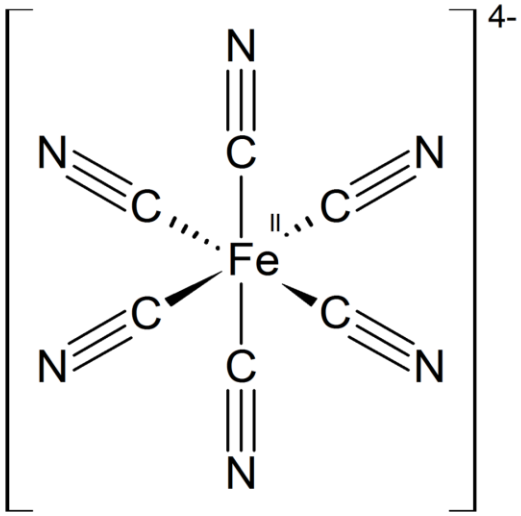

*Figure 6: Ferrocyanide, an organometallic complex ion used to make Prussian Blue dye. The iron atom contributes 6 valence electrons due to its +2 charge. Each cyanide molecule, which have a -1 charge, contributes 2 valence electrons, so the compound has (6 + 6*2) = 18 valence electrons. The net charge is -4 (44).*

Some examples of the many possible ligands include carbon monoxide, methyl and other carbon chains, carbon rings and aromatics, and even larger molecules such as bipyridyl (33). A given metal atom will react with anywhere from two to nine of these molecules, typically limited by the amount of space around the atom and the 18-electron rule. These structures usually have tetrahedral, square planar, trigonal bipyramidal, or octahedral geometries, but sometimes variations such as square pyramidal structures occur (23, 42).

In order to act as a strong photosensitizer, the organometallic molecule needs to be anchored well to the semiconductor. Many smaller ligands, including carbon monoxide and cyanide, can form a strong nucleophilic bond to a titanium atom in TiO_2, for instance, providing an anchor for the organometallic molecule (45). Rather than a simple conduction and valence band, the complex has a highest occupied molecular orbital (HOMO) and a lowest unoccupied molecular orbital (LUMO). Electron excitation caused by the presence of an organometallic molecule takes two major forms, called "dye" photosensitization and "direct" photosensitization. (see Figure 7).

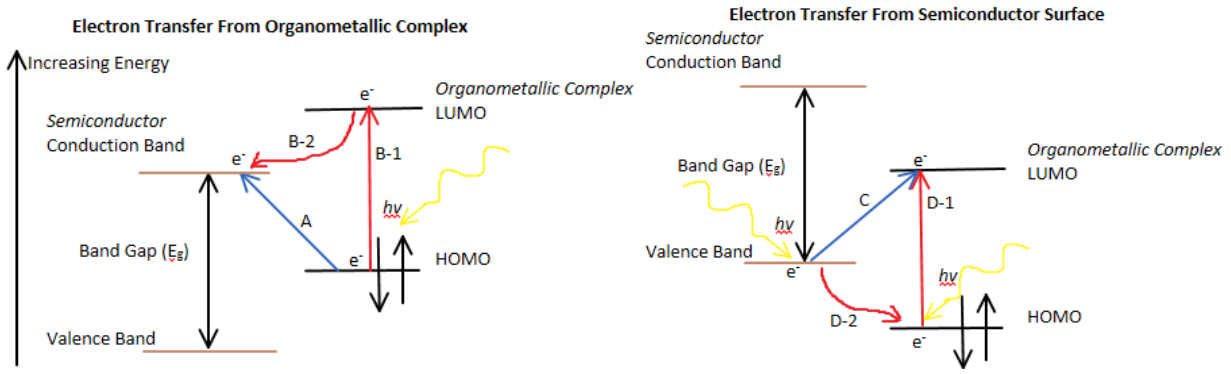

Figure 7: Demonstration of the types of photoexcitation in the presence of an organometallic complex. In general, lower energy bands are populated with electrons, while higher energy bands are mostly empty save for excited electrons. In the left schematic electrons can be excited from the HOMO level of the complex to the semiconductor conduction band (blue arrow) or from the HOMO to the LUMO level of the organometallic complex, and then transferred to the semiconductor conduction band (red arrows). In the right schematic electrons can be excited from the semiconductor valence band into the complex LUMO (blue arrow), or from the complex HOMO to LUMO (red arrow). If the there are holes in the complex, electrons can hop from the semiconductor valence band to the holes in the HOMO.

When light with enough energy strikes a HOMO electron, that electron may jump into the conduction band of the semiconductor in direct photosensitization (A in Figure 7). Alternatively, the light may excite that electron to the LUMO (B-1 in Figure 7), which then transfers to the semiconductor in dye sensitization (B-2 in Figure 7). This sequence is possible if the LUMO is higher energy than the conduction band in the semiconductor. This excitation relies on the HOMO and LUMO of the complex being close to the conduction band of the semiconductor, in a similar way that band gap influences photoexcitation. The opposite phenomena also may occur if the energy of the LUMO and HOMO are closer to the valence band of the semiconductor (Figure 7, right). A photoexcited electron from the valence band may be excited directly into the LUMO (C

in Figure 7), or an electron may be photoexcited from the organometallic HOMO to the LUMO (D-1 in Figure 7) and be replaced by one from the semiconductor (D-2 in Figure 7). Since this excitation can be simpler and require less energy than photoexcitation in the semiconductor alone, it may be useful for photocatalytic processes (45).

1.4.3 Relevant Organometallic Sensitizers

One interesting organometallic sensitizer is ferrocyanide, a low-spin iron(II) center with six cyanide molecules attached in an octahedral geometry (46). It is a diamagnetic species, meaning it is repelled by a magnetic field (46). Ferrocyanide is unlikely to release toxic cyanide ions during a reaction, making it relatively safe (46). Ferrocyanide is a powerful electron donor, allowing it to transfer its excited electrons into the titanium dioxide surface. This process is quick, avoiding electron recombination. Because of this ability ferrocyanide is often used on semiconductor surfaces to increase photoexcitation and increase the number of excited electrons. When ferrocyanide is used on a TiO_2 semiconductor, excited electrons within the complex can be transferred to the substrate surface in metal-to-particle charge transfer (47). In dye absorption ferrocyanide has been shown to be highly effective at lowering the band gap of a semiconductor/photosensitizer complex, as much as ~4.3 eV (47). It has also been shown to increase the efficiency of solar cells (48, 43).

In many cases ferricyanide can be used with or in place of ferrocyanide. Ferricyanide is very similar to ferrocyanide, but instead of having a central iron(II) atom, ferricyanide has a central iron(III) atom (49). Like ferrocyanide, ferricyanide has strong ionic bonds with its cyanide ligands, and is therefore relatively nontoxic. In previous experiments using ferricyanide and ferrocyanide together for absorption in a TiO_2 semiconductor has been shown to have a high charge transfer rate, thereby blocking hole recombination (47).

1.5 Density Functional Theory

1.5.1 The Schrödinger Equation

At the quantum, or small scale, the “normal” laws of physics cease to function, and the interactions of small particles, such as electrons, protons, or nuclei are best described by quantum mechanics. The Schrödinger equation is a mathematical equation that can be used to determine the wave function of a particle. The wave function is a mathematical function that describes a system of particles, and can, for instance, provide information on location probability or other properties. The Schrodinger equation has two different types, time-dependent and time-independent. In a time-dependent system, the particle in question is changing with time. For the purpose of this project, since we are interested in the most stable configurations, the time-independent Schrödinger equation, shown in Equation 1, was used (50).

$$\hat{\mathrm{H}}\,\Psi = E\,\Psi \tag{1}$$

In the general time-independent Schrödinger equation, Ψ represents the wave function of the particle in question, as a function of space. E is a proportionality constant, representing the energy associated with the wave function. $\hat{H}$ refers to the Hamiltonian operator, which is a mathematical operator used to determine the energy of a system. The Hamiltonian operator has two major parts: V, which represents the potential energy (e.g. electrostatic interactions between charged particles) of the system as a function of position, and $-(\hbar^2/2\mu)\nabla^2$, representing the kinetic energy of the system in space. $\hbar$ is the reduced Planck's constant, or Planck's constant divided by 2π ($h/2\pi$), μ is the mass of the particle under examination, and ∇^2 is the Laplace operator, or the sum of all second partial derivatives of the wavefunction (46). After expanding the Hamiltonian operator, we obtain a more detailed version of the time-independent Schrödinger equation as shown in Equation 2.

$$[-(h^2/2\mu)\nabla^2 + V(r)]\Psi(r) = E\,\Psi(r) \tag{2}$$

Analytical solutions of one-particle systems are known (51). However, the Schrödinger equation is impractical to solve analytically for complex systems with many electrons and nuclei. This is because the interactions between electrons add complex potential energy terms to the equation. In order to find an approximate solution for such a complex system a set of assumptions must be made to simplify the system (50).

1.5.2 Use of Density Functional Theory for a Many-Electron Problem

Density functional theory, or DFT, replaces a number of terms in the Schrödinger equation to allow computers to calculate energies and wavelengths for a complex system of atoms. Hohenberg and Kohn laid the groundwork for DFT by postulating two things. First, they postulated that the external potential energy caused by electron interactions, and therefore the total energy of the system was a unique value dependent solely on the electron density function; this meant that total energy was a functional of electron density since the electron density is a function. A functional returns a number when given a function, as opposed to a function which returns a number when given a number. Second, the correct electron density of the system at ground state would minimize the total energy. The electron density is a function of position, and the number of variables for electron density is only 3 - the cartesian position coordinates x, y, and z (52, 53).

Kohn and Sham used the previous work of Hohenberg and Kohn to create a set of equations relating the electron density and total energy of the system. An electron density guess can be used to calculate the potential energy of the system of electrons. This potential is used to calculate the one-particle Schrödinger equation for each electron, and the wave functions are then summed as a new electron density (see Figure 8). If the initial guess for electron density was incorrect, these steps can be repeated with better guesses and the electron density should converge to a ground state. The theory has difficulties when dispersion is a dominating force, which can lead to inaccuracy (54, 55).

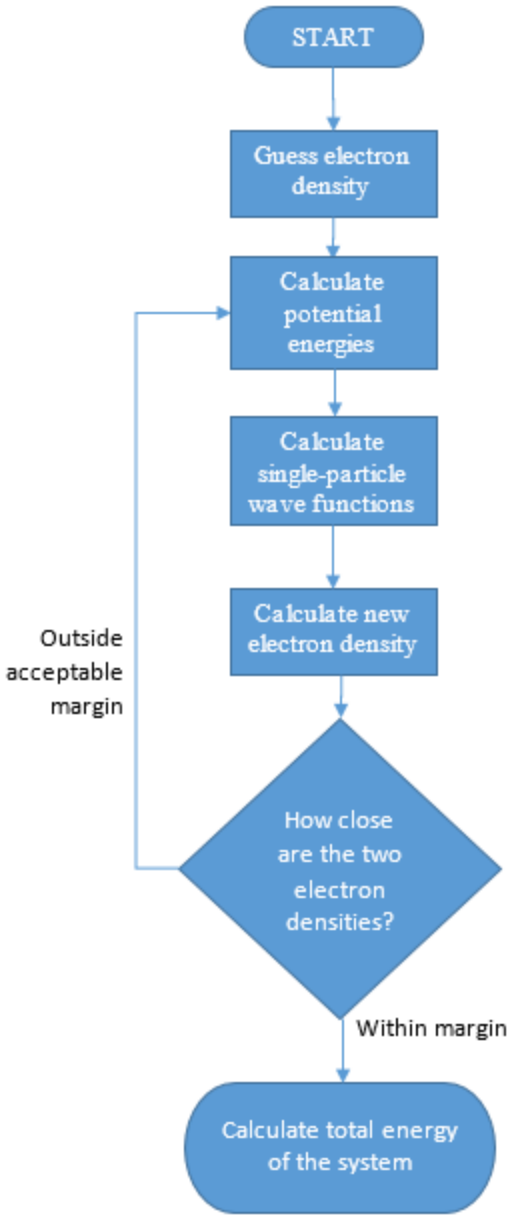

Figure 8: A demonstration of the self-consistent method density functional theory calculations use. The convergence criteria (or acceptable margin) is set at the beginning of the calculation.

1.5.3 Approximations Made by Density Functional Theory

Some approximations are made in all DFT calculations. These may include pseudopotentials, the exchange-correlation functional, the use of reciprocal space and k-points, and the basis set. Even with the application of the density functional theory, the number of electrons can still be prohibitively large for calculations when dealing with larger atomic numbers. The concept of pseudopotentials makes these calculations easier by separating electrons into two categories: valence and core. Valence electrons frequently move and interact with other atoms and electrons, and their potentials can vary. Core electrons, on the other hand, are usually fixed in

energy, and have nearly static wave functions. Pseudopotentials eliminate the need for calculating core electron potential by fixing them as static electric potentials. Adapting pseudopotentials improves computation time without much loss in accuracy (56, 57). The pseudopotentials and calculations in this study were based on the projector augmented-wave method (58).

The potential energy term *V(r)* in the Schrödinger equation becomes three potential energy terms in the Kohn-Sham equations, $V_{nuc\text{-}e}$ and V_H. This is shown in Equation 3.

$$[-(h^2/2\mu)\nabla^2 + V_{nuc-e}(r) + V_H(r) + V_{XC}(r)]\Psi_i(r) = E_i\Psi_i(r) \quad (3)$$

These terms account for the interactions of nuclei with electrons, and the Hartree potential, or the Coulomb interaction between electrons, which can be calculated from the electron density. The last term defines the exchange-correlation potential, a correction factor needed due to the assumptions made in density functional theory. This exact potential is unknown, so approximate exchange correlation functionals must be used. The simplest case assumes a uniform electron gas, i.e. a gas with constant density. This method, known as the local density approximation, or LDA, assumes that the electron density can be evaluated as constant when a small enough volume is selected. The LDA has been extended to include a local gradient of the electron density, known as the generalized gradient approximation, or GGA. Many GGA functionals are in use, but the Perdew-Burke-Ernzerhof (PBE) functional was used for this study (59, 60).

Since exact wave functions are unknown, continuous functions, a basis set, or a set of weighted functions, is defined in a DFT problem to approximate the wave functions or atomic orbitals. The basis set used in this study consisted of plane wave functions, of the form $e^{i*x} = \sin x + \cos x$. Plane wave basis sets are excellent for approximating a repeating unit, known as a supercell, such as a small group of atoms of a large, contiguous solid. This is due to their periodic nature. During the calculation, this basis set will mimic the actual wave functions by guessing weights for each function until a self-consistent solution is reached. Plane wave basis sets involve a summation of many reciprocal space vectors G, for an infinite series of integers m_1, m_2, and m_3. This is shown in Equations 4 and 5.

$$\phi_k(r) = \sum_G c_k + Gexp[i(k+G)r] \quad (4)$$

$$G = m_1b_1 + m_2b_2 + m_3b_3 \quad (5)$$

Summing over an infinite series for a basis set is impossible, and the basis set must be finite. The number of summations is limited by establishing a cutoff kinetic energy. Each vector G has a kinetic energy, and higher kinetic energy plane waves often have less relevance in calculations. Equation 6 describes the cutoff kinetic energy.

$$E_{cut} = \frac{\hbar}{2m}G_{cut}^2 \quad (6)$$

Therefore, our calculations will define a cutoff energy which limits the number of vectors G to a finite amount; after varying m_1, m_2, and m_3, all vectors G resulting in a kinetic energy lower than the cutoff will be included. The higher the cutoff energy, the more G-vectors will be included. A higher cutoff energy will result in greater accuracy achieved and time required, so a balance must be struck (60).

DFT calculations are often carried out in reciprocal space, rather than real space, as calculations with plane wave functions become much simpler to compute in those coordinates. Reciprocal space is defined in terms of k vectors, and a given supercell can be translated into this space, becoming known as the Brillouin zone. Many computations with periodic boundary conditions involve integration across the Brillouin zone. Monkhorst and Pack have defined a useful numerical integration method which exploits symmetries in the Brillouin zone to obtain an accurate integration using as few intervals as possible (61). This "special-point method" generates intervals within the symmetry-reduced Brillouin zone (also known as the irreducible Brillouin zone) based on a given number of integration points, known as k-points due to their location in reciprocal space. The more k-points in a calculation, the more accurate it will be; however, defining more k-points lead to greater memory and time requirements (60).

The use of plane wave basis sets meant that all VASP calculations were performed using periodic boundary conditions (PBC). Under PBC, the atoms defined in the simulation define what is called a "supercell." This supercell is then repeated in every direction in order to dictate an infinite system. In this way, calculations can be performed for large solid crystals such as TiO_2 by only defining a small number of atoms. PBC must also be considered when designing surfaces; a large empty space must be left in the supercell definition so that two adjacent cells do not interact with each other (62).

Calculating the band gap of the system was an integral part of our analysis. However, traditional DFT with PBE-PAW pseudopotentials severely underestimates band gap, and poorly predicts electronic state. Fortunately, a correction is available, called the Hubbard or U correction, which rectifies this issue and allows DFT to properly predict electronic configuration and density of states. When applying the U correction (or +U as often designated in the literature), an energetic correction is applied to individual electron types of specific atoms in the system. For instance, in this study, a correction of 4.5 eV applied to the d orbital of Ti atoms was sufficient for accurate density of states calculation (6).

2 Methodology

Our goal was to evaluate organometallic compounds and predict their effectiveness as photosensitizers when bonded to a TiO_2 semiconductor surface. Density functional theory (DFT) calculations were performed using the Vienna Ab-initio Simulation Package (VASP) to predict their photocatalytic activity both alone and bonded to titanium dioxide. Our objectives were as follows:

1. To accurately model the properties of TiO_2, such as the band gap and electron energies
2. To simulate a number of potential organometallic compounds and ensure our results agree with literature results
3. To determine which compounds could be optimal photosensitive materials

DFT calculations were performed to evaluate the density of states which occurred when titanium dioxide was bonded to our chosen organometallic compounds. This information determined how the band gap properties changed when a photosensitizer was present. Since visible light is readily available, photosensitizers which allowed TiO_2 to capture light in that part of the spectrum would be the most significant.

2.1 Modeling Introduction

The Vienna Ab initio Simulation Package, or VASP, was the primary modeling program used for these simulations (63). VASP is a density functional theory program that can be used to model quantum mechanics at the atomic level, such as the structure of molecules and their interactions with other compounds (63). This study used both VASP version 5.3 and 5.4.4.

To model titanium dioxide, both bulk and surfaces, the Atomic Simulation Environment (ASE) (64) for Python was utilized. ASE consists of a wide variety of tools and libraries capable of generating atomic structures in formats readable by VASP, as well as many other simulation programs. Within ASE, crystals could be generated automatically, and replicated to form a surface. Using a program called VESTA, atomic structures could be visualized in three dimensions and tweaked (65); other three-dimensional modeling programs such as Avogadro were also used to generate correct geometry for organometallic molecules and model them in three dimensions. (66).

2.2 VASP Input

The VASP simulation package requires a number of input files to begin the calculation. The INCAR file indicates what tasks the simulation package will perform and what methods it will use (see Figure 9). Many variables can be defined in the INCAR file, but most have defaults which cover normal use cases, allowing INCAR files to be fairly short.

```
INCAR created by Atomic Simulation Environment
 ENCUT = 450.000000 ——Plane-wave basis set cutoff energy (eV)
 SIGMA = 0.100000 ——Width of smearing (eV), see ISMEAR below.
 EDIFF = 1.00e-05 —— Target iteration accuracy. Ionic step completes if two electronic steps are this close (eV)
 EDIFFG = -2.00e-02 —— Threshold energy. Relaxation simulation will complete if forces fall below threshold (eV)
 PREC = Normal —— General accuracy parameter. Defines defaults for several other parameters.
 ALGO = 38 —— Iteration scheme. This setting indicates the Davidson-block iteration scheme.
 ISPIN = 2 ——Spin-polarized calculations are performed.
 ISMEAR = 0 ——Orbital partial occupancies, in this case defined by Gaussian smearing
 ISTART = 0 —— Calculation begins from scratch, no input from previous calculations.
 NSW = 500 ——Maximum number of ionic steps allowed. 500 is very high
 IBRION = 2 —Method for relaxing ions into a lower-energy state. This option is the conjugate-gradient method
 NPAR = 2 ——Number of computing nodes used for parallelization, helps save memory and improves calc time
 ISIF = 2 —— Controls parameters allowed to relax during calculation. This setting relaxes ions only.
 LCHARG = .TRUE. | Charge densities from previous calculations are used.
 LWAVE = .TRUE. | Orbitals from previous calculations are used.
```

Figure 9: A sample INCAR file. Descriptions are provided for the parameters used, but many more exist which have been set to their defaults. The VASP manual describes in detail the various parameters in the file.

The KPOINTS file provides either the location of each k-point used in the simulation, or the means to automatically generate k-points needed in the simulation (see Figure 10). The Monkhorst-Pack grid method is a very common way to generate k-points, as described in section 1.5.3.

```
Automatic k-points
0 —— K-points are generated automatically.
monkhorst —— Monkhorst-Pack grid method is used.
8 8 8 —— Number of K-points per unit length in reciprocal space
0 0 0 —— K-point mesh shift (in this case nothing)
```

Figure 10: Example of a simple KPOINTS file.

The POSCAR file defines the lattice dimensions, the atoms being simulated, and the position of each atom (see Figure 11). This file includes all the coordinates for atom nuclei in three-dimensional space, within a three-dimensional lattice whose endpoints are also defined within the POSCAR. When using plane-wave basis sets, this lattice doubles as the unit supercell, i.e. the repeating group of atoms being examined.

```
Ti O ———————— Acceptably unoriginal system name.
1.0 —— Universal scaling factor. "1.0" means everything is to scale.
    3.81  0.0000000000     0.0000000000
    0.0000000000     3.81  0.0000000000
    0.0000000000     0.0000000000     9.71
```
Lattice boundary coordinates. Each coordinate defines the corner of a rectangular prism.

```
  Ti    O
   4    8 ———————— There are four titanium atoms and eight oxygen atoms in this crystal.
Direct ——"Direct" means the following position coordinates are fractions of the total lattice size.
     0.000000000          0.000000000          0.000000000
     0.500000000          0.500000000          0.499999950
    -0.000000000          0.500000000          0.249999975
     0.500000000         -0.000000000          0.750000025
     0.000000000          0.000000000          0.207999998
     0.500000000          0.500000000          0.708000011
    -0.000000000          0.500000000          0.457999986
     0.500000000         -0.000000000          0.958000086
     0.500000000         -0.000000000          0.542000014
    -0.000000000          0.500000000          0.041999999
     0.500000000          0.500000000          0.291999989
     0.000000000          0.000000000          0.791999989
```
Position coordinates for each atom in the order they are defined - i.e. the first four lines are titanium atoms, the next eight lines are oxygen atoms.

Figure 11: Example of a POSCAR file, defining a titanium dioxide crystal.

The POTCAR file houses the pseudopotential definitions of each type of atom involved in the simulation. POTCAR files are included in the VASP package for each element (see Figure 12). When running a simulation involving multiple elements, POTCAR files must be appended together in the order they are defined in the POSCAR file. For instance, in Figure 11 above, titanium and oxygen are called for in the simulation. A POTCAR file for this simulation would be generated by attaching titanium and oxygen POTCAR files together, in that order.

```
 PAW_PBE Ti_pv 07Sep2000
 10.00000000000000000
 parameters from PSCTR are:
   VRHFIN =Ti: d3 s1
   LEXCH  = PE
   EATOM  =  1042.3781 eV,   76.6126 Ry

   TITEL  = PAW_PBE Ti_pv 07Sep2000
   LULTRA =        F    use ultrasoft PP ?
   IUNSCR =        1    unscreen: 0-lin 1-nonlin 2-no
   RPACOR =    2.200    partial core radius
   POMASS =   47.880; ZVAL   =   10.000    mass and valenz
   RCORE  =    2.500    outmost cutoff radius
   RWIGS  =    2.500; RWIGS  =    1.323    wigner-seitz radius
(au A)
   ENMAX  =  222.338; ENMIN  =  166.753 eV
   RCLOC  =    1.701    cutoff for local pot
   LCOR   =        T    correct aug charges
   LPAW   =        T    paw PP
   EAUG   =  482.848
   DEXC   =    -.008
   RMAX   =    3.092    core radius for proj-oper
   RAUG   =    1.300    factor for augmentation sphere
   RDEP   =    2.538    radius for radial grids
```

Figure 12: An example of the beginning of a POTCAR file. This particular file gives electronic information for a titanium atom (Ti_pv).

2.3 VASP Output

VASP also generates a number of files as output to each calculation. Many of these files define information that can be used to continue or rerun the calculation. For instance, charge densities are contained in the CHG and CHGCAR files. Wave function information is written to the WAVECAR file. Final positions of atoms after relaxation are written to the CONTCAR file, which has the same format as the POSCAR file. The major output, however, is stored in the OUTCAR file, which stores relaxation information from all ionic and electronic steps, computation time and memory used, as well as energies of the calculation, and other information (see Figure 13). The OUTCAR file will include the line "reached required accuracy - stopping structural energy minimization" when the calculation has come to an end.

```
 FREE ENERGIE OF THE ION-ELECTRON SYSTEM (eV)
 ---------------------------------------------------
 free  energy   TOTEN  =      -107.64160493 eV

 energy  without entropy=     -107.64160493  energy(sigma->0) =     -107.64160493

d Force = 0.1186243E-02[ 0.132E-03, 0.224E-02]  d Energy = 0.1207217E-02-0.210E-04
d Force =-0.3124193E+01[-0.314E+01,-0.311E+01]  d Ewald  =-0.3124160E+01-0.331E-04
```

Figure 13: A small sample of the OUTCAR file, which is usually quite large. The final energy of this system after the DFT calculation is complete is -107.64 eV.

2.4 Generating Simulation Structures

Our calculations involved a surface of anatase with the (1 0 1) orientation. This is known to be one of the lower energy surfaces of anatase, and therefore one of the most stable (7). The structure of the repeating supercell is determined by the position of all atoms within it. We can define a supercell with side lengths *a* and height *c*. All atoms in the repeating structure can be defined by a vector $\mathbf{r} = (u_i n_1 a, v_i n_2 a, w_i n_3 c)$, where u_i, v_i, and w_i are atom i's fractional coordinates within the supercell, and n_1, n_2, and n_3 are any integers. The idea of fractional coordinates defines atom position as a fraction of the lattice in that dimension; for instance, a fractional coordinate of u = 0.5 in a supercell of a = 10 Å would yield a position of 5 Å. The parameters *a* and *c* are known as lattice constants and are usually different to avoid lattice solutions changed by symmetry (see Figure 14). The best value of these constants are the ones that minimize the energy of the supercell. The values of *a* and *c* can be determined using a DFT program such as VASP by iteration, performing a number of calculations at different values of *a* and different ratios *c/a* until a local minimum is found (see Figure 15). This is called lattice optimization.

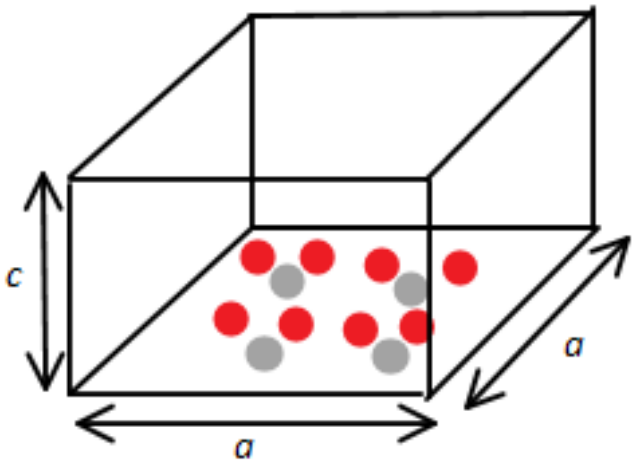

Figure 14: A visualization of a supercell with side lengths a and height c. Each atom i in the crystal has its own unique fractional coordinates u_i, v_i, and w_i.

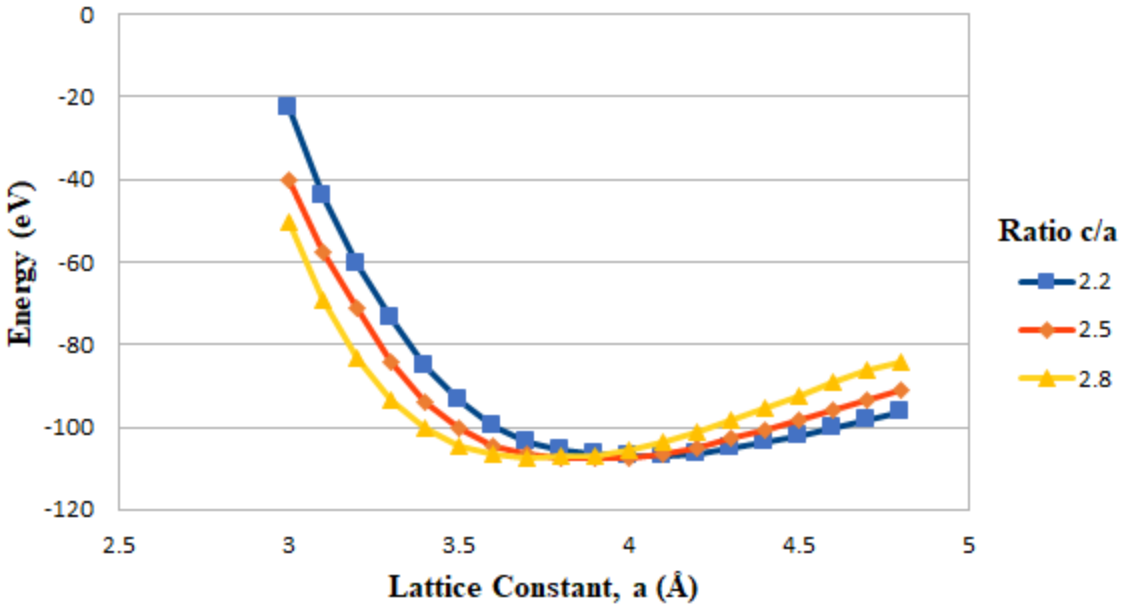

Figure 15: A demonstration of lattice optimization. By varying both the lattice constant a (x-axis) and the ratio between constants c and a (curves), the energy of the system varies (y-axis). At the right lattice constants, the crystal is at a minimum energy. The lattice constants that minimize the energy are the optimal constants at the level of theory we used to simulate the crystal, which in our case was DFT using the PBE exchange correlation functional.

In order to determine the lattice parameters for modelling a titanium dioxide surface, a TiO_2 supercell containing four titanium atoms and eight oxygen atoms was generated using the ASE package in python and changed to fractional coordinates using VESTA. This supercell formed an infinite TiO_2 crystal, also known as bulk TiO_2. The lattice was then optimized by conducting calculations varying the lattice constant *a* as well as the ratio *c/a*, first in increments of 0.1, then in increments of 0.01 to find the lattice constants to two significant digits. After the lattice constants were discovered, we allowed VASP to further minimize the energy by allowing first the supercell volume to change, then the supercell shape. These calculations returned lattice constants optimized to several decimal places.

These optimal lattice constants were then used to generate a titanium dioxide surface in the ASE. The bulk titanium dioxide crystal was generated using optimum lattice parameters, replicated to form an anatase surface, and built four layers deep to simulate depth of the nanoparticle (see Figure 16). The bottom two layers of the crystal were then fixed during calculations, to simulate the fixed nature of the nanoparticle. This surface was then relaxed so all atoms would settle into the positions of lowest energy. The band gap was then calculated for the surface by performing a Density of States (DOS) calculation. This surface was used as a representation of a titanium dioxide nanoparticle surface.

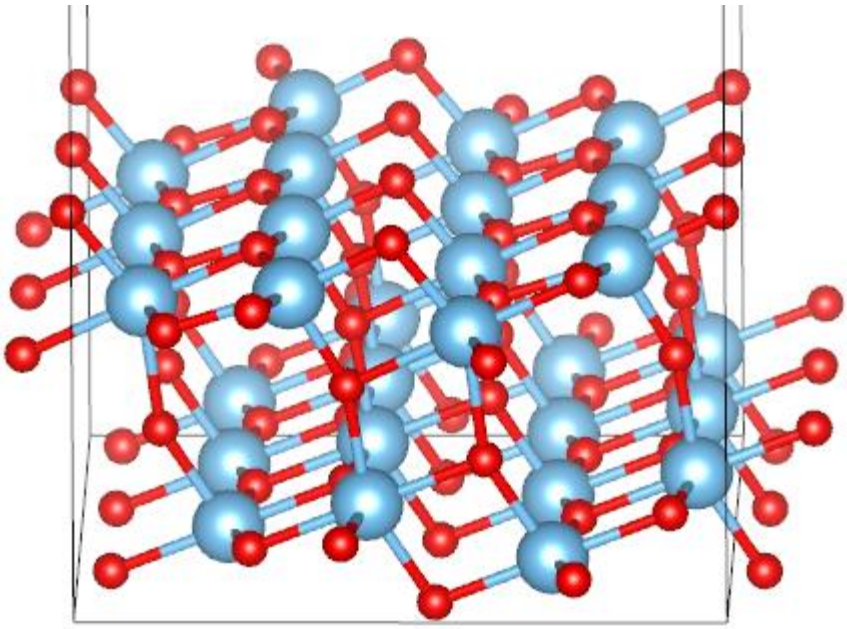

Figure 16: The generated surface of a TiO2 nanoparticle, or anatase (101) surface, used in this work. Blue atoms are titanium, red atoms are oxygen. The lattice is much bigger in the z-direction in order to simulate a "slab" of TiO2 rather than a solid block.

Using Avogadro, various organometallic complexes were created, starting with ferrocyanide. Ferrocyanide was selected due to previous research indicating its strong potential as a photosensitizer (67). Ferrocyanide was used as a base complex, and many analogues were investigated by exchanging the iron atom for another metal or exchanging one or more cyanide ions for other groups such as carbonyl, a halogen, or cyanide. Complexes of other geometries, such as tetrahedral, square planar, or trigonal bipyramidal, were also studied. The full list of organometallic complexes examined can be found in Appendix B.

Each organometallic complex was first modeled using VASP to relax the ions into ground state and evaluated using a density of states calculation to determine the band gap. Next, the organometallic complex was attached to the titanium dioxide surface by adding it to the existing POSCAR file. A preliminary structure was created using Avogadro for attaching one or more ligands from the complex to the titanium dioxide surface. Relaxation was then performed on the system to ensure they were in ground state. Once relaxed, a density of states calculation was performed on the whole system in order to evaluate its band gap (see Figure 17).

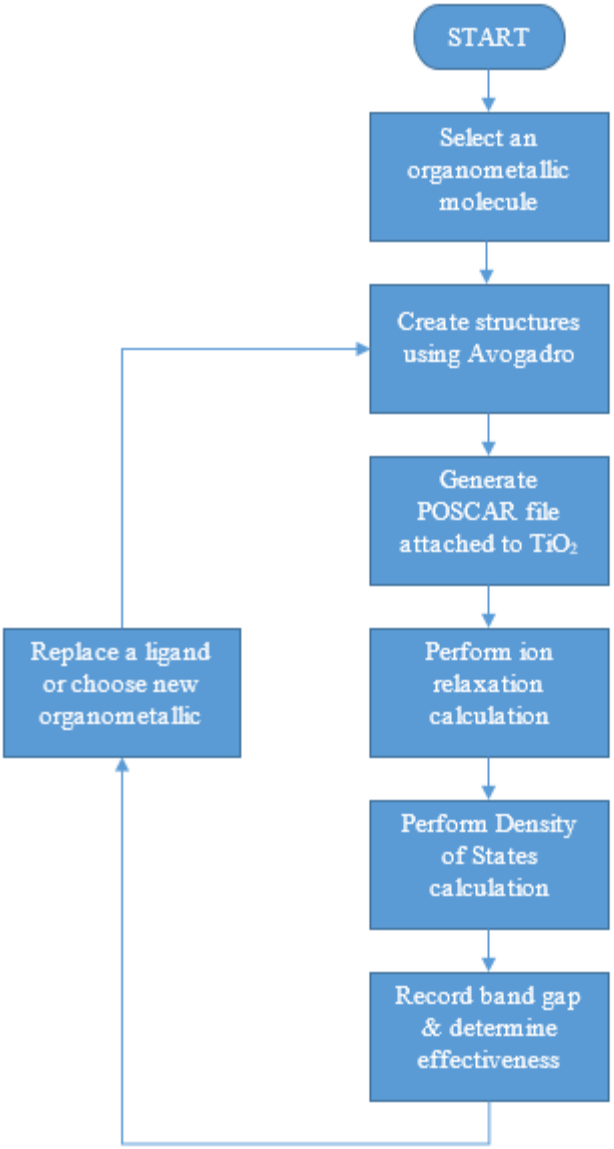

Figure 17: Flowchart demonstrating the workflow involved in investigating organometallic molecules as photosensitizers.

After performing ion relaxation on the adsorbed organometallic complex, two factors were observed to discover the presence of a bond. The shortest distance between an atom in the complex and on the surface was measured and recorded as the bond length. Bond lengths of under 2.6 Å were considered to be plausible bonds. The second factor was the binding energy between the complex and the surface, which is shown in Equation 7.

$$E_{binding} = (E_{anatase} + E_{organometallic}) - E_{organometallic\ on\ slab} \quad (7)$$

The total energies from the gas phase organometallic complex and anatase slab were summed and compared with the total energy from the complex adsorbed on the slab; a reduction of energy in the adsorbed complex indicates a bond-like interaction. An adequate bond between

the complex and slab was considered to be on the order of 1 eV. A weak bond would be on the order of 0.5 eV, while binding energies less than 0.5 eV were considered to be weak interactions.

2.5 Calculation Settings

The simulations performed for this study can be classified into three major categories by system type: bulk TiO_2, individual organometallic molecules, and organometallics adsorbed on anatase surfaces. For all the calculations, the Perdew-Burke-Ernzerhof (PBE) exchange-correlation functional (60) was used, in tandem with projector augmented-wave (PAW) pseudopotentials (58). Gaussian smearing was used nearly universally for wavefunction partial occupancy; in certain cases, tetrahedron method was substituted. To ensure similar results, a constant cutoff energy of 450 eV was used for all calculations, while convergence criteria for the wavefunction was set to an energy difference of $1*10^{-5}$ eV. Figure 18 highlights the differences between the three types of INCAR files used for geometry relaxation.

```
ENCUT = 450.000000
SIGMA = 0.100000
EDIFF = 1.00e-05
EDIFFG = -2.00e-02
PREC = Normal
ALGO = Fast
ISPIN = 2
ISMEAR = 0
ISTART = 0
NSW = 500
IBRION = 2
NPAR = 2
LDAUTYPE = 2
ISIF = 2
LCHARG = .TRUE.
LWAVE = .TRUE.
LREAL = Auto
LDAU = .TRUE.
LDAUL = -1 2
LDAUU = 0.000 4.500
LDAUJ = 0.000 0.000
```

```
ENCUT = 450.000000
SIGMA = 0.100000
EDIFF = 1.00e-05
EDIFFG = -2.00e-02
PREC = Normal
ALGO = Fast
ISPIN = 2
ISMEAR = 0
ISTART = 0
NSW = 500
IBRION = 2
NPAR = 2
ISIF = 2
LCHARG = .TRUE.
LWAVE = .TRUE.
LREAL = Auto
```

```
ENCUT = 450.000000
SIGMA = 0.100000
EDIFF = 1.00e-05
EDIFFG = -2.00e-02
PREC = Normal
ALGO = Fast
ISPIN = 2
ISMEAR = 0
ISTART = 0
NSW = 500
IBRION = 2
NPAR = 2
ISIF = 2
LCHARG = .TRUE.
LWAVE = .TRUE.
LREAL = Auto
LDAU = .TRUE.
LDAUTYPE = 2
LDAUL = -1 2 -1 -1 -1
LDAUU = 0.000 4.500 0.000 0.000 0.000
LDAUJ = 0.000 0.000 0.000 0.000 0.000
```

Figure 18: INCAR files used for ion relaxation. These were used for bulk TiO2 (left), organometallic complexes (center), and adsorbed complexes (right).

The major differences between these INCAR files are the LDAU parameters, which dictate the +U correction. The order and presence of these parameters matched the order of elements in the POTCAR file. In the case of our calculations, our +U correction was 4.5 eV (LDAUU = 4.500) on the d-orbitals of titanium (LDAUL = 2). No other atoms received +U corrections. Another varying part of the ion relaxation was the k-point mesh; in most cases, a simple mesh of 1x1x1 k-points was used. In the case of bulk TiO_2, however, 8x8x8 k-points were used since the unit cell was quite small.

Density of states calculations were the other major part of our work. These calculations were similar to geometry relaxation as much as possible: PBE exchange-correlation functionals, PAW pseudopotentials, Gaussian smearing, 450 eV cutoff energy, and $1*10^{-5}$ convergence energy criteria. Figure 19 compares the different density of states INCAR files.

```
ENCUT = 450.000000
SIGMA = 0.100000
EDIFF = 1.00e-05
EDIFFG = -2.00e-02
PREC = Normal
ALGO = Fast
ISPIN = 2
ISMEAR = 0
NELM = 200
NSW = 0
NCORE = 2
LREAL = Auto
LMAXMIX = 4
LORBIT = 10
EMIN = -20
EMAX = 10
NEDOS = 1200
LDAUTYPE = 2
LDAU = .TRUE.
LDAUL = -1 2
LDAUU = 0.000 4.500
LDAUJ = 0.000 0.000
```

```
ENCUT = 450.000000
SIGMA = 0.100000
EDIFF = 1.00e-05
EDIFFG = -2.00e-02
PREC = Normal
ALGO = Fast
ISPIN = 2
ISMEAR = 0
NELM = 200
NSW = 0
NCORE = 2
LREAL = Auto
LMAXMIX = 4
LORBIT = 10
EMIN = -12
EMAX = 0
NEDOS = 1200
```

```
ENCUT = 450.000000
SIGMA = 0.100000
EDIFF = 1.00e-05
EDIFFG = -2.00e-02
PREC = Normal
ALGO = Fast
ISPIN = 2
ISMEAR = 0
NELM = 200
NSW = 0
NCORE = 2
LREAL = Auto
LMAXMIX = 4
LORBIT = 10
EMIN = -12
EMAX = 0
NEDOS = 1200
LDAU = .TRUE.
LDAUTYPE = 2
LDAUL = -1 2 -1 -1 -1
LDAUU = 0.000 4.500 0.000 0.000 0.000
LDAUJ = 0.000 0.000 0.000 0.000 0.000
```

Figure 19: INCAR files used for density of states calculation. These were used for bulk TiO2 (left), organometallic molecules (center), and adsorbed complexes (right).

The inclusion of the parameter NSW = 0 prevented geometry relaxation, while LMAXMIX = 4 ensures all the appropriate charge information is written. The parameter dictating a density of states calculation is LORBIT, which is set to 10 to write a DOSCAR and PROCAR file. The DOSCAR file includes the density of states for the calculation. Choice of k-point mesh was similar to that during geometry relaxation, although density of states calculations may require more k-points to be accurate. For bulk TiO_2, a 12x12x12 k-point mesh was used, while an 8x8x8 mesh was used for most organometallic molecules due to limitations on the tetrahedron k-point method used. Density of states calculations for both the lone anatase slab and the slab plus adsorbate were performed with a 1x1x1 k-point mesh.

3 Results and Discussion

3.1 Modeling Bulk Titanium Dioxide

3.1.1 Determining TiO_2 Lattice Parameters

The first step in modeling a titanium dioxide surface was to determine the supercell lattice constants *a* and *c*. Lattice optimization was performed to find the optimal parameters of TiO_2 that resulted in the lowest energy. This was done by modelling a bulk TiO_2 crystal in fractional coordinates and controlling both *a* and the ratio *c/a* to minimize the overall energy. First, a coarse optimization was performed with *a* values from 3 to 4.8 Å and ratios of 2.2 to 2.8, both in intervals of 0.1. The lattice parameters that resulted in the lowest energy was the local optimum (see Figure 20).

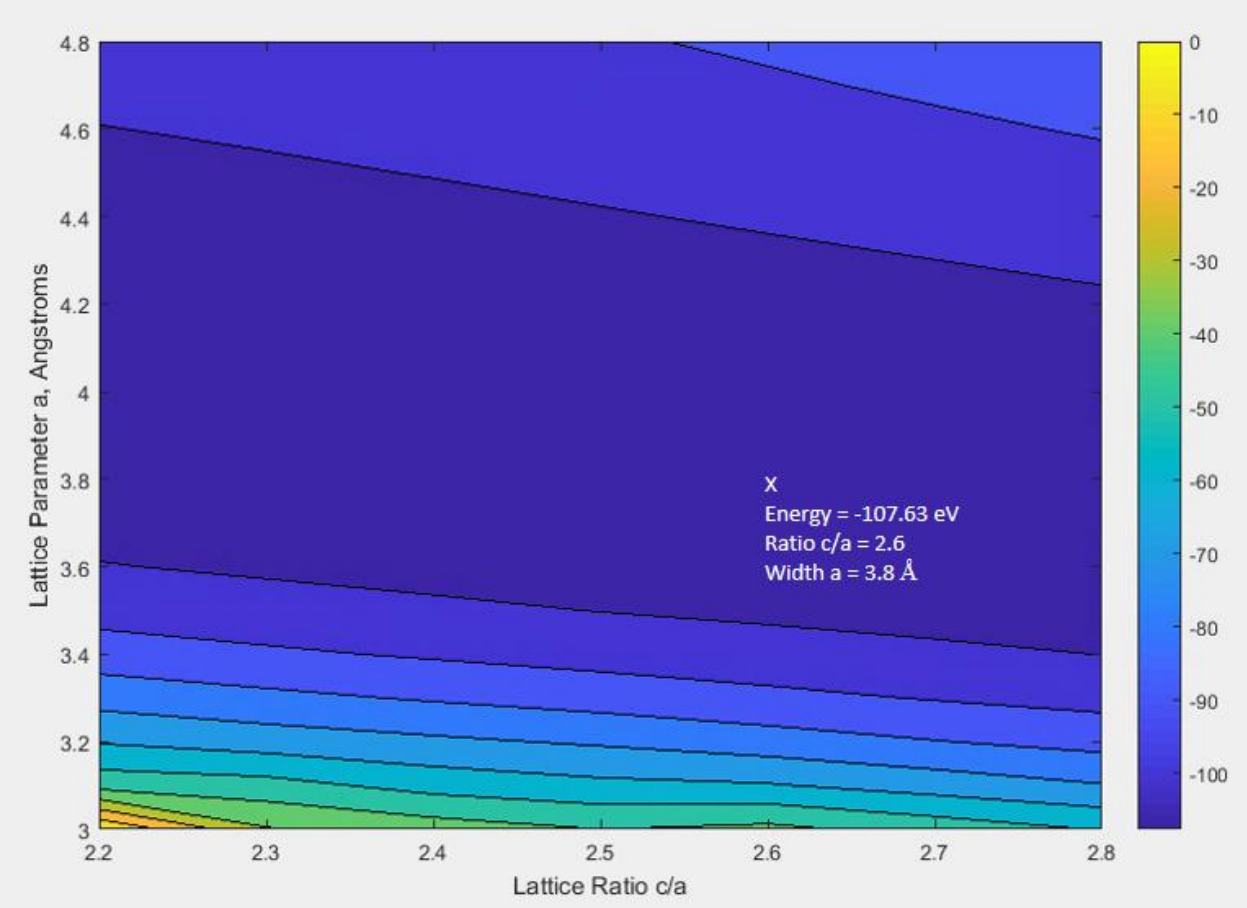

Figure 20: The results of the coarse lattice optimization, with minimum marked.

The contour figure demonstrates that the global minimum was not accurately determined. In order to tune the lattice parameters further, a fine lattice optimization was performed with *a* values from 3.73 to 3.88 Å and ratios of 2.4 to 2.7, in intervals of 0.01. Again, the optimization sought a point of lowest energy (see Figure 21).

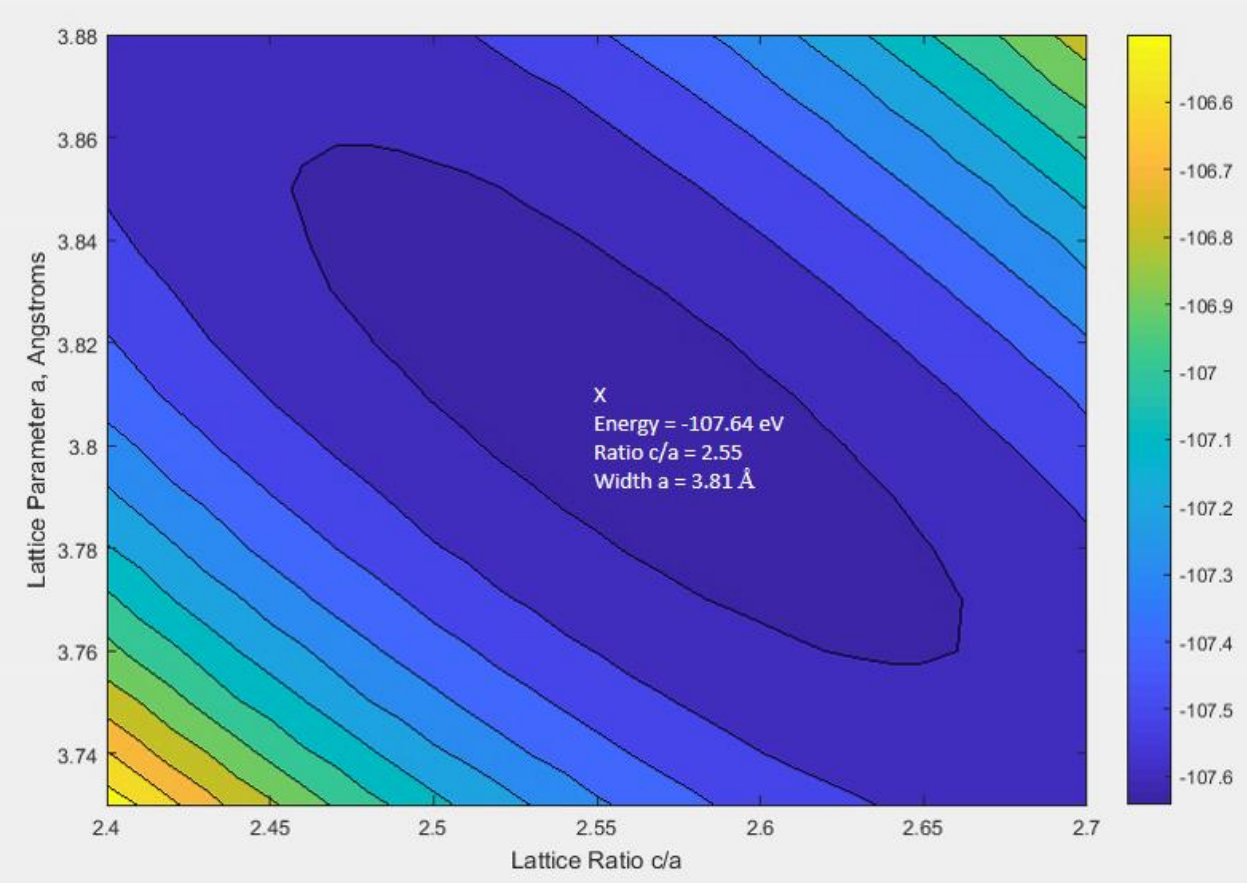

Figure 21: The results of the fine lattice optimization, with the minimum marked.

Our lattice optimization discovered a minimum energy with lattice parameters a = 3.81 Å and c = 9.51 Å. These parameters are in excellent agreement with previous DFT results (a = 3.78 Å and c = 9.56 Å (68); a = 3.76 Å and c = 9.52 Å (69)) as well as experimental (a = 3.78 Å and c = 9.51 Å (5)) work, indicating that our titanium dioxide crystal is similar enough to real values to produce meaningful results.

In the above calculations, the supercell lattice parameters are held constant while ions are allowed to move and relax. However, two additional relaxation methods are possible in VASP: relaxing the cell shape and relaxing the cell volume; these three methods can be used in any combination. Both of these methods can change the lattice parameters. To ensure that we reached a local minimum, two additional simulations were performed at these relaxed lattice parameters. First, by setting the ISIF input parameter to 4, VASP was allowed to change the cell shape in addition to allowing ions to move while keeping volume fixed. Second, by setting the ISIF input parameter to 3, VASP changed the ion positions, cell shape, and cell volume (ISIF = 3) during simulation. The results after these relaxations were compared to the initially discovered lattice parameters as described above (see Figure 21). We found after allowing the volume to change using VASP's algorithms the differences were minimally different (<1%). Therefore, we can further be certain that our optimized lattice parameters are correct. The lattice parameters a = 3.81 Å and c = 9.51 Å were therefore used to generate a titanium dioxide surface.

3.1.2 Density of States Analysis on Bulk Titanium Dioxide

Density of states indicate the distribution of electronic states, both occupied and unoccupied. From a density of states graph, the band gap can be determined, among other properties. We prepared a density of states graph of bulk titanium dioxide in order to verify our calculations. We present our plot of density of states calculated without the +U correction to compare it with a literature plot (see Figure 22).

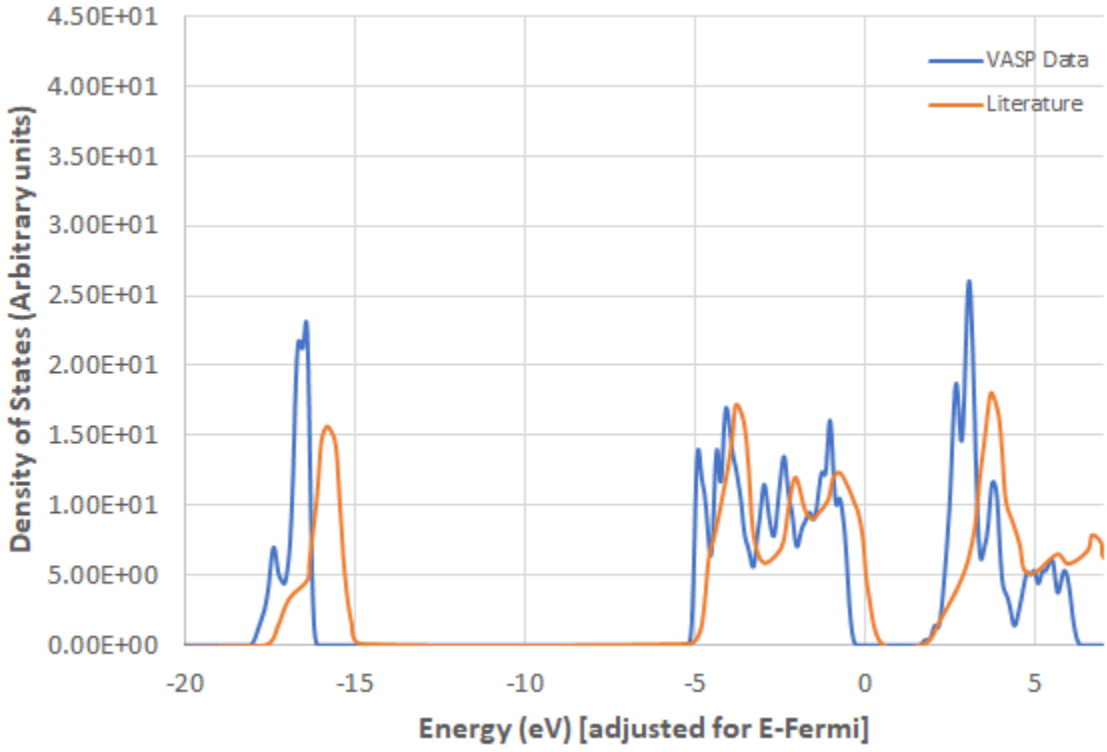

Figure 22: Our calculated density of states plot from VASP compared with literature data generated from similar levels of theory (70).

Our calculated density of states overall is an excellent match to the literature, with a major peak at -16 eV, a series of peaks from -5 to 0 eV, and another major peak under 5 eV. Density of states without the +U correction predicts a band gap of 2.15 eV, too low but also agreeing with literature calculations at similar levels of theory, around 2-2.5 eV (6). Notably, our data and the literature seem to be offset by ~0.5 eV. This difference may result from choice of pseudopotentials: their calculations were done with ultra-soft pseudopotentials while our calculations used projector augmented-wave pseudopotentials.

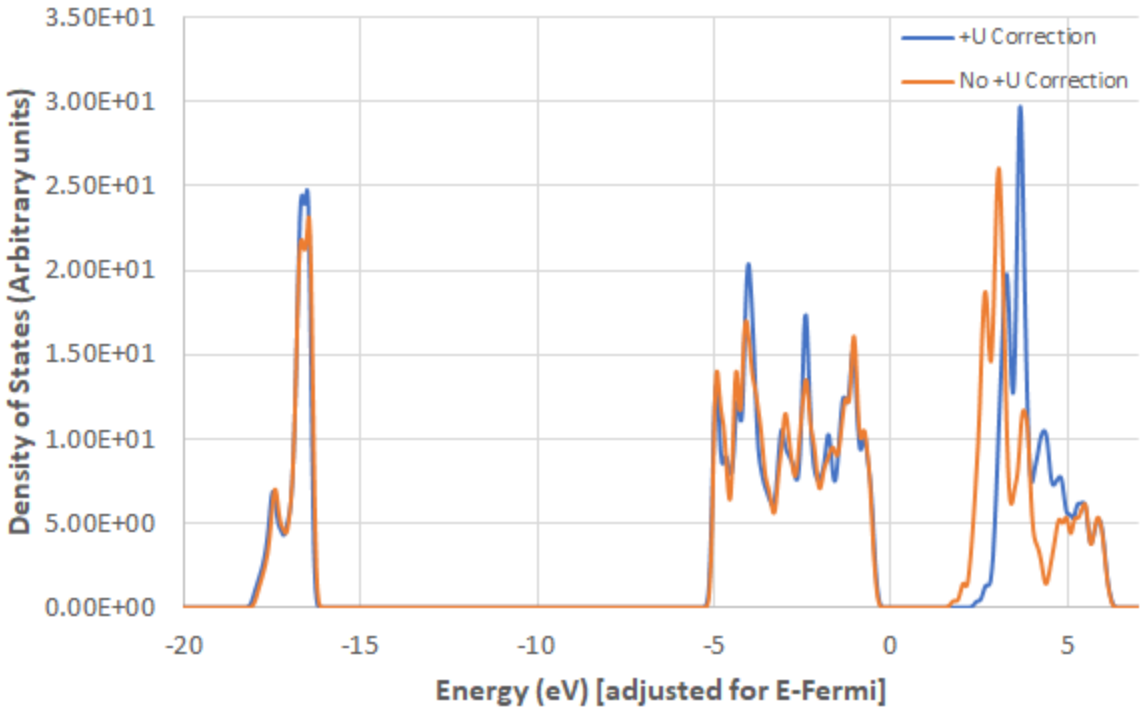

Figure 23: Our calculated density of states plot for bulk titanium dioxide with the U correction, in blue. We have included the plot without the +U correction in orange.

As Figure 23 shows, results using the +U correction predict a band gap of just over 2.80 eV, which agrees well, although not perfectly, with literature values of 3-3.2 eV (6). Comparing to the graph without the +U correction, it is clear that only the position of the valence band is changed, increasing the band gap. This argues for the use of the +U correction for density of states calculations. We used the +U correction for all density of states results involving TiO2.

3.2 Modeling the Titanium Dioxide Surface

3.2.1 Surface Slab Creation and Justification

Before attaching organometallic molecules, the Atomic Simulation Environment was used to generate a model four-layer titanium dioxide surface slab consisting of 24 titanium atoms and 48 oxygen atoms from the determined lattice parameters (a = 3.81, c = 9.51). VASP was used to electronically relax this surface to ensure the most stable structure was achieved. Two slabs were prepared in this exercise; one with the bottom layer of titanium dioxide fixed (i.e. prevented from relaxing), and one without this restriction. The slab with the bottom layer fixed would be the basis for all our surface adsorption calculations and was used for the rest of this study; however, fixing the bottom layer artificially inflated the energy of the system, so the unrestricted slab was prepared to properly calculate the surface energy.

Fixing the bottom layer simulates the condition where the lower slab levels are in bulk-like configuration, such as in a nanoparticle. The top layers interact with the bottom, frozen bulk-like

layers of the slab and "behave" more realistically on the surface. The slab with frozen layers would be used in calculations involving adsorption of species to the surface. The surface energy was also needed as a benchmark, however, and this was inaccurately predicted by the slab with frozen layers. In order to obtain the surface energy associated with the titanium dioxide surface, the entire slab was allowed to relax. Appendix A details the calculation of surface energy from bulk and slab energies.

Our titanium dioxide surface energy was calculated as 0.38 J/m^2 for our (1 0 1) surface. Another paper calculated the surface energy as 0.49 J/m^2 for the same surface, although that paper used ultra-soft pseudopotentials rather than projector augmented-wave pseudopotentials (7). Since these values are reasonably close, they indicate that our slab model is adequate.

3.2.1 Surface Density of States Analysis

We also calculated the density of states for the titanium dioxide surface slab, to serve as a base case for adsorbed cases. We examined surface density of states both with and without the +U correction, in order to compare with our bulk titanium dioxide and understand the repercussions of having a slab only a few atoms thick. Figure 24 shows these density of states results. Aside from the difference in peak height, which arises from the differing number of atoms in the supercell, the two graphs are very similar; electronic states near -16 eV, a cluster of electronic states from -5 eV to 0 eV, and valence band states between 0 and 5 eV. The reduced band gap is a result of the small slab thickness. Increasing the slab thickness should make our system more bulk-like and give a band gap closer to the bulk band gap. Note that with the +U correction, band gap is increased, but it is still smaller than that in bulk TiO_2. Since the electronic structure of this surface slab model is sufficiently close to literature values, we proceeded to model organometallics and adsorb them to the surface.

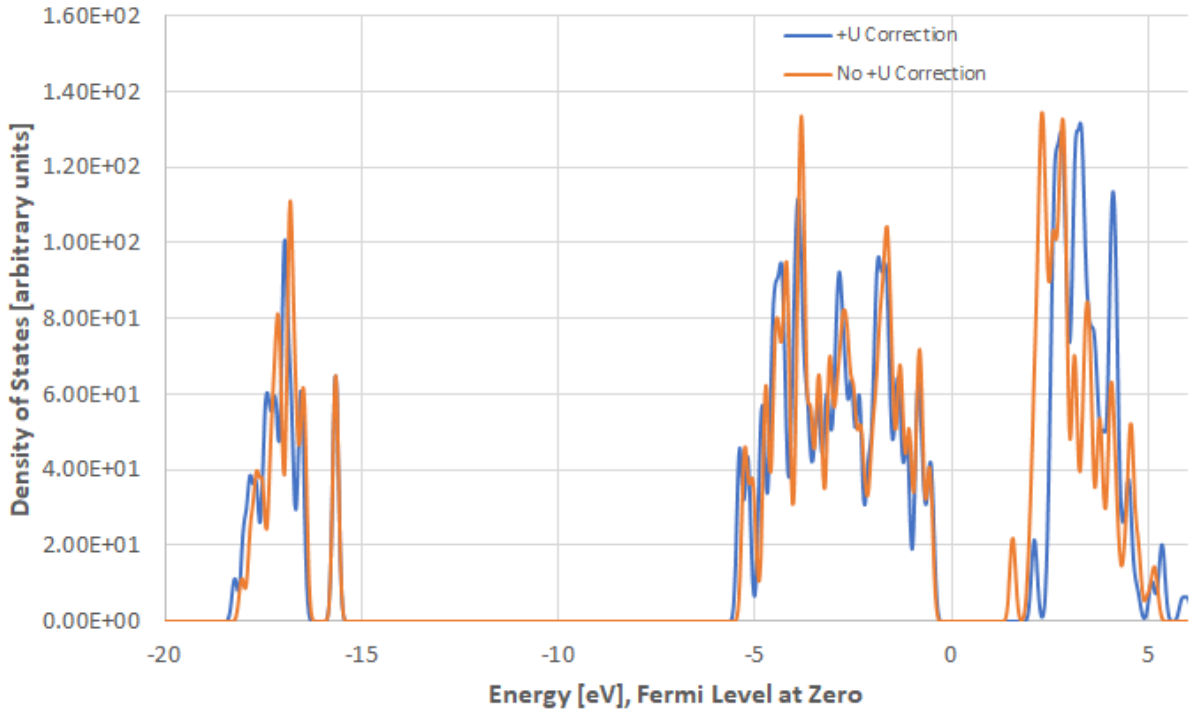

Figure 24: Calculated density of states for the surface slab of titanium dioxide using DFT+U, compared with the simple DFT density of states plot. The DFT plot has a band gap of 2.06 eV, while the DFT+U plot has a band gap of 2.58 eV.

3.3 Modeled Organometallic Compounds in Gas Phase

3.3.1 Gas Phase Molecules

Molecules were first built in Avogadro, optimized using the "optimize geometry" option wherever possible, and the molecular coordinates was extracted and used for VASP calculations. These molecules were ran using large cells of at least 15 Å for each lattice parameter, to prevent individual molecules from interacting with each other due to the periodic boundary conditions. In this way, each molecule was essentially in the gas phase. First, we performed VASP calculations to relax the atom positions of the molecules, giving what could be considered the "best" configuration of the molecule. Second, we performed density of states calculations on each converged molecule, calculating the HOMO and LUMO energies of the molecules. The calculated structures and HOMO-LUMO gaps were compared with literature values wherever possible to assess their validity.

We show in Tables 1, 2, and 3 our calculated bond lengths of various organometallic compounds compared to previous literature values. The maximum absolute difference in bond lengths between calculated values and literature was 0.21 Å, but the minimum absolute difference was 0.002 Å. The average absolute difference was 0.051 Å. This indicated an overall good agreement between our bond lengths and those in literature. The only case to stand out with a

significant disagreement is $Mn(CN)_6^{4-}$; compared with literature values, our VASP calculations underestimated its metal-ligand bond lengths. Since $Mn(CN)_6^{4-}$ is the only molecule studied including Mn-C bonds, we cannot comment on how accurate VASP modeled such bonds. This molecule may be an outlier in our calculations. We conclude our data to be overall trustworthy, with the exception of $Mn(CN)_6^{4-}$, and our calculated values reasonable. Optimized configurations of all molecules can be found in Appendix B.

Table 1: Calculated Bond Lengths of Octahedral Molecules Compared to Literature Values

Molecule, Fig # in Appendix B	VASP Calculated Bond Length, Å			*Literature Bond Length, Å			*Reference Number
	M-L, Equatorial	M-L, Axial	C-N or C-O	M-L, Equatorial	M-L, Axial	C-N or C-O	
$Fe(CN)_6^{4-}$, B1	1.94	1.94	1.18	1.9	1.9	1.18	DFT (71)
$Co(CN)_6^{4-}$, B2	1.91	1.91	1.18	1.903	1.886	1.15	EXP (72)
$Mn(CN)_6^{4-}$, B3	2	2	1.18	2.21	2.21	1.16	EXP (73)
$Os(CN)_6^{3-}$, B4	2.06	2.06	1.18	2.058	2.058	1.146	EXP (74)
$Ti(CN)_6^{4-}$, B5	2.16	2.16	1.18	2.26	2.26	1.17	EXP (75)
$Cr(CO)_6$, B6	1.9	1.9	1.16	1.91	1.91	1.14	DFT (76)
$Ru(CN)_6^{3-}$, B7	2.07	2.07	1.18	Values could not be found			

**Literature references are indicated; DFT means the reference is based on density functional theory calculations, while EXP means the reference is from experimental results*

Table 2: Calculated Bond Lengths of Trigonal Bipyramidal Molecules Compared to Literature Values

Molecule, Fig # in Appendix B	VASP Calculated Bond Length, Å				*Literature Bond Length, Å				*Reference Number
	M-L, Equatorial	M-L, Axial	C-O	Halide	M-L, Equatorial	M-L, Axial	C-O	Halide	
$Fe(CO)_5$, B8	1.8	1.8	1.16	N/A	1.81	1.81	1.16	N/A	DFT (77)
$Fe(CO)_3Cl_2$, B9	1.91	1.83	1.15	2.22	1.89	1.89	1.16	2.28	EXP (78)
$Fe(CO)_3Br_2$, B10	1.73	1.83	1.15	2.35	1.89	1.89	1.15	2.4	EXP (78)
$Fe(CO)_3I_2$, B11	1.72	1.82	1.15	2.52	1.89	1.89	1.16	2.63	EXP (79)

**Literature references are indicated; DFT means the reference is based on density functional theory calculations, while EXP means the reference is from experimental results*

Table 3: Calculated Bond Lengths of Square Planar Molecules Compared to Literature Values

Molecule, Fig # in Appendix B	VASP Calculated Bond Length, Å		*Literature Bond Length, Å		*Reference Number
	Metal-C	C-O or C-N	Metal-C	C-O or C-N	
$Ni(CO)_4$, B12 (tetrahedral)	1.81	1.16	1.82	1.15	EXP (80)
$Ni(CN)_4^{2-}$, B13	1.86	1.18	Values could not be found		
$Fe(CN)_4^{3-}$, B14	1.93	1.18	1.89	1.16	EXP (81)
$Os(CN)_4^{3-}$, B15	2.04	1.19	2.07	1.16	EXP (82)
$Ru(CN)_4^{3-}$, B16	2.06	1.19	2.07	1.21	EXP (83)
$Pd(CN)_4^{3-}$, B17	2.01	1.18	1.96	1.15	EXP (84, 85)

** Literature references are indicated; DFT means the reference is based on density functional theory calculations, while EXP means the reference is from experimental results.*

Tables 4, 5, and 6 show our calculated HOMO-LUMO gaps. Many of our calculations had orbitals that were incorrect or incomplete; VASP calculated orbitals with partial occupation levels (between 0 and 1), suggesting that electrons reside somewhere in between multiple orbitals, rather than at distinct energy levels (see Section 3.3.2 below). These incorrect orbitals led to a distortion of the calculated HOMO-LUMO gaps compared to literature. Molecules with incorrect orbitals have been starred in Tables 4 through 6. Among those values with incorrect orbitals, compared with literature, the maximum absolute difference was 3.15 eV, the minimum absolute difference was 0.043, and the mean absolute difference was 1.17 eV. The difference is greatest for $Fe(CN)_6^{4-}$ and $Mn(CN)_6^{4-}$, both charged molecules with cyanide ligands, while the difference is least for $Fe(CO)_3Cl_2$, which is an uncharged molecule with no cyanide ligands. Although we have insufficient information to determine the true cause of this distortion, it indicates we cannot trust density of states for molecules with incorrect orbitals, as they are unpredictable. Therefore, we conclude that having incorrect orbitals gives the greatest distortion to HOMO-LUMO gaps either when the molecule is charged or has certain ligands such as cyanide.

Among the molecules with "correct" orbitals, the maximum difference between calculated values and literature was 0.17 eV, while the minimum difference was 0.0303 eV. The average difference was 0.1098 eV, indicating overall good agreement between our results and literature. The maximum disagreement was in the HOMO-LUMO gap of $Fe(CO)_5$; however, this disagreement has an error of under 5%, as the actual gap is quite large. These molecules with correct orbitals are consistently close to the literature values, making them more accurate than those with incorrect orbitals. In general, the results indicate good calculations of the HOMO-LUMO gaps by VASP for select molecules, and our presented data for correct molecules again can be taken as credible. Calculated density of states graphs can be found for each molecule in Appendix C.

Table 4: Calculated HOMO-LUMO Gaps of Octahedral Molecules Compared to Literature Values

Molecule, Fig # in Appendix C	VASP HOMO-LUMO gap, eV	Literature HOMO-LUMO gap, eV	*Reference Number
†$Fe(CN)_6^{4-}$, C1	0.4841	3.63	DFT (48)
$Co(CN)_6^{4-}$, C2	1.1713	1.328	EXP (72)
†$Mn(CN)_6^{4-}$, C3	1.5851	1.27	EXP (73)
$Cr(CO)_6$, C4	3.9504	3.84	DFT (76)
†$Os(CN)_6^{3-}$, C5	0.3624	Values could not be found	
$Ti(CN)_6^{2-}$, C6	2.3896	Values could not be found	
†$Ru(CN)_6^{3-}$, C7	0.4245	Values could not be found	

**DFT means the reference is based in density functional theory, while EXP means the reference is experimental in nature; Molecules with a † had incorrect orbitals*

Table 5: Calculated HOMO-LUMO Gaps of Trigonal Bipyramidal Molecules Compared to Literature Values

Molecule, Fig # in Appendix C	VASP HOMO-LUMO gap, eV	Literature HOMO-LUMO gap, eV	*Reference Number
$Fe(CO)_5$, C8	3.8899	3.72	EXP (86)
†$Fe(CO)_3Cl_2$, C9	0.5830	0.54	EXP (78)
$Fe(CO)_3Br_2$, C10	0.9103	0.88	EXP (78)
$Fe(CO)_3I_2$, C11	0.7937	0.71	EXP (79)

**DFT means the reference is based in density functional theory, while EXP means the reference is experimental in nature. Molecules with a † had incorrect orbitals*

Table 6: Calculated HOMO-LUMO Gaps of Square Planar Molecules

Molecule, Fig # in Appendix C	VASP HOMO-LUMO gap, eV
$Ni(CO)_4$, C12	4.2857
$Ni(CN)_4^{2-}$, C13	1.8235
†$Fe(CN)_4^{3-}$, C14	0.8472
†$Os(CN)_4^{3-}$, C15	0.2738
$Pd(CN)_4^{3-}$, C16	2.2581
†$Ru(CN)_4^{3-}$, C17	0.3813

Molecules with a † had incorrect orbitals

3.3.2 Issues with Incorrect Atomic Orbitals

Frequently, a calculation converged to a minimum energy, but found an incorrect orbital structure. Such a structure involved band orbitals failing to be either fully occupied or unoccupied, but instead were partially occupied (See Figure 25). In reality, electrons cannot partially occupy a band orbital at low temperature, as they correspond to precise energy levels an electron can occupy. VASP may be generating an erroneous set of orbitals, smearing electrons incorrectly across multiple orbitals, or some other problem. This issue may lead to inaccurate electronic structure and band gap, and in some cases also lead to inaccurate total energy. Many calculations, including ferrocyanide, hexacyanomanganate, hexacyanoosmiate, hexacyanoruthenate, iron(II) tricarbonyl dichloride, iron(II) tricarbonyl diiodide, tetracyanoferrate, tetracyanoosmiate, and tetracyanoruthenate, were affected by incorrect electronic orbitals.

In an attempt to rectify the issue, we changed several parameters in the INCAR files. Setting ALGO = Normal, over the default ALGO = Fast enforced a more rigorous algorithm, requiring more time from the computation, but increasing the likelihood of convergence. If this step failed, a non-self-consistent check was performed by adding ICHARG = 12, which asks VASP to find the superposition of atomic charge densities. A failure to converge on this check indicated a serious issue with the calculation. If the check converged successfully, the mixing parameters AMIX and BMIX were changed, starting with AMIX = 0.1 and BMIX = 0.01. These parameters guide how the algorithm approaches convergence. See the VASP Guide for more details (87). Of all the molecules affected, only iron(II) tricarbonyl diiodide's orbitals were corrected through these

steps. A further effort to use the tetrahedron method by changing the ISMEAR line in the INCAR file from 0 to -5 and setting the k-points to a 4x4x4 mesh allowed ferrocyanide to converge without partial occupancy in the molecular orbitals. However, this converged ferrocyanide gave a band gap of 0.022 eV, which still disagrees with the literature value of 3.63 eV (48). Further investigation is required to determine the effectiveness of the tetrahedron method. Also, an upgrade to VASP 5.4.4 and a GPU version of VASP during our research increased the difficulty in diagnosing the convergence problems. Diagnosing and attempting to correct these convergence issues was a primary setback of our work.

spin component 1

k-point 1 : 0.0000 0.0000 0.0000

band No.	band energies	occupation
1	-18.3572	1.00000
2	-18.2623	1.00000
3	-18.2584	1.00000
4	-18.2541	1.00000
5	-18.2246	1.00000
6	-18.2200	1.00000
7	-9.4934	1.00000
8	-7.1548	1.00000
9	-7.1515	1.00000
10	-7.1476	1.00000
11	-7.1119	1.00000
12	-7.1074	1.00000
13	-5.3140	1.00000
14	-5.3099	1.00000
15	-5.3070	1.00000
16	-4.9930	1.00000
17	-4.9007	1.00000
18	-4.8987	1.00000
19	-4.8932	1.00000
20	-4.8476	1.00000
21	-4.8457	1.00000
22	-4.3524	1.00000
23	-4.3475	1.00000
24	-4.3467	1.00000
25	-4.0404	1.00000
26	-4.0383	1.00000
27	-4.0348	1.00000
28	-3.6384	1.00000
29	-3.6373	1.00000
30	-3.6353	1.00000
31	-2.0410	0.99694
32	-1.8837	0.69689
33	-1.8758	0.65686
34	-1.8743	0.64931
35	-1.3210	0.00000
36	-1.2959	0.00000
37	-1.2181	0.00000

Figure 25: An excerpt from an OUTCAR file demonstrating the failure of band occupation to converge. In this band occupation graph, each band should be either occupied (right column = 1) or unoccupied (right column = 0). Note that orbitals 31-34 have "partial occupancy," indicating that the calculation could not determine whether they were occupied.

3.4 Adsorbed Complexes

Once the lowest energy gas-phase geometries of the organometallic molecules and the anatase surface were determined, we adsorbed molecules to the titanium dioxide surface. For each molecule, six different initial adsorption geometries were created in an attempt to test for the many different possible adsorption configurations. Of the final optimized geometries, the lowest energy geometry was used to calculate the density of states.

3.4.1 Chromium Hexacarbonyl

Figure 26 shows the most stable configuration of chromium hexacarbonyl over TiO_2. Two equatorial oxygens of chromium hexacarbonyl adhered to titanium atoms on the surface of titanium dioxide. This bond has a weak binding energy of 0.21 eV, and bond lengths of 2.54 and 2.74 Å between oxygen atoms of chromium hexacarbonyl and titanium atoms of the anatase surface. This bidentate bond is not likely strong enough to hold the chromium hexacarbonyl to the surface in aqueous solution. Bonds between water molecules (O-H bonds) have an energy of about 0.24 eV (88), which suggests that carbonyl groups may have similar bonding energies between the carbonyl O and water H atoms. Thus, the bonding strength of chromium hexacarbonyl to water and the TiO2 surface are of similar magnitudes. A better ligand should be sought out in order to stronger bind complexes to the surface.

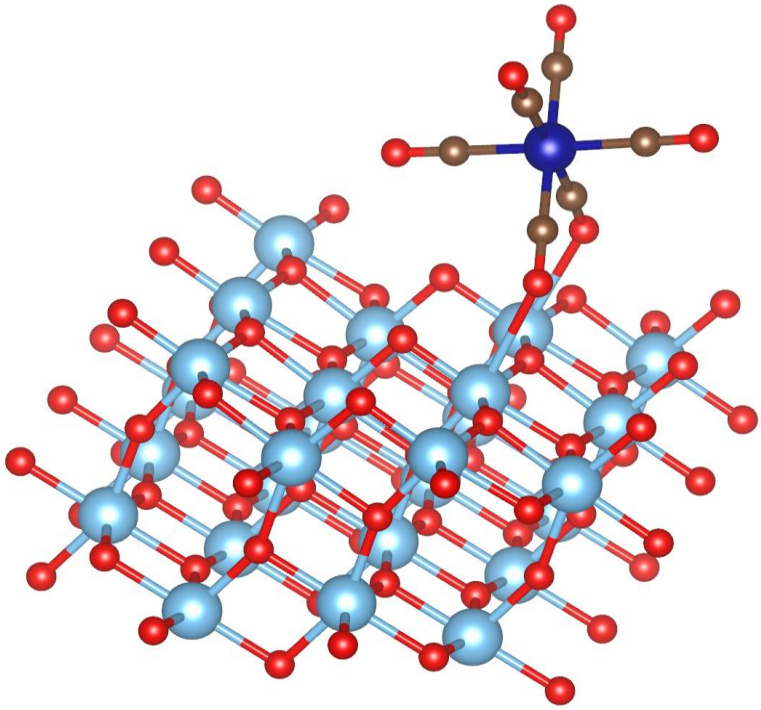

Figure 26: Geometry D, chromium hexacarbonyl's best bonding geometry with titanium dioxide.

Figure 27 shows the other converged geometries for $Cr(CO)_6$, three of which are monodentate, one bidentate, and one tridentate. The bond lengths and binding energies are shown in Table 7. As demonstrated in Figure 27, geometries A through C actually converged to very

similar configurations, with an oxygen interacting with a raised titanium atom on the surface. Geometries D through F are quite similar as well, angled so three oxygen atoms are potentially weakly interacting with the surface. The binding energies, all under 0.25 eV, indicate that the bond is weak between the oxygen atoms and titanium surface, however. Monodentate geometries A and C have a binding energy of 0.17 eV at a bond length around 2.45 Å, while bidentate geometry D has a bonding energy of 0.21 eV for a similar bond length of 2.54 Å. This indicates that bidentate bond geometry is more effective in the case of carbonyl groups. Regardless, carbonyl groups in chromium hexacarbonyl bond weakly with the titanium dioxide surface.

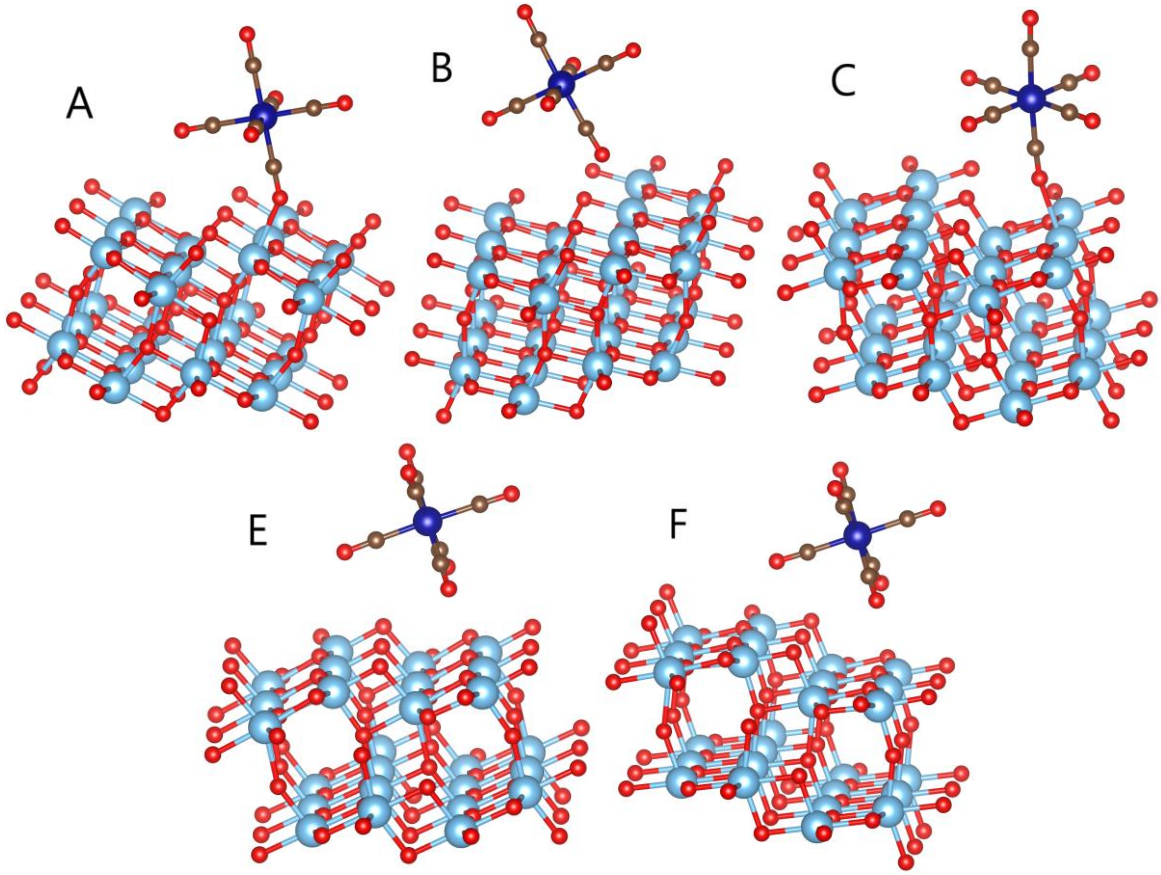

Figure 27: Converged adsorption geometries studied for chromium hexacarbonyl. Each geometry is labeled as it appears in Table 7.

Table 7: Calculated Bond Lengths for Chromium Hexacarbonyl Adsorbed to Anatase

$Cr(CO)_6$ Geometry	Bond Formation (Adsorbate - Surface)	Bond Length(s), Å	Binding Energy, eV (Positive is better)
A	O - Ti	2.47	0.17
B	O - Ti	3.56	0.03
C	O - Ti	2.42	0.17
D (Optimal)	2x O - Ti	2.74 & 2.54	0.21
E	2x O - O	3.18 & 3.26	0.06
F	3x O – Ti	3.19 & 3.26 & 3.31	0.08

Figure 28 shows the calculated density of states for the selected optimal geometry (shown in Figure 26). The states from the titanium dioxide slab are clearly visible, with the valence band from around -5 to 0 eV, and excited states above 2.5 eV. This surface has a band gap of 2.58 eV, very similar to the lone anatase slab, indicating that the chromium hexacarbonyl may not provide any useful benefits for photoexcitation. Chromium hexacarbonyl bands around -5 and -1 eV, as well as at 3 eV, places them below and above the existing titanium dioxide energy bands, respectively. There appears no benefit to having chromium hexacarbonyl present, since any photoexcited electrons would jump from the HOMO of TiO_2 to the LUMO of TiO_2 (same energy as pure TiO_2) or jump from the HOMO of chromium hexacarbonyl to LUMO of TiO_2 (more energy than pure TiO_2). Excitation from the HOMO of chromium hexacarbonyl to LUMO of chromium hexacarbonyl requires even more energy. Thus, the chromium hexacarbonyl system requires just as much energy as pure anatase slab to excite electrons, and chromium hexacarbonyl binds poorly to anatase, so we conclude that chromium hexacarbonyl would be a poor choice for a photosensitizer.

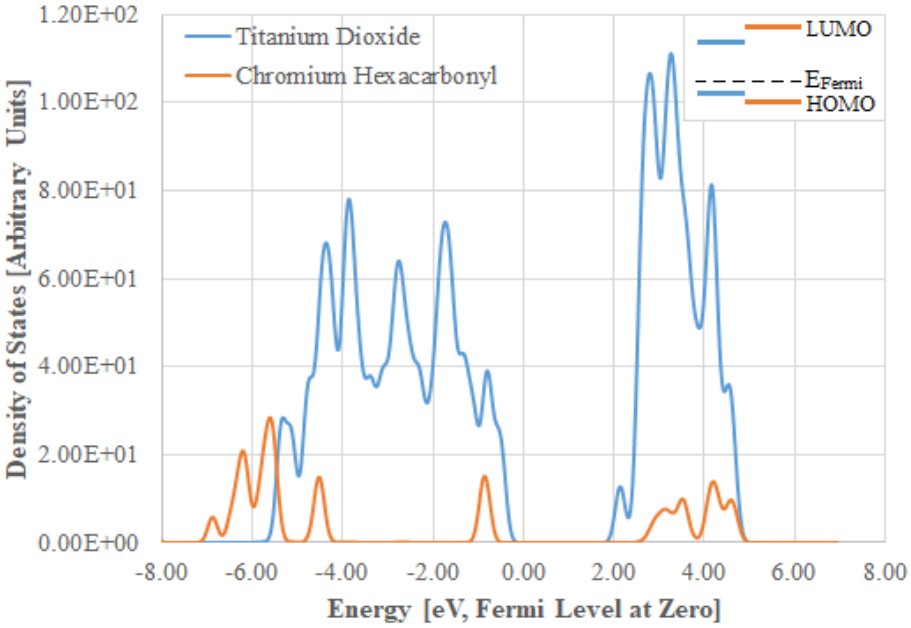

Figure 28: Calculated density of states for chromium hexacarbonyl adsorbed to the titanium dioxide surface. Electronic titanium dioxide states are shown in blue, while chromium hexacarbonyl states are shown in orange.

3.4.2 Iron Pentacarbonyl

Figure 29 shows the most stable configuration of iron pentacarbonyl over TiO_2. An equatorial oxygen of iron pentacarbonyl bonded to a titanium atom on anatase. This bond has a weak binding energy of 0.16 eV and a bond length of 2.44 Å between the oxygen atom on the ligand and a titanium atom on the surface. This monodentate bond will also probably not hold together in aqueous solution, further reinforcing the idea that carbonyl groups do not bond well with the titanium dioxide surface, and a better ligand is needed. Interestingly, this bond is monodentate, while chromium hexacarbonyl's best bond with the surface was bidentate; this likely indicates the trigonal bipyramidal geometry of iron pentacarbonyl does not lend itself well to bidentate bonds.

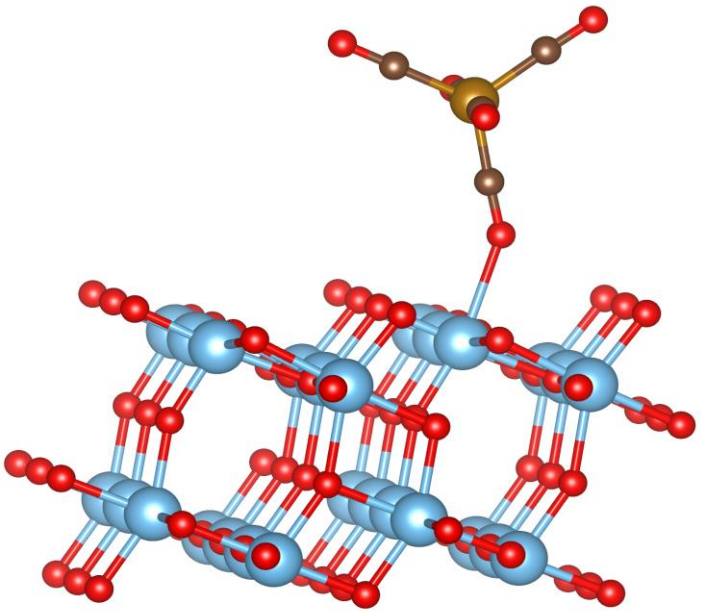

Figure 29: Geometry C, iron pentacarbonyl's best bonding geometry with titanium dioxide.

Figure 30 shows the other converged geometries for iron pentacarbonyl, two of which are monodentate and three of which are bidentate. The bond lengths and binding energies are shown in Table 8. Geometries A through C actually converged to similar configurations, with an oxygen atom interacting with a raised titanium atom. These geometries have binding energies in the range of 0.12 - 0.16 eV, and around 2.5 Å away from the surface. Geometries D and E are quite similar as well, although an equatorial and axial carbonyl bonded to the surface in geometry D while two equatorial carbonyl groups bonded to the surface in geometry E. Geometry F involves two carbonyl groups bonding across an oxygen bridge in anatase. The presence of the bridge is likely the cause of the long distances in this geometry. Geometries D and F both have binding energies around 0.18 eV, but they are farther away, around 2.70 Å. This indicates that the geometry of iron pentacarbonyl makes two bonds with the surface impractical, unlike chromium hexacarbonyl. Geometry E especially indicates this, being pushed to 3 Å away from the surface, and having a binding energy of 0.12 eV, even less than the other geometries.

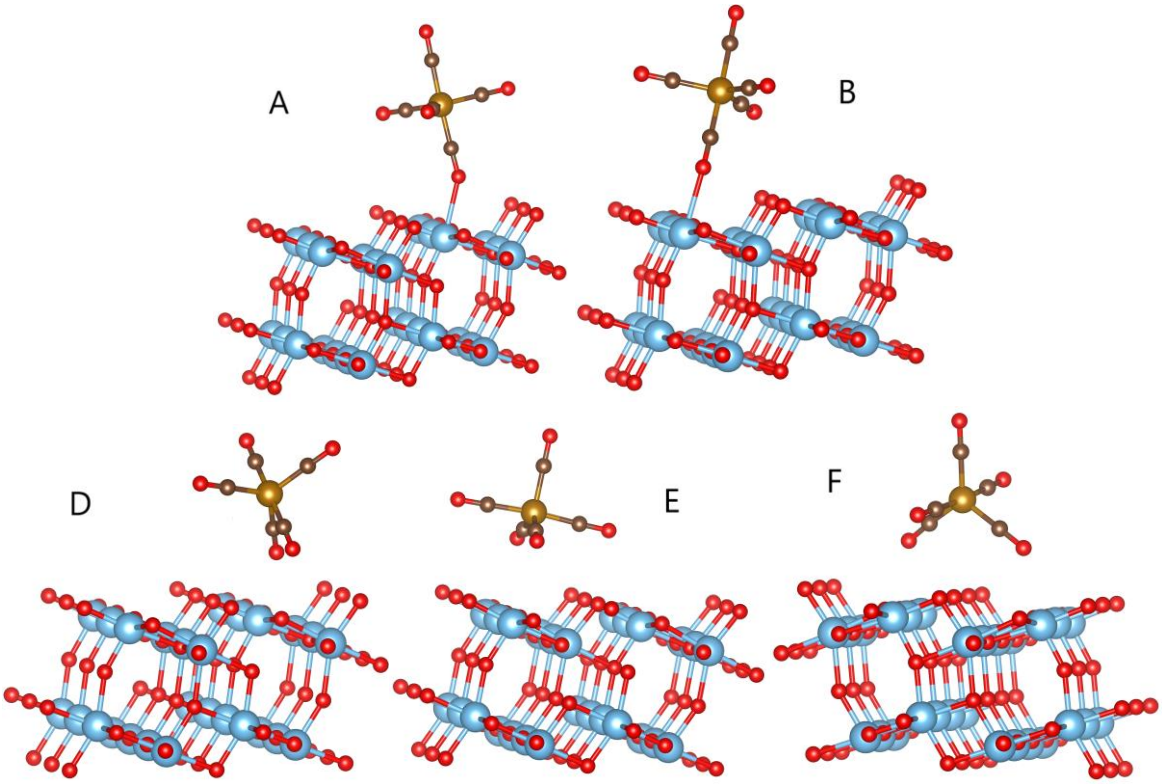

Figure 30: Different adsorption geometries studied for iron pentacarbonyl. Each geometry is labeled as it appears in Table 8.

Table 8: Calculated Bond Lengths for Iron Pentacarbonyl Adsorbed to Anatase

$Fe(CO)_5$ Geometry	Bond Formation (Adsorbate - Surface)	Bond Length(s), Å	Binding Energy, eV (Positive is better)
A	O - Ti	2.5	0.12
B	O - Ti	2.51	0.15
C (Optimal)	O - Ti	2.44	0.16
D	2x O - Ti	2.62 & 2.99	0.17
E	2x O - Ti	3.00 & 3.06	0.12
F	O - Ti, O – O	2.70 & 2.98	0.19

Figure 31 shows the calculated density of states for the selected optimal geometry. In addition to the states contributed by titanium dioxide, iron pentacarbonyl contributes electron states around -6, -2, -0.5, and 3 - 5 eV on the chart. The HOMO of iron pentacarbonyl at -0.5 eV, similar to the HOMO of titanium dioxide. This close energy level could indicate that

electrons/holes could exchange between the two orbitals easily. The LUMO of iron pentacarbonyl resides at ~3 eV, higher than that of titanium dioxide at ~2 eV. There appears no benefit to having iron pentacarbonyl present, since any photoexcited electrons would jump from the HOMO of TiO_2 to the LUMO of TiO_2 (same energy as pure TiO_2) or jump from the HOMO of iron pentacarbonyl to LUMO of TiO_2 (more energy than pure TiO_2). Excitation from the HOMO of iron pentacarbonyl to LUMO of iron pentacarbonyl requires even more energy. Therefore, iron pentacarbonyl is not helpful with photoexcitation. The substitution of chromium with iron added states at -2 eV but did not place any states inside or near enough to titanium bands to enable photosensitization. Similar to chromium hexacarbonyl, a combination of poor adhesion to the surface and negligible potential as a photosensitizer indicates that iron pentacarbonyl makes for a poor choice in this effort. Using carbonyl ligands therefore does not look promising.

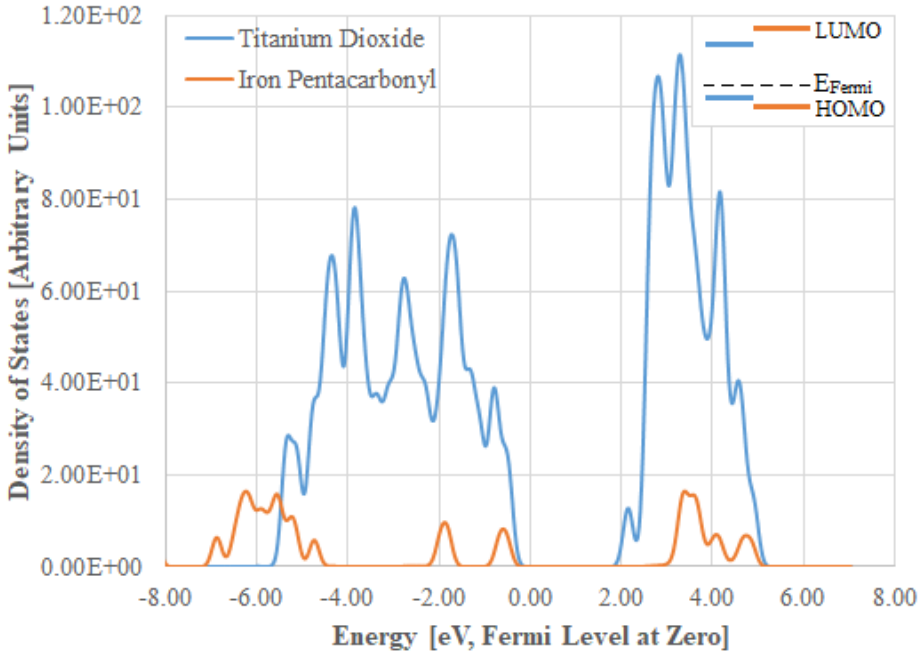

Figure 31: Calculated density of states for iron pentacarbonyl adsorbed to the titanium dioxide surface for the most stable geometry. Electronic contributions from titanium dioxide are shown in blue, while contributions from iron pentacarbonyl are shown in orange.

3.4.3 Iron(II) Tricarbonyl Diiodide

We now considered another molecule which is a variation of iron pentacarbonyl, that has two iodine atoms and three carbonyl groups, or iron(II) tricarbonyl diiodide. Figure 32 shows the most stable configuration of iron(II) tricarbonyl diiodide over TiO_2. The equatorial oxygen of iron tricarbonyl diiodide adhered to a titanium atom on the TiO_2 surface. This bond has a weak binding energy of 0.16 eV, and a bond length of 2.44 Å between the iron in the adsorbate and a slightly displaced oxygen atom on the surface. This bond is not likely strong enough to hold together in aqueous solution. Iron bonds directly to the surface and the molecule essentially changes into an octahedral structure, indicating how much stronger the Fe-O bond is than a C-O-Ti bond, as in the

previous two molecules. However, the bond energy is still weak. possibly because the adsorbed molecule becomes severely bent to form an octahedral structure. Interestingly, an oxygen atom of anatase is pulled out of position by 0.02 Å to form this bond.

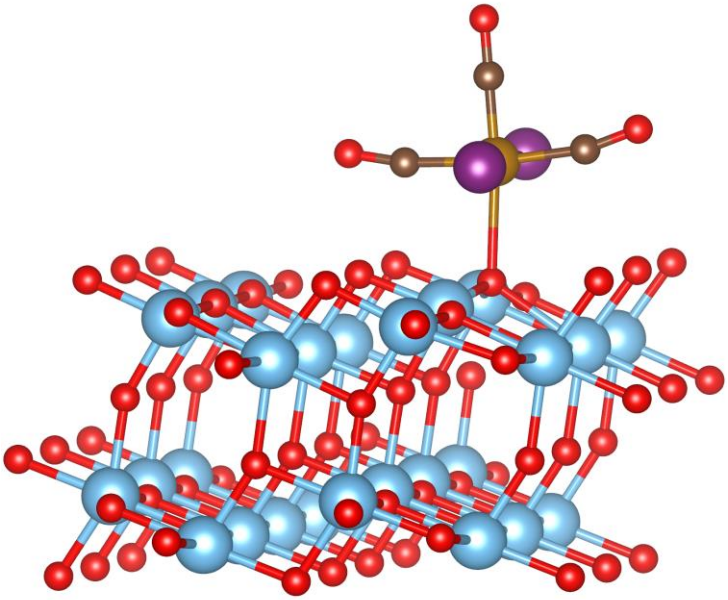

Figure 32: Geometry F, iron(II) tricarbonyl diiodide's best bonding geometry with titanium dioxide.

Figure 33 shows the other converged geometries for $Fe(CO)_3I_2$, all five of which can be considered monodentate. The bond lengths and binding energies are shown in Table 9. The molecules converged to a wide array of geometries, indicating that the molecule could interact with the surface in a number of different ways. However, the carbonyl groups generally interacted with the surface more than the iodide atoms. Binding energies were all below 0.25 eV, indicate that only weak interactions take place. This further reinforces the idea that carbonyl groups will not bond to the titanium dioxide surface. Furthermore, iodide ligands resist bonding to the surface more than carbonyl ligands. Geometry E has a binding energy of 0.24 eV, but the O-Ti bond length of 2.68 Å is rather long. The Fe-O bond in Geometry F has comparable binding energy to other monodentate C-O-Ti or I-Ti bonds despite the change in geometry, indicating that a direct metal-to-surface bond is preferable to these two ligands.

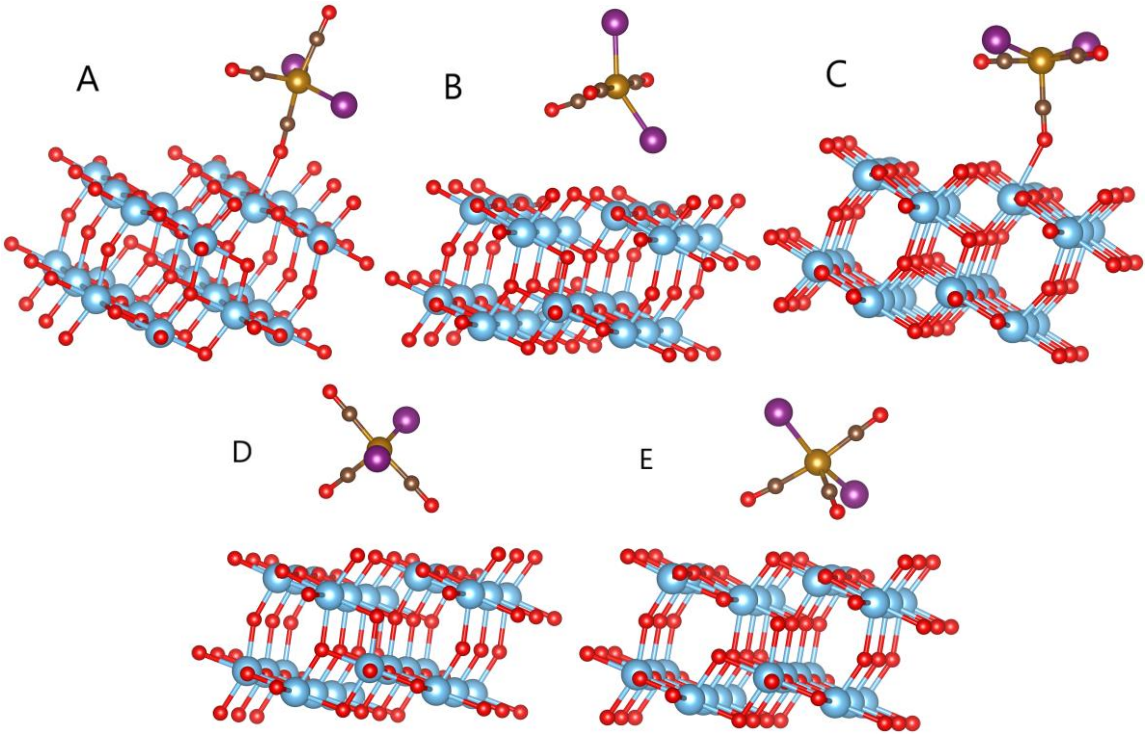

Figure 33: Different adsorption geometries studied for iron(II) tricarbonyl diiodide. Each geometry is labeled as it appears in Table 9.

Table 9: Calculated Bond Lengths for Iron(II) Tricarbonyl Diiodide Adsorbed to Anatase

$Fe(CO)_3I_2$ Geometry	Bond Formation (Adsorbate - Surface)	Bond Length(s), Å	Binding Energy, eV (Positive is better)
A	O - Ti	2.45	-0.22
B	I - Ti	3.3	0.15
C	O - Ti	2.46	0.13
D	O - Ti	2.8	0.09
E	O - Ti	2.68	0.23
F (Optimal)	Fe – O	2.43	0.16

Figure 34 shows the calculated density of states for the selected optimal geometry. In addition to the states from the anatase slab, states from $Fe(CO)_3I_2$ appear at -8 to -6 eV, -2 eV, a HOMO just below 0 eV, a LUMO at 1 eV, and states at 1.5 eV and 3 to 4 eV. This places the $Fe(CO)_3I_2$ band gap around 1 eV. The HOMO band of titanium dioxide is around -1 eV, while its LUMO appears at 1.5 eV, giving a band gap of 2.5 eV. Light may excite electrons from the HOMO

of $Fe(CO)_3I_2$ to its LUMO, and more energetic light, or another photon of 0.5 eV, could send those electrons into the LUMO of anatase, where they become available for reaction. Thus, photoexcitation appears easier for this system than pure anatase, around 1.53 eV, so visible light excitation may be possible. Although this means $Fe(CO)_3I_2$ has significant potential as a photosensitizer, it forms a poor bond with the surface. This indicates that electrons would be struggling to reach anatase if $Fe(CO)_3I_2$ molecules were in solution rather than bound to the surface. A better anchor for this molecule may be needed to stabilize it to the surface.

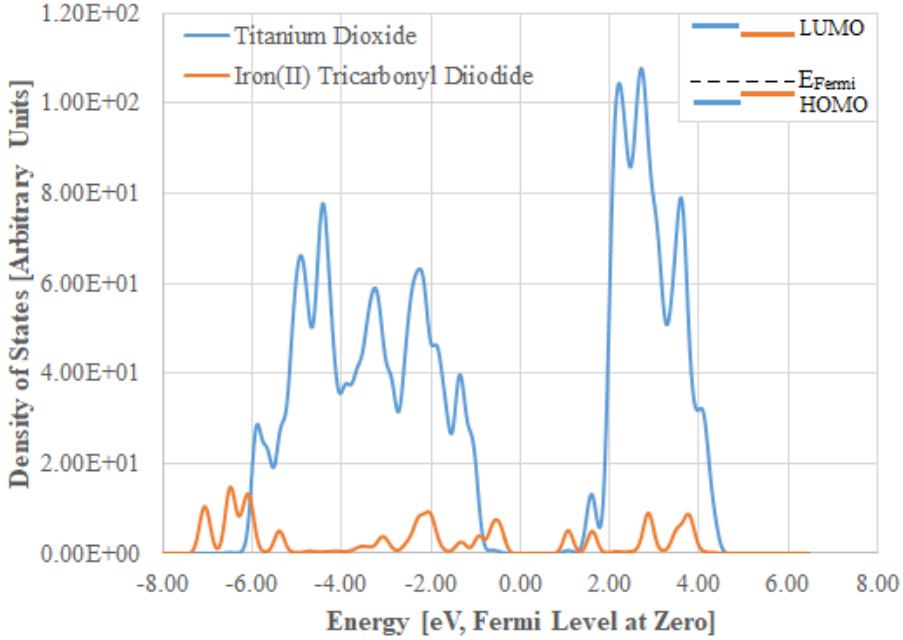

Figure 34: Calculated density of states for iron(II) tricarbonyl diiodide adsorbed to the titanium dioxide surface. Electronic contributions from titanium dioxide are shown in blue, while contributions from iron(II) tricarbonyl diiodide are shown in orange.

3.4.4 Iron(II) Tricarbonyl Dibromide

To examine the effect of changing halides from iodine to bromine, we next simulated iron(II) tricarbonyl dibromide. Figure 35 shows the most stable configuration of iron(II) tricarbonyl dibromide over TiO_2. Similar to iron(II) tricarbonyl diiodide, the organometallic adsorbate iron(II) tricarbonyl dibromide assumed an octahedral geometry, allowing the iron atom to bond to an oxygen atom on the anatase surface, displacing it upward by 0.02 Å. This monodentate bond has a binding energy of 0.59 eV, and a bond length of 2.25 Å, significantly stronger and closer to the surface than the other bond lengths considered thus far. The strength of this bond indicates that changing ligands increase the binding energy with titanium dioxide and a possible way to increase binding of the photosensitizer. The significant difference between bromine and iodine demonstrates how the larger size of iodine atoms interferes with the bonding of the molecule.

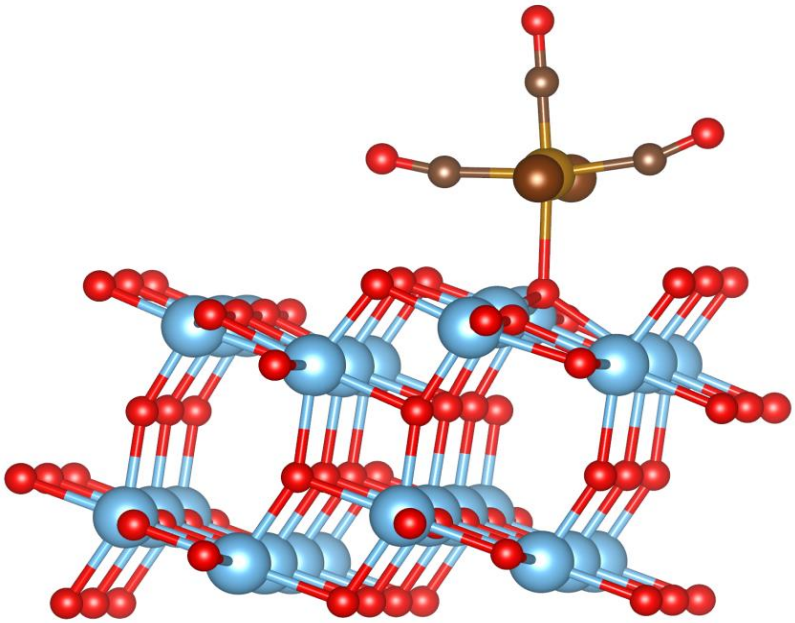

Figure 35: Geometry F, iron(II) tricarbonyl dibromide's best bonding geometry with titanium dioxide.

Figure 36 shows the other converged geometries for $Fe(CO)_3Br_2$, all of which are effectively monodentate. The bond lengths and binding energies are shown in Table 10. As demonstrated in Figure 36, geometries B and E converged to similar geometries, with a bromine atom interacting with a surface titanium atom at a bond length of ~2.9 Å and energy of ~0.23 eV. Geometries A, C, and D, converged to geometries where a carbonyl group interacted with a titanium atom on the surface, achieving comparatively shorter bond lengths of ~2.6 Å but much smaller energies of ~0.10 eV. The polar halides therefore are more effective at bonding to the surface than carbonyl groups in general. Compared to $Fe(CO)_3I_2$, $Fe(CO)_3Br_2$ shows more promise in binding to the surface, as the Br atom is smaller and more suited to forming stronger bonds with the anatase surface. The trigonal bipyramidal geometry and large ligands of $Fe(CO)_3Br_2$ prevented any bidentate geometries from occurring; this parallels the geometries formed by $Fe(CO)_3I_2$. Halides, therefore, increase the bonding potential with the anatase surface, so long as they are not so large as to interfere with bonding.

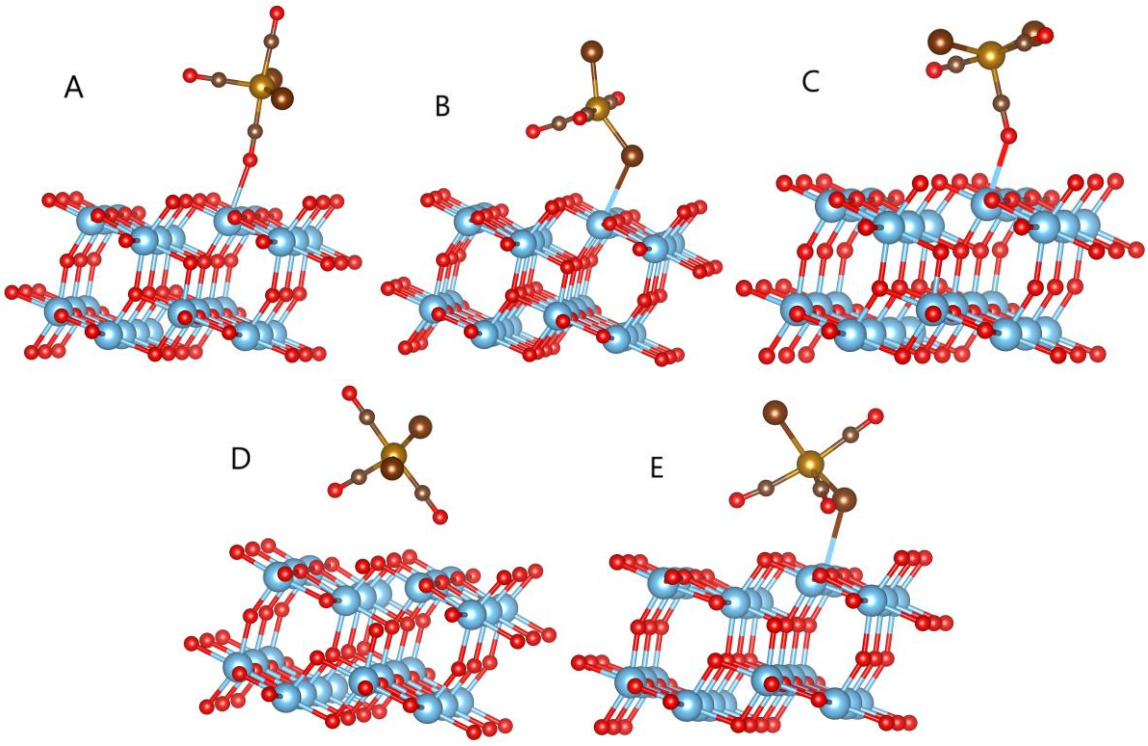

Figure 36: Converged adsorption geometries studied for iron(II) tricarbonyl dibromide. Each geometry is labeled as it appears in Table 10.

Table 10: Calculated Bond Lengths for Iron(II) Tricarbonyl Dibromide Adsorbed to Anatase

$Fe(CO)_3Br_2$ Geometry	Bond Formation (Adsorbate - Surface)	Bond Length(s), Å	Binding Energy, eV (Positive is better)
A	O - Ti	2.57	0.08
B	Br - Ti	3.07	0.20
C	O - Ti	2.5	0.12
D	O - Ti	2.81	0.08
E	Br - Ti	2.81	0.27
F (Optimal)	Fe – O	2.25	0.59

Figure 37 shows the calculated density of states for the selected optimal geometry (shown in Figure 35). The states from anatase are overlapped by states from $Fe(CO)_3Br_2$, which range from -7 to -0.25 eV, where its HOMO is located. $Fe(CO)_3Br_2$ has a LUMO at 1.5 eV, and more bands at 2, 3, and 4 eV. The band gap of $Fe(CO)_3Br_2$ is therefore around 1.85 eV. The HOMO of titanium dioxide is around -0.75 eV, while its LUMO appears at 1.75 eV, maintaining its band gap

is 2.5 eV. Light may excite electrons from the HOMO of titanium dioxide into the LUMO of $Fe(CO)_3Br_2$ with an energy requirement of about 2.25 eV, which is not much lower than the standard band gap of TiO_2. However, light excited from the HOMO of $Fe(CO)_3Br_2$ into its LUMO requires less energy; these electrons are then available for further excitation into the LUMO of TiO_2, with an energy requirement of 0.5 eV. Therefore, photoexcitation appears easier for this system than for pure anatase, around 1.85 eV, so visible light excitation is possible. This means that $Fe(CO)_3Br_2$ has significant potential as a photosensitizer, and also has a relatively strong bond with the surface, making it an excellent candidate.

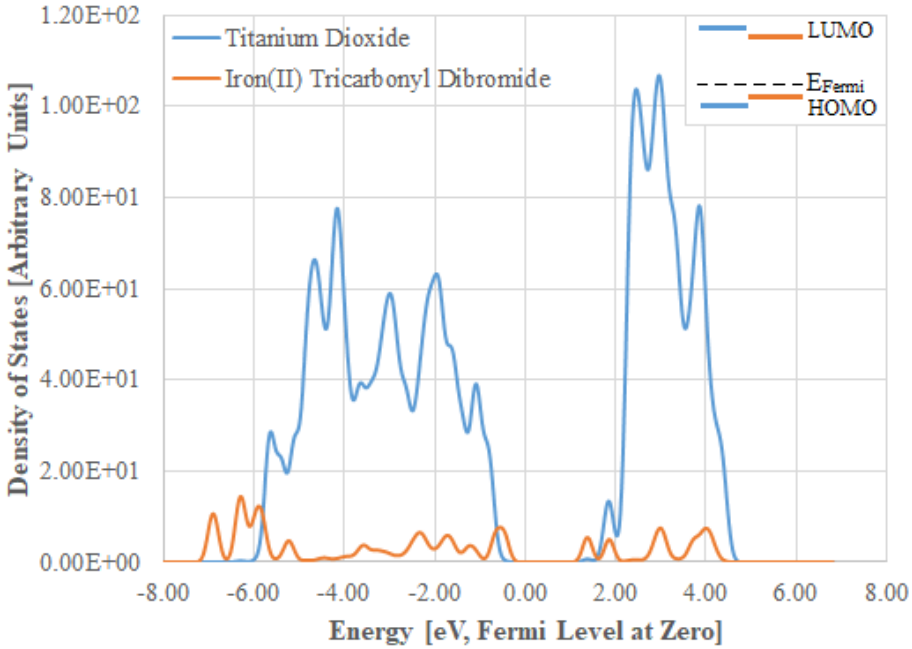

Figure 37: Calculated density of states for iron(II) tricarbonyl dibromide adsorbed to the titanium dioxide surface. State contributions from titanium dioxide are shown in blue, while contributions from iron(II) tricarbonyl dibromide are shown in orange.

3.4.5 Nickel Tetracarbonyl

Figure 38 shows the most stable configuration of nickel tetracarbonyl over TiO_2. One oxygen atom of nickel tetracarbonyl bonded to a titanium atom on anatase. This bond has a weak binding energy of 0.13 eV and a bond length of 2.58 Å between the oxygen atom on the ligand and the titanium atom on the surface. This monodentate bond will probably not hold together in aqueous solution, as it is a carbonyl group, which we have previously seen bonds poorly to the titanium dioxide surface, requiring a better ligand. This bond is monodentate, compared to chromium hexacarbonyl's bond, which was bidentate, and iron pentacarbonyl's bond, which was also monodentate. The reason is likely the same as in iron pentacarbonyl; the tetrahedral geometry prohibits bidentate bonds.

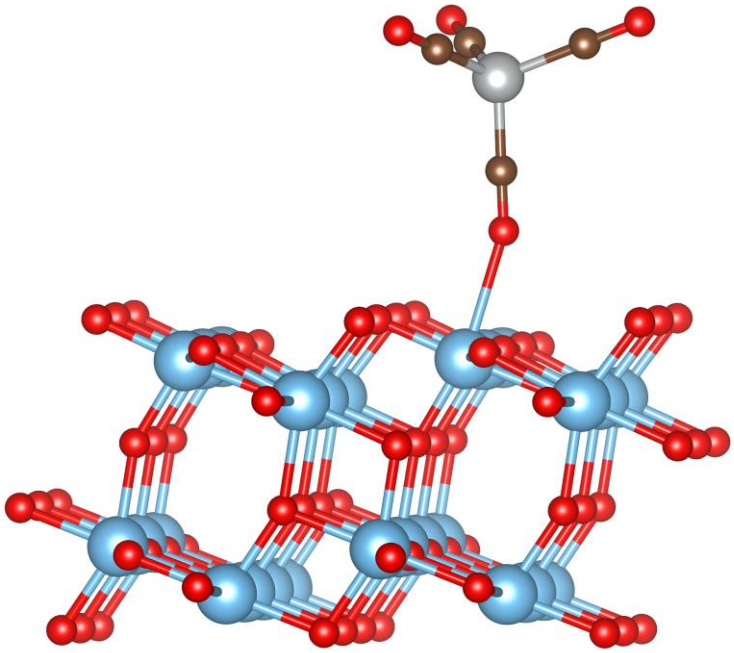

Figure 38: Geometry A, nickel tetracarbonyl's best bonding geometry with titanium dioxide.

Figure 39 shows the other converged geometries for nickel tetracarbonyl, four of which are monodentate and one of which is bidentate. The bond lengths and binding energies are shown in Table 11. Interestingly, geometry B is basically identical to geometry A, with a carbonyl group interacting with a raised titanium atom. These two geometries have binding energies of 0.13 eV and bond lengths of 2.58 Å. Geometries C and D are similar in that a solo carbonyl group interacts with the surface, but geometry C is attempting to interact with a lower titanium atom and geometry D is attempting to interact with a raised oxygen. Both geometries have a bond length around 3.2 Å and binding energy of basically 0 eV, so in these instances the nickel tetracarbonyl simply floats above the surface. Geometry E features two carbonyl groups attempting to bond to raised titanium atoms in the same row; bond lengths of 3.2 Å and 3.3 Å and binding energy of 0.05 eV in this geometry indicate that bonding is unsuccessful. Geometry F is a more stable orientation with a binding energy of 0.14 eV; unfortunately, the carbonyl group interacts with a titanium atom at a distance of 2.68 Å, which is rather long for a bond. This indicates that bidentate bonds are quite impractical between nickel tetracarbonyl and titanium dioxide, as in iron pentacarbonyl; the only one that is close to a bidentate bond is geometry E, which has a very low energy and large bond distance.

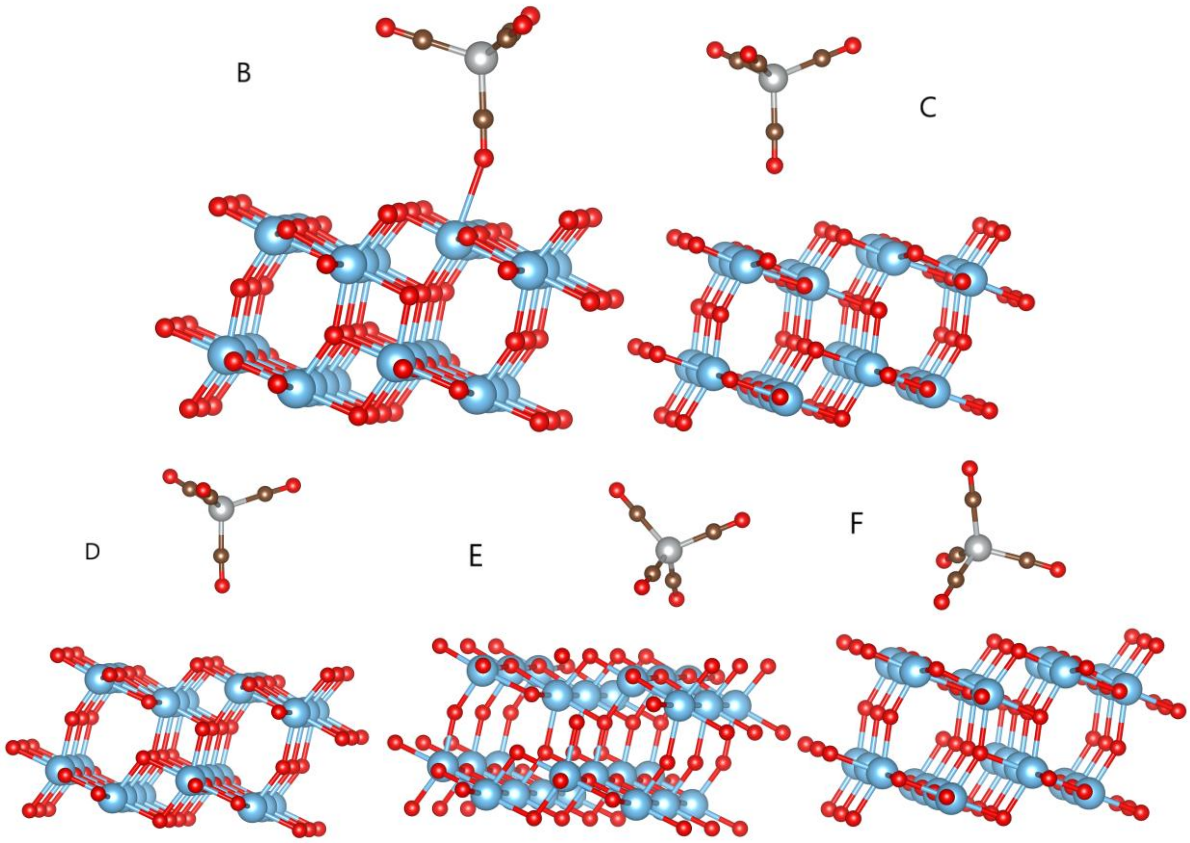

Figure 39: Different adsorption geometries studied for nickel tetracarbonyl. Each geometry is labeled as it appears in Table 11.

Table 11: Calculated Bond Lengths for Nickel Tetracarbonyl Adsorbed to Anatase

$Ni(CO)_4$ Geometry	Bond Formation (Adsorbate - Surface)	Bond Length(s), Å	Binding Energy, eV (Positive is better)
A (Optimal)	O - Ti	2.58	0.13
B	O - Ti	2.58	0.13
C	O - Ti	3.22	0.01
D	O - O	3.2	0.00
E	O - Ti & O - Ti	3.16 & 3.26	0.05
F	O – Ti	2.68	0.14

Figure 40 shows the calculated density of states for the selected optimal geometry (shown in Figure 38). In addition to states from anatase, the nickel tetracarbonyl contributes electron states

around -6 to -5, -2, -1, and 3.5 to 4.5 eV on the chart. The HOMO of nickel tetracarbonyl, at -1 eV, is just 0.5 eV below the HOMO of titanium dioxide. This energy level indicates that electrons could move between the two orbitals. The LUMO of nickel tetracarbonyl is at ~3.5 eV, significantly higher than that of titanium dioxide at ~2 eV. The results indicate that there is no benefit to having nickel tetracarbonyl present; the electrons could excite from the HOMO of TiO_2 to the LUMO of TiO_2 with the same energy as pure TiO_2 requires. Excitation from the HOMO of $Ni(CO)_4$ to the LUMO of TiO_2 requires even more energy. Therefore, nickel tetracarbonyl is unhelpful with photoexcitation. The substitution of iron with nickel, compared to iron pentacarbonyl, seems to shift the HOMO down by a small amount, but does not significantly change the band structure. Similar to chromium hexacarbonyl and iron pentacarbonyl, nickel tetracarbonyl is a poor choice as a photosensitizer because it cannot bond well to the surface and that it does little to improve photoexcitation.

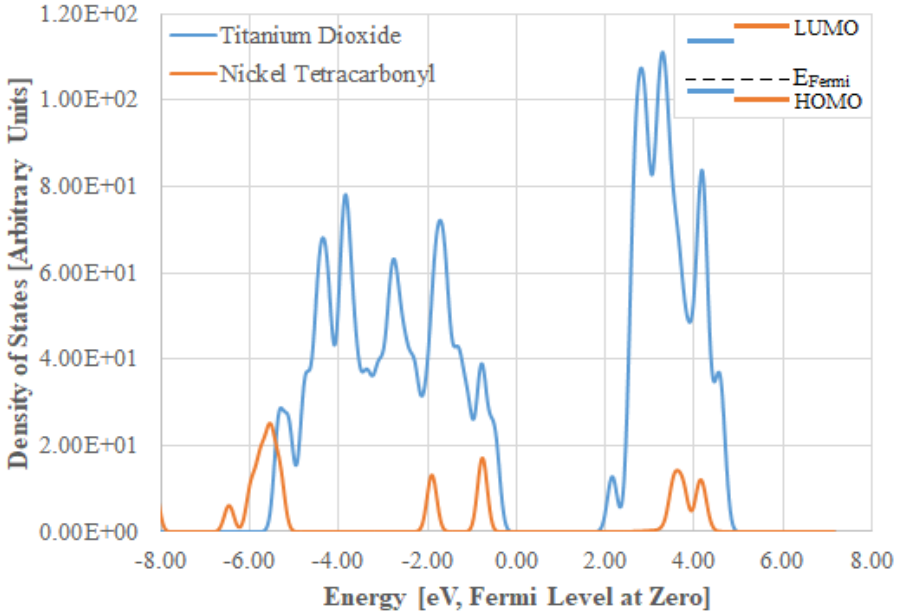

Figure 40: Calculated density of states for nickel tetracarbonyl adsorbed to the titanium dioxide surface for the most stable geometry. Electronic states from titanium dioxide are shown in blue, while contributions from nickel tetracarbonyl are shown in orange.

3.4.6 Tetracyanonickelate

To examine the effect of changing ligands from carbonyl to cyanide, we next simulated tetracyanonickelate. Figure 41 shows the most stable configuration of $Ni(CN)_4^{2-}$ over TiO_2. The $Ni(CN)_4$-TiO_2 system was modeled with a net charge of -2, as well as the lone $Ni(CN)_4$ molecule. Similar to chromium hexacarbonyl, the adsorbate assumed a bidentate bond with two raised titanium atoms. This bond has bond lengths of 2.15 Å, the closest bond observed thus far. This system is charged, introducing error in VASP's energy calculation of the system (8); this resulted in a certainly inaccurate binding energy of -2.21 eV. This binding energy suggests a strong repulsive force from the surface of anatase, which if true would have forced the tetracyanonickelate

to float above the surface rather than attaching quite closely to it as in this geometry. Therefore, the binding energy is unknown. Increasing the lattice height and affording more distance between this anatase slab and the one generated from periodic boundary conditions above it, would reduce this error in the calculation. Due to the ionic interactions, tetracyanonickelate should bind more strongly to the surface than other considered molecules.

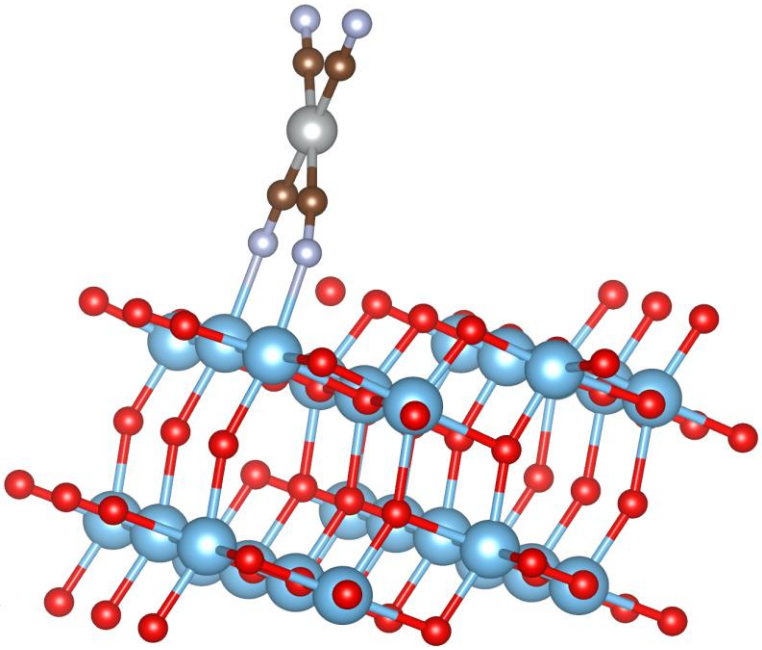

Figure 41: Geometry E, tetracyanonickelate's most stable bonding geometry with titanium dioxide.

Figure 42 shows the other converged geometries for $Ni(CN)_4^{2-}$. Two of these are monodentate and three bidentate, and their bond lengths and distorted binding energies are shown in Table 12. Geometries A and B converged similarly, with a single nitrogen atom interacting with a raised titanium atom at a distance of ~2.06 Å and energy of ~-3.60 eV. Geometries C, D, and E are also very similar, with two nitrogen atoms bonding with raised titanium atoms at distances of ~2.14 Å and energies of ~-2.22 eV. The parallels between similar geometry and similar energy indicates that the program may distort bond energy in a predictable way, so those bonds of geometries C, D, and E are actually stronger than the bonds of geometries A and B. An outlier is geometry F, which features a distorted square planar geometry in order for opposed nitrogen atoms to bond to titanium atoms on the surface. This geometry has a longer distance of 2.30 Å and lower energy of -4.02 eV, so it is unlikely to be the strongest bond of the set. Interestingly, although the nickel atom was exposed and could have bonded to titanium itself, all geometries featured nitrogen bonding to titanium atoms.

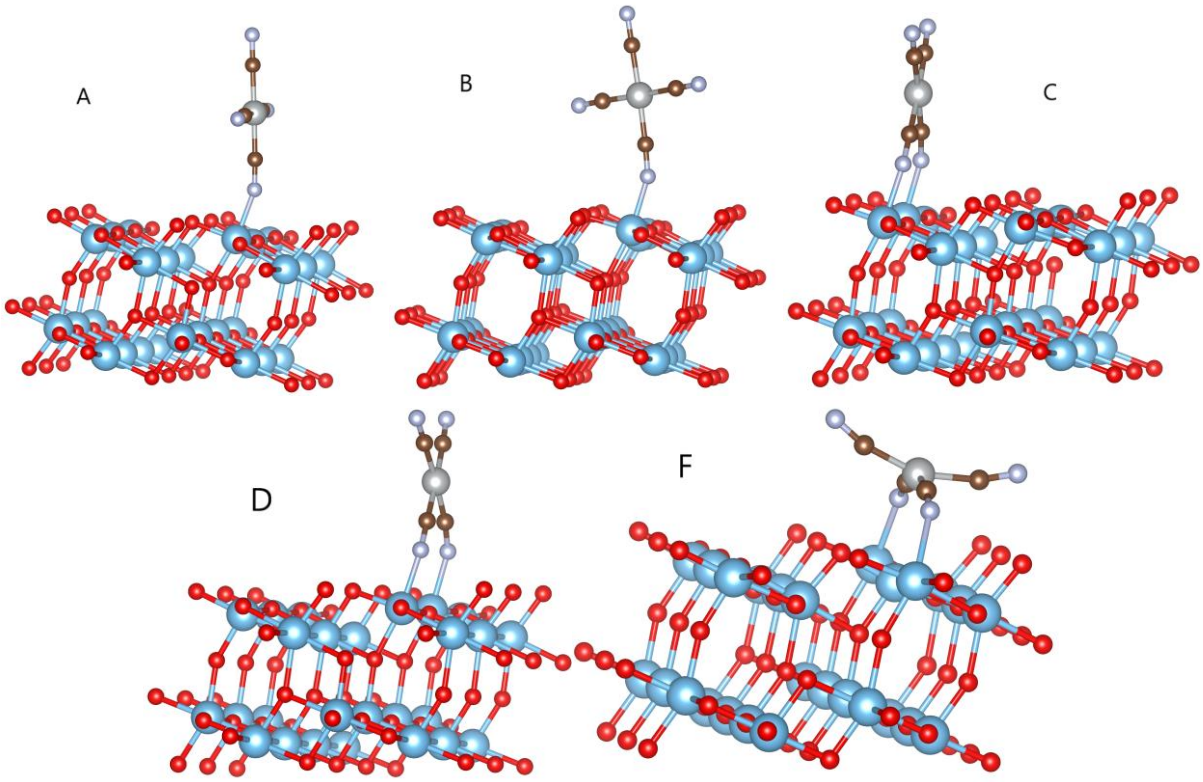

Figure 42: Converged adsorption geometries studied for tetracyanonickelate. Each geometry is labeled as it appears in Table 12.

Table 12: Calculated Bond Lengths for Tetracyanonickelate Adsorbed to Anatase

$Ni(CN)_4^{2-}$ Geometry	Bond Formation (Adsorbate - Surface)	Bond Length(s), Å	Binding Energy, eV (Positive is better)
A	N – Ti	2.06	-3.61
B	N – Ti	2.07	-3.59
C	N - Ti & N – Ti	2.14 & 2.14	-2.21
D	N - Ti & N – Ti	2.14 & 2.14	-2.23
E (Optimal)	N - Ti & N – Ti	2.15 & 2.15	-2.21
F	N - Ti & N – Ti	2.30 & 2.30	-4.02

Figure 43 shows the calculated density of states for the selected optimal geometry. Tetracyanonickelate adds significantly to the states provided by anatase, with states ranging from -7 eV to -0.5 eV, the HOMO of tetracyanonickelate. The LUMO of tetracyanonickelate is located around 3 eV. The HOMO band of titanium dioxide is at -2 eV, with its LUMO band at 0.5 eV; this

retains the previously-calculated TiO_2 band gap of 2.5 eV. Light may excite electrons from the HOMO of $Ni(CN)_4^{2-}$ to its LUMO, requiring light of high energy (~3.5 eV), or simply to the LUMO of TiO_2, which only requires 1.03 eV. This direct photosensitization is likely to allow visible light to excite electrons, indicating that tetracyanonickelate has vast potential as a photosensitizer if anchored to the anatase surface. Further research is needed to determine whether $Ni(CN)_4^{2-}$ can bond effectively to TiO_2; however, the ability of $Fe(CN)_6^{4-}$ to bond to the surface is promising (48).

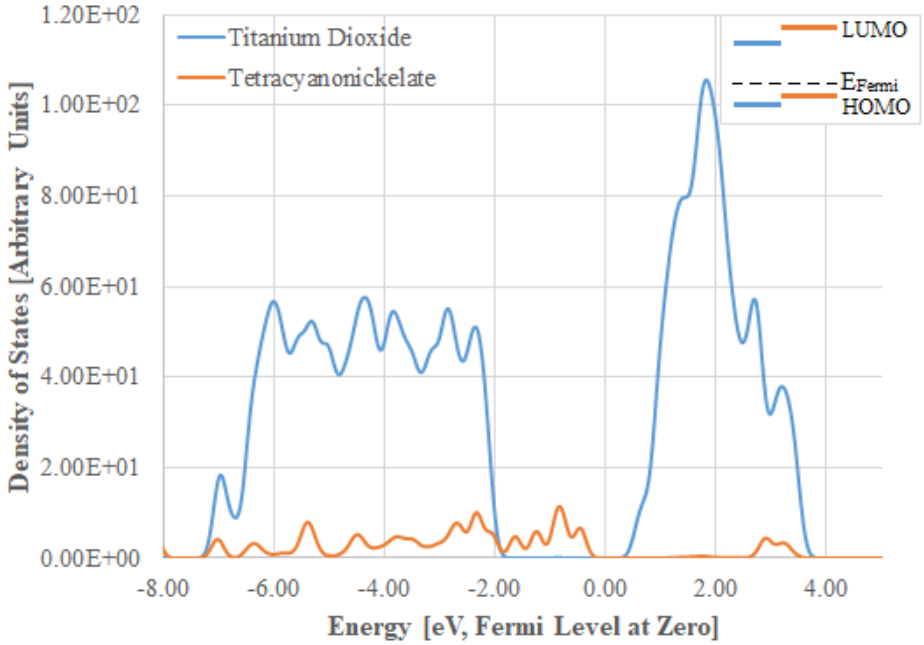

Figure 43: Calculated density of states for tetracyanonickelate adsorbed to the titanium dioxide surface. Electronic contributions from titanium dioxide are shown in blue, while contributions from tetracyanonickelate are shown in orange.

3.4.7 Tetracyanopalladate

We examined the effect of changing metals from nickel to palladium by simulating tetracyanopalladate. Figure 44 shows the most stable configuration of $Pd(CN)_4^{3-}$ over TiO_2. To ensure consistency in the same way that we did with $Ni(CN)_4^{2-}$, the $Pd(CN)_4^{3-}$-TiO_2 system was modeled with a charge of -3. The most stable geometry of $Pd(CN)_4^{3-}$ is nearly identical to that of $Ni(CN)_4^{2-}$; two nitrogen atoms bonded to two raised titanium atoms on the surface. These bond lengths are 2.2 Å, only slightly longer than those in $Ni(CN)_4^{2-}$-TiO_2. As with $Ni(CN)_4^{2-}$, VASP could not accurately predict the energy due to the system charge (8); the program generated a binding energy of -3.21. Increasing the box size or adding charged corrections may help obtain better binding energies. As in $Ni(CN)_4^{2-}$, ionic interactions should cause $Pd(CN)_4^{3-}$ to bind strongly to the surface of titanium dioxide, although this needs to be further explored.

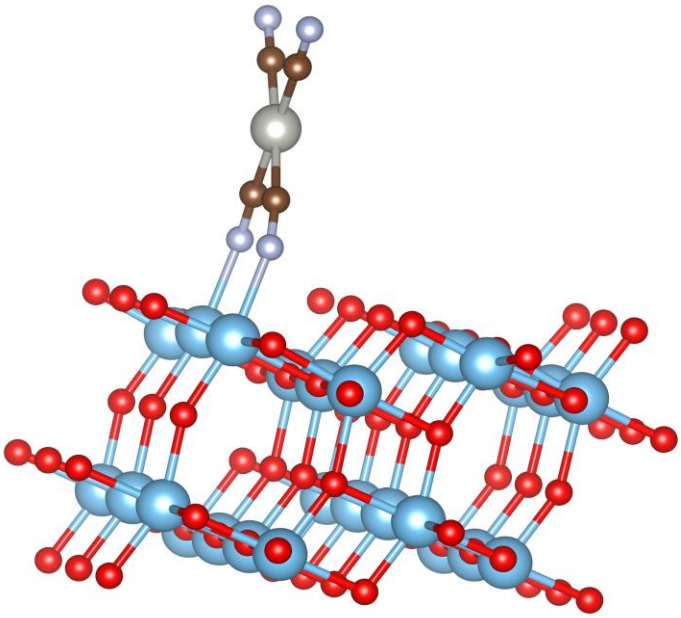

Figure 44: Geometry C, tetracyanopalladate's most stable bonding geometry with titanium dioxide.

Figure 45 shows the other converged geometries for $Pd(CN)_4^{3-}$. Two of these have monodentate geometry and three have bidentate geometry, and their bond lengths and distorted binding energies are shown in Table 13. Geometries A and B converged similarly to $Ni(CN)_4^{2-}$; a single nitrogen atom interacted with a raised titanium atom at a distance of ~2.14 Å and energy of ~-4 eV. Geometries C, D, and E are also similar; two nitrogen atoms bond with raised titanium atoms at distances of ~2.2 Å and energies of ~-3.21 eV. The final geometry, geometry F, is the same kind of outlier as in $Ni(CN)_4^{2-}$, with distorted square planar geometry so two opposing nitrogen atoms can bond to titanium atoms on the surface. This geometry has bond distances of 2.37 Å and energy of -5.47 eV and is therefore unlikely to be the strongest bond of the set. These geometries parallel $Ni(CN)_4^{2-}$ strongly, heavily indicating that energy is distorted predictably by VASP, and reinforcing the idea that the most stable bond retains the highest binding energy, despite the distortion imposed by the program. Furthermore, the palladium atom never bonded to the surface itself, indicating that the N-Ti bonds are far stronger than metal-oxygen or metal-titanium bonds.

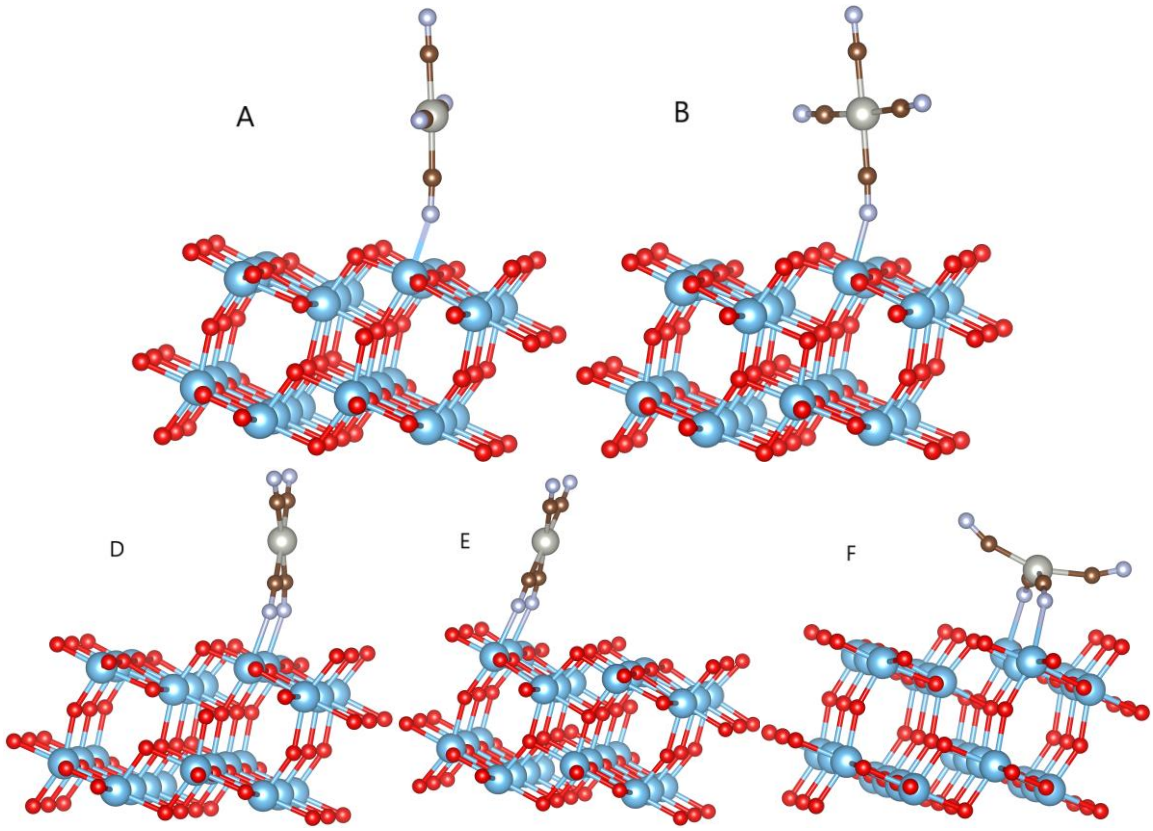

Figure 45: Converged adsorption geometries studied for tetracyanopalladate. Each geometry is labeled as it appears in Table 13.

Table 13: Calculated Bond Lengths for Tetracyanopalladate Adsorbed to Anatase

$Pd(CN)_4^{3-}$ Geometry	Bond Formation (Adsorbate - Surface)	Bond Length(s), Å	Binding Energy, eV (Positive is better)
A	N - Ti	2.14	-4.15
B	N - Ti	2.15	-3.88
C (Optimal)	N - Ti & N - Ti	2.2 & 2.2	-3.21
D	N - Ti & N - Ti	2.2 & 2.2	-3.22
E	N - Ti & N - Ti	2.21 & 2.21	-3.22
F	N - Ti & N – Ti	2.37 & 2.37	-5.47

Figure 46 shows the calculated density of states for the selected optimal geometry. Due to problems with incorrect orbitals, the density of states for $Pd(CN)_4^{3-}$ was calculated using the tetrahedron method. Tetracyanopalladate adds a range of states from -5 to -2.5 eV, with its HOMO

at -0.01 eV and its LUMO at 2.5 eV. Light may excite electrons from the HOMO of $Pd(CN)_4^{3-}$ to its LUMO, with a band gap of 2.5 eV; alternatively, they can be excited from the HOMO of $Pd(CN)_4^{3-}$ to the LUMO of TiO_2, with a band gap of 0.50 eV. This direct photosensitization has an excellent potential to excite electrons, indicating that tetracyanopalladate has strong potential as a photosensitizer if it bonds well with the anatase surface. Further research is needed to determine whether $Pd(CN)_4^{3-}$ can bond effectively to TiO_2, although the ability of $Fe(CN)_6^{4-}$ to bond to the surface remains promising (48).

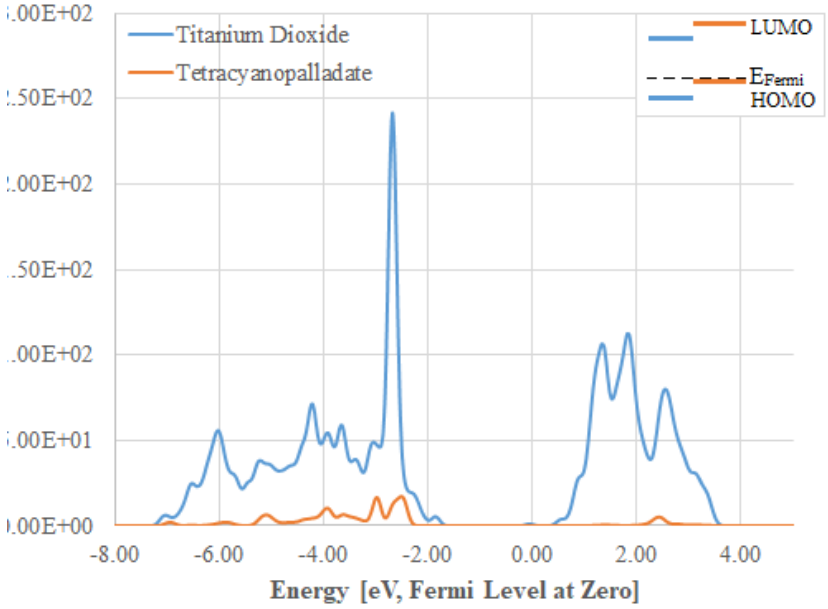

Figure 46: Calculated density of states for hexacyanopalladate adsorbed to the titanium dioxide surface. Electronic contributions from titanium dioxide are shown in blue, while contributions from hexacyanopalladate are shown in orange.

3.4.8 Hexacyanotitanate

In an attempt to examine an octahedral geometry with cyanide ligands, we next considered hexacyanotitanate. Figure 47 shows the most stable configuration of $Ti(CN)_6^{4-}$ over TiO_2. Similar to the previous two molecules, both the $Ti(CN)_6^{4-}$-TiO_2 system and the lone $Ti(CN)_6^{4-}$ molecule were modeled with a -4 charge. Interestingly, this molecule assumed a tridentate bond with the surface; three nitrogen atoms bonded at distances of 2.23, 2.24, and 2.36 Å to raised titanium atoms on the surface. As in tetracyanonickelate and tetracyanopalladate, the actual overall energies were distorted due to the charge on the system. This lead to an inaccurate binding energy of -2.68 eV. Ionic interactions should allow hexacyanotitanate to bond fairly strongly to the titanium dioxide surface. Of note is the structure of this geometry; the octahedral shape is distorted into more of a double cone, and one cyanide ligand is flipped, with the nitrogen bonding to the titanium center instead of the carbon. The Ti - C bonds are also stretched, varying from 2.21 Å for cyanide groups bonding with the slab to 2.10 Å for cyanide groups not bonding with the slab. Furthermore, one of the cyanide ligands became flipped, with the central titanium bonding to nitrogen rather than

carbon. This is uncharacteristic for a cyanide ligand and indicates there may be an issue with the VASP calculation of the structure. The binding of $Ti(CN)_6^{4-}$ to titanium dioxide requires further work to clarify this structure.

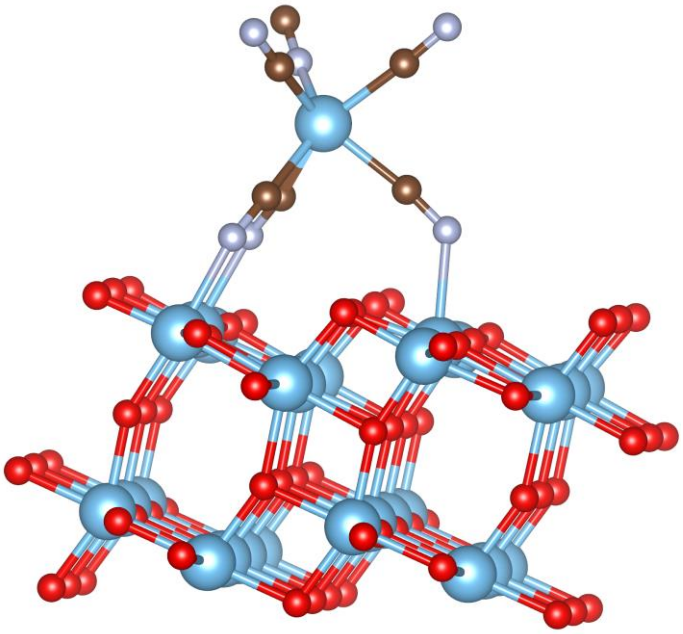

Figure 47: Geometry C, hexacyanotitanate's optimal bonding geometry with titanium dioxide.

Figure 48 shows the other converged geometries for $Ti(CN)_6^{4-}$. One of these is monodentate and four are bidentate, and their bond lengths and binding energies are shown in Table 14. All geometries are unique; even in geometries E and F, where bonding to the surface is similar, the molecule's ligands are in completely different positions. Geometry A involved two nitrogen atoms bonding to raised titanium atoms at a distance of 2.19 Å and a binding energy of -2.96 eV. This geometry also shaped the molecule into a near double-cone as in geometry C. Geometry B involved one nitrogen atom bonding to a raised titanium atom at a distance of 2.11 Å and energy of -4.22 eV. In this geometry, the lowermost Ti-C bond in $Ti(CN)_6^{4-}$ is stretched to 2.21 Å from 2.16 Å, which is small but not insignificant. In geometry D, the molecule again assumes a near double-cone shape so two nitrogen atoms can bond to titanium atoms on distant bridges at lengths of ~2.23 Å and a binding energy of -3.39 eV. In both geometry E and F, one cyanide ligand flips around so carbon binds with the titanium surface and nitrogen with the titanium center of the organometallic. In geometry E, the C-Ti bond has a length of 2.29 Å while the N-Ti bond has a length of 2.17 Å; the binding energy is -3.08 eV. Geometry F seems to place more strain on the molecule, as the C-Ti bond has a length of 2.46 Å while the N-Ti bond has a length of 2.33 Å, and the binding energy is -4.29 eV. The uniqueness of each geometry combined with their notable deformation of the $Ti(CN)_6^{4-}$ molecule in each case indicates that VASP may be encountering a serious issue in attempting to model $Ti(CN)_6^{4-}$ adsorbed to anatase, and this issue should be revisited with a different approach.

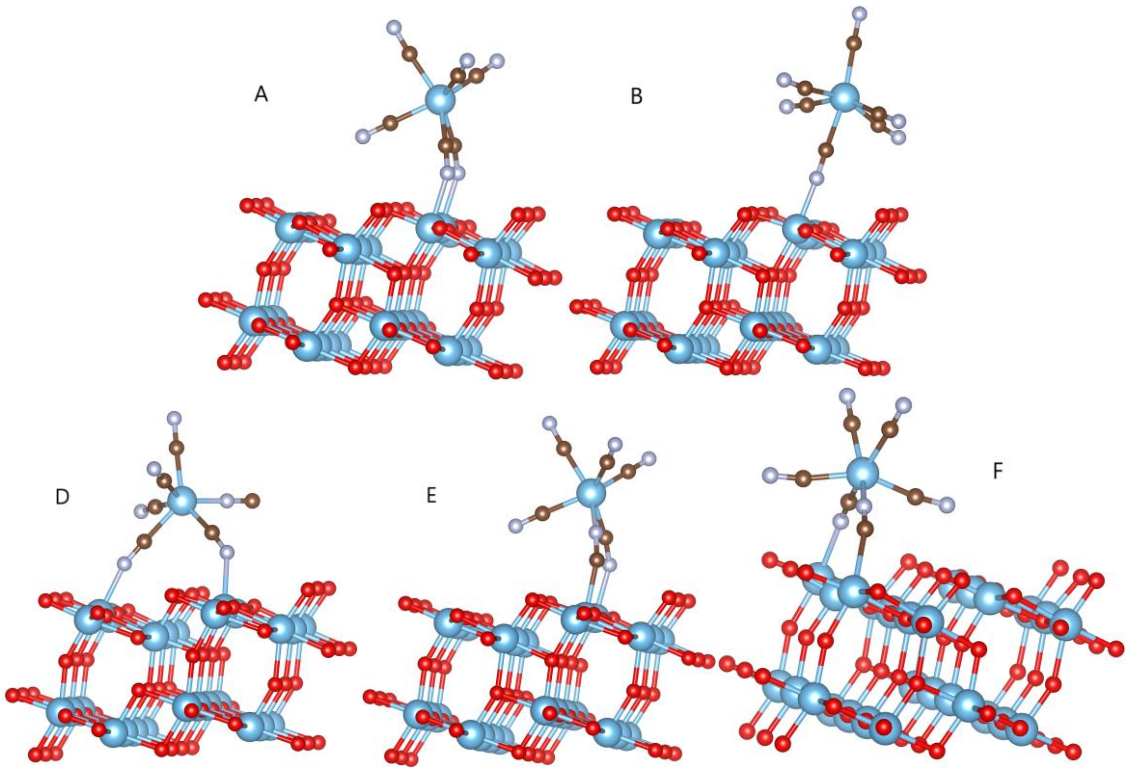

Figure 48: Converged adsorption geometries studied for hexacyanotitanate. Each geometry is labeled as it appears in Table 14.

Table 14: Calculated Bond Lengths for Hexacyanotitanate Adsorbed to Anatase

$Ti(CN)_6^{4-}$ Geometry	Bond Formation (Adsorbate - Surface)	Bond Length(s), Å	Binding Energy, eV (Positive is better)
A	2x N - Ti	2.19 & 2.19	-2.96
B	N - Ti	2.11	-4.22
C (Optimal)	3x N - Ti	2.24 & 2.23 & 2.36	-2.68
D	2x N - Ti	2.25 & 2.2	-3.39
E	C - Ti & N - Ti	2.29 & 2.17	-3.08
F	C - Ti & N – Ti	2.46 & 2.33	-4.29

Figure 49 shows the calculated density of states for the selected optimal geometry. Hexacyanotitanate inserts a range of states at -7 eV, -6 to -5.5 eV, and -5 to -1 eV, with its HOMO at -1 eV. It's LUMO at 1.5 eV and has more states at just above 4 eV and at 6 eV. The HOMO of titanium dioxide remains at -0.5 eV and its LUMO at 2 eV, retaining the band gap of 2.5 eV. Light

may excite electrons from the HOMO of TiO_2 to the LUMO of $Ti(CN)_6^{4-}$, requiring light of 2.07 eV. It may also excite from the HOMO of $Ti(CN)_6^{4-}$ to its LUMO, requiring 2.5 eV. Photosensitization from TiO_2 to $Ti(CN)_6^{4-}$ might allow visible light to excite electrons, but less so than tetracyanonickelate or iron(II) tricarbonyl dibromide. Furthermore, the odd geometry of $Ti(CN)_6^{4-}$ may distort the density of states, giving a poorer estimate of the ability of $Ti(CN)_6^{4-}$ as a photosensitizer. Compared with the simple monodentate binding geometry of $Fe(CN)_6^{4-}$ (44), these geometries seem off, likely affecting the density of states.

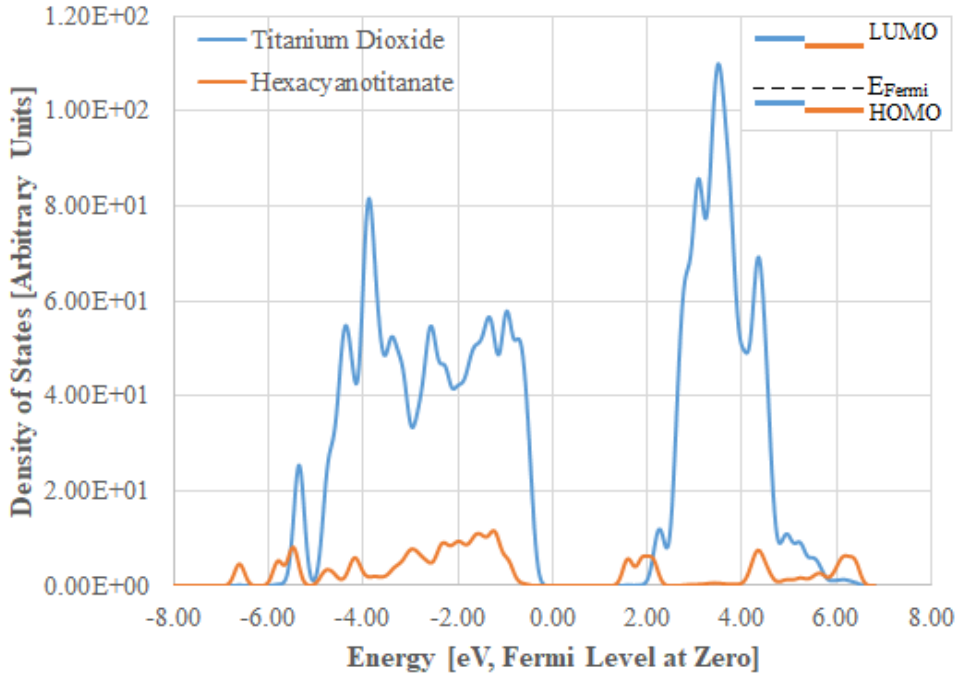

Figure 49: Calculated density of states for hexacyanotitanate adsorbed to the titanium dioxide surface. Electronic contributions from titanium dioxide are shown in blue, while contributions from hexacyanotitanate are shown in orange.

3.4.9 Comparisons Between Molecules

Overall, carbonyl ligands are a poor choice for both adhering to anatase and improving photoexcitation. All molecules with only carbonyl ligands, including chromium hexacarbonyl and iron pentacarbonyl, bonded poorly to the anatase surface with binding energies less than 0.24 eV, making them susceptible to detaching in aqueous solution. These molecules also provided no useful benefits for photoexcitation.

The exchange of carbonyl groups for halide molecules, as in iron(II) tricarbonyl diiodide and iron(II) tricarbonyl dibromide, both made bonding easier and enabled better photosensitization. These molecules could assume an octahedral geometry, allowing the central metal to bond directly to an oxygen atom on the surface; this did not occur in iron pentacarbonyl, indicating that the polar halide molecules facilitated the bonding of the molecule to the surface. The large iodide ligands of iron(II) tricarbonyl diiodide interfered with this bond, however, as bond

energy remained below 0.24 eV similar to carbonyl-titanium bonds. Iron(II) tricarbonyl diiodide did introduce a band gap of 1.5 eV to the anatase system and made photoexcitation more possible. The smaller bromide ligands of iron(II) tricarbonyl dibromide were much more effective, increasing the binding energy to 0.59 eV; however, the molecule only decreased the minimum band gap in the anatase system to 1.85 eV. This trend indicates that substituting chloride ligands, as in iron(II) tricarbonyl dichloride, could further increase the binding energy to the surface, but may also increase the band gap of the system, reducing the photosensitization benefits granted by the other halide ligands.

The exchange of carbonyl groups with cyanide groups, as in $Ni(CO)_4$ to $Ni(CN)_4^{2-}$, seemed to greatly improve photosensitization. The final geometry changed for the two molecules upon adsorption, with the square planar $Ni(CN)_4^{2-}$ bonding in a bidentate fashion to the anatase surface at with CN-Ti distances of 2.15 Å. Compare this bond length to the CO-Ti bond in $Ni(CO)_4$, 2.38 Å. Although no conclusions can be drawn about their relative bond strengths, tetracyanonickelate generated occupied electronic states at much higher energy than the anatase HOMO, reducing the gap between its HOMO and anatase's LUMO to 1.03 eV. On the other hand, nickel tetracarbonyl generated no states between the anatase HOMO and LUMO, so electrons would have to cross the same gap as in normal anatase to become excited.

The exchange of metals between nickel and palladium, as in $Ni(CN)_4^{2-}$ to $Pd(CN)_4^{3-}$, seemed to greatly improve photosensitization. These two similar molecules bonded with nearly identical geometries. $Ni(CN)_4^{2-}$ bonded closer, at distances of 2.15 Å, compared to $Pd(CN)_4^{3-}$ which bonded at distances of 2.20 Å. Although neither binding energy could be determined due to potential errors for charged systems (8), $Pd(CN)_4^{3-}$ provided a much smaller minimum band gap of 0.50 eV for photoexcitation, compared to that in $Ni(CN)_4^{2-}$, which came to 1.03 eV. This is due to $Pd(CN)_4^{3-}$ generating filled states at a much higher energy than $Ni(CN)_4^{2-}$. This result indicates that the choice of metal can have a profound effect on the location of the HOMO in an adsorbed organometallic complex. The ability to choose metal to influence the density of states is potentially very powerful; ligand choice seems to greatly influence both bonding and density of states, so a powerful organometallic photosensitizer can be found by first finding the best ligands for binding and photosensitization, then varying the metal center. The states generated by cyanide above the HOMO of anatase indicate that cyanide is the most promising photosensitizer ligand studied.

Despite the odd geometries encountered in $Ti(CN)_6^{4-}$, it displayed some similarities as an adsorbate to $Ni(CN)_4^{2-}$ and $Pd(CN)_4^{3-}$. Cyanide groups bonded fairly close to the surface of anatase, at around lengths of 2.30 Å, similar to $Ni(CN)_4^{2-}$ at 2.15 Å and $Pd(CN)_4^{3-}$ at 2.20 Å. Rather than creating filled states, however, $Ti(CN)_6^{4-}$ created unfilled states starting around 1.5 eV. This still resulted in a reduction of the minimum band gap to 2.07 eV, although this gap is larger than the minimum band gaps of 1.03 in $Ni(CN)_4^{2-}$-TiO_2 and 0.50 in $Pd(CN)_4^{3-}$-TiO_2. Due to the distorted nature of $Ti(CN)_6^{4-}$-TiO_2 geometries, it is difficult to derive a trend from this comparison; it may further reinforce that cyanide ligands are strong photosensitizing agents. Further research is required to determine whether the differences between these molecules are due to the change of metal, change of charge, or change from square planar to octahedral geometry.

3.4.10 Issues with Incorrect Atomic Orbitals

Aside from requiring more time, some calculations of adsorbed molecules on TiO_2 suffered from the same incorrect orbital structures as the gas-phase molecules; electron orbitals assumed partial occupancy (occupancy between 0 and 1), rather than being fully occupied or unoccupied. These incorrect structures gave inaccurate electronic structures and total energies, preventing us from properly assessing the effectiveness of such a photosensitizer due to both erroneous band gap and binding energy. Calculations of adsorbed molecules such as ferrocyanide, iron(II) tricarbonyl diiodide, and tetracyanonickelate were affected by these incorrect electronic orbitals. Through the same steps as section 3.3.2 above, setting ALGO to Normal and varying AMIX and BMIX parameters, calculations of iron(II) tricarbonyl diiodide were corrected to give correct orbitals. Other calculations did not properly converge and changing these parameters did not help to correct the convergence issues. However, using the tetrahedron method by changing the ISMEAR line in the INCAR file from 0 to -5 and setting the k-point mesh to 4x4x4 allowed some molecule-surface configurations to converge without partial occupancy in the molecular orbitals. This was effective in converging tetracyanonickelate and tetracyanopalladate adsorbed to the surface of titanium dioxide. We were unable to find a literature value for tetracyanopalladate, so it is unknown whether the tetrahedron method was effective in converging molecules with a band gap similar to literature values. Further investigation is needed to determine the usefulness of the tetrahedron method.

4 Conclusions and Future Work

4.1 Conclusions

The goal of this project was to evaluate organometallic compounds and predict their effectiveness as photosensitizers when bonded to a TiO_2 semiconductor surface. Using the Vienna Ab-initio Simulation Package (VASP), density functional theory (DFT) calculations were performed to predict the photocatalytic activity of the chosen organometallic compounds both alone and bonded to titanium dioxide. We were able to accurately model the properties of TiO_2, such as the band gap and electron energies, simulate a number of potential organometallic compounds and ensure our results agreed with literature results, and determine which compounds could be optimal photosensitive materials. This was done using DFT, because we needed to evaluate the density of states that occurred when titanium dioxide was bonded to our chosen organometallic compounds. This information determined how the band gap properties changed when a photosensitizer was present. Since visible light is readily available, photosensitizers which allowed TiO_2 to capture light in that part of the light spectrum were the most significant.

We found that carbonyl ligands are a poor choice for both adhering to anatase and improving photoexcitation. All molecules with only carbonyl ligands bonded poorly to the anatase surface with binding energies less than 0.24 eV, making them susceptible to detaching in aqueous solutions. The exchange of carbonyl groups with cyanide groups, as in $Ni(CO)_4$ to $Ni(CN)_4^{2-}$, seemed to greatly improve photosensitization. No conclusions were able to be drawn about their relative bond strengths due to error in the binding energy of $Ni(CN)_4^{2-}$ inherent with the charged system. Tetracyanonickelate generated occupied electronic states at much higher energy than the anatase's HOMO, reducing the gap between tetracyanonickelate's HOMO and the anatase's LUMO to 1.03 eV. On the other hand, nickel tetracarbonyl generated no states between the anatase's HOMO and LUMO, so electrons would have to cross the same gap as in normal anatase to become excited. The states generated using cyanide ligands above the HOMO of anatase indicate that cyanide is a very promising photosensitizer that was studied.

Exchanging carbonyl groups for halide molecules made bonding to the anatase surface stronger, because these molecules could assume an octahedral geometry, which allowed the central metal to bond directly to an oxygen atom on the surface. However, the large iodide ligands in iron(II) tricarbonyl diiodide did interfere with the surface binding, causing the overall binding energy to be 0.24 eV. Iron(II) tricarbonyl dibromide was a promising photosensitizer, because the smaller bromide ligands increased the binding energy to 0.59 eV as well as decreasing the minimum band gap in the anatase system to 1.85 eV. This trend indicates that substituting chloride ligands, as in iron(II) tricarbonyl dichloride, could further increase the binding energy to the surface.

During the course of our work, we discovered that some calculations had electronic orbitals that failed to be fully occupied or unoccupied, but rather were partially occupied. Calculations with incorrect orbitals would therefore have inaccurate total energy and electronic states for these types of calculations. Through several changes to the INCAR files, and eventually the use of the

tetrahedron method, we were able to amend some of the calculations affected by incorrect electronic orbitals.

4.2 Future Work

Through our simulations of organometallic compounds binding to an anatase surface, we obtained valuable insight into how organometallic compounds can lower the band gap in a TiO_2 semiconductor. We recommend the following as future work related to this project.

1. Performing more simulations with compounds with cyanide and halide ligands.

These showed the most promise for allowing visible light to be able to excite electrons into the conduction band. For example, iron(II) tricarbonyl dichloride or difluoride may increase the binding energy and lower the minimum band gap more than iron (II) tricarbonyl dibromide did.

2. Using different metals attached to a cyanide compounds and other ligands.

Metals such as iron, as in ferrocyanide, may change the geometry of the molecule allowing it to bind better to the surface and create desired energy states in between the HOMO and LUMO of the anatase.

3. Determine methods to overcome the incorrect orbital problems in organometallic compounds.

Incorrect orbitals caused numerous issues, and we attempted to correct them by changing the calculation settings or using the tetrahedron method. Calculations should be run to determine the accuracy of the tetrahedron method versus our default smearing method, Gaussian smearing, and test other methods to overcome incorrect orbitals.

4. Perform physical experiments to verify the accuracy of our simulations.

Depending on the results from these experiments other organometallic compounds could then be modeled first using computer simulations, and then synthesized and tested in the laboratory.

Acknowledgements

We would like to thank the following people for their support in this endeavor:

Our advisor, Professor N. Aaron Deskins, for his support and guidance.

Satish Siyemperumal, a graduate student working under Professor Deskins, for his help learning the VASP program and insights into both running it and extracting data.

WPI's department of chemical engineering, for the use of the high-performance computer (HPC) clusters for the processors to run simulations in VASP.

Spencer Pruitt, a Computational Scientist at WPI, for his tireless work ensuring our multitude of calculations came to completion.

References

1. *Key World Energy Statistics 2017.* (2017). Paris: OECD Publishing; International Energy Agency.

2. *How Much Electricity Does an American Home Use? - FAQ*. (2016). Retrieved from https://www.eia.gov/tools/faqs/faq.php?id=97&t=3.

3. Peter, L., Hakki, A., Mendive, C., Paz, Y., Choi, W., Schneider, J., Schneider, J., Bahnemann, D.Y., Jinhua P., Gianluca L.D., Dionysios D.. (2016). Photocatalysis - Fundamentals and Perspectives. *Royal Society of Chemistry*.

4. Jin, T., Liu, C., & Li, G. (2014). Photocatalytic CO2 Reduction Using a Molecular Cobalt Complex Deposited on TiO2 Nanoparticles. *Chemical Communications (Cambridge, England)*, *50*(47), 6221–4.

5. Burdett, J. K., Hughbanks, T., Miller, G. J., Richardson Jr, J. W., & Smith, J. V. (1987). Structural-electronic relationships in inorganic solids: powder neutron diffraction studies of the rutile and anatase polymorphs of titanium dioxide at 15 and 295 K. *Journal of the American Chemical Society*, *109*(12), 3639-3646.

6. Pacchioni, G. (2008). Modeling doped and defective oxides in catalysis with density functional theory methods: Room for improvements. *The Journal of chemical physics*, *128*(18), 182505.

7. Lazzeri, M., Vittadini, A., & Selloni, A. (2001). Structure and Energetics of Stoichiometric TiO_2 Anatase Surfaces. *Physical Review B*, *63*(15), 155409.

8. Kresse, G., & Furthmüller, J. (1999, March 29). *Monopole, Dipole and Quadrupole corrections: NELECT, IDIPOL, DIPOL, LMONO, LDIPOL, EPSILON and EFIELD*. Retrieved March 13, 2018, from http://cms.mpi.univie.ac.at/vasp/vasp/Monopole_Dipole_Quadrupole_corrections_NELECT_IDIPOL_DIPOL_LMONO_LDIPOL_EPSILON.html.

9. Vallero, D. (2014). *Fundamentals of Air Pollution* (5th ed.) Elsevier.

10. *Global Trends in Renewable Energy Investment 2017.* (2017). Frankfurt: Frankfurt School-UNEP Centre/BNEF.

11. *Climate and Earth's Energy Budget: Feature Articles*. (n.d.). Retrieved October 08, 2017, from https://earthobservatory.nasa.gov/Features/EnergyBalance/page2.php.

12. Walker, A. (2013). *Solar Energy: Technologies and Project Delivery for Buildings* (1st ed.). Somerset: Wiley.

13. Honorio, L. et al. (2003). *Efficiency in Electricity Generation* (1). Brussels, Belgium.

14. Energy Sage. (2017, September 13). *2017 Most Efficient Solar Panels on the Market.* Retrieved from http://news.energysage.com/what-are-the-most-efficient-solar-panels-on-the-market/.

15. Philibert, C. (2005). The Present and Future Use of Solar Thermal Energy as a Primary Source of Energy. *International Energy Agency,* Paris, France.

16. Armaroli, Nicola & Balzani, Vincenzo. (2007). The Future of Energy Supply: Challenges and Opportunities. *Angewandte Chemie (International ed. in English)*. 46. 52-66.

17. McNaught, A. D., & Wilkinson, A. (2005). *IUPAC Compendium of Chemical Terminology (gold book)* (2nd ed.). Oxford: Blackwell Scientific Publications.

18. Reprinted from Wikipedia. (2017, December 6). *Catalysis.* Retrieved January 3, 2018, from https://en.wikipedia.org/wiki/Catalysis.

19. Kim, W., Mcclure, B. A., Edri, E., & Frei, H. (2016). Coupling Carbon Dioxide Reduction with Water Oxidation in Nanoscale Photocatalytic Assemblies *Chem. Soc. Rev*, *45*(45), 3221–3243.

20. Hehre, W. J. (2003). *A Guide to Molecular Mechanics and Quantum Chemical Calculations* (Vol. 2). Irvine, CA: Wavefunction.

21. Babu, V. S. (2010). *Solid State Devices and Technology, 3rd Edition*. Pearson.

22. Reprinted from Wikipedia. (2018, January 1). *Semiconductors.* Retrieved January 3, 2018, from https://en.wikipedia.org/wiki/Semiconductor.

23. Crabtree, R. H. (2014). *The Organometallic Chemistry of the Transition Metals* (6th ed.). US: John Wiley & Sons Ltd.

24. Reprinted from The Prashant Kamat Laboratory. Kamat, P. (2016). *Photocatalysis.* Retrieved January 03, 2018, from https://www3.nd.edu/~kamatlab/research_photocatalysis.html.

25. Yin, Y., Liang, J., Yang, L.,& Wang, Q. (2007). Vapour Generation at a UV/TiO2 Photocatalysis Reaction Device for Determination and Speciation of Mercury by AFS and HPLC-AFS. *Journal of Analytical Atomic Spectrometry, 22,* 330-334.

26. Liu, Y., Jia, X., & Wu, X. (2014). ZnO Core-Shell Microspheres Prepared by One-Pot Hydrothermal Reaction and their Photocatalysis Properties. *Micro & Nano Letters, 9*(5), 328-331.

27. Khan, M. M., Adil, S. F., & Al-Mayouf, A. (2015). Metal oxides as photocatalysts. *Journal of Saudi Chemical Society, 19*(5), 462-464.

28. Moussa, H., Girot, E., Mozet, K., Alem, H., Medjahdi, G., & Schneider, R. (2016). ZnO Rods/Reduced Graphene Oxide Composites Prepared via a Solvothermal Reaction for Efficient Sunlight-driven Photocatalysis. *Applied Catalysis B: Environmental, 185*, 11-21.

29. Lin, W., & Frei, H. (2006). Bimetallic Redox Sites for Photochemical CO2 Splitting in Mesoporous Silicate Sieve. *Comptes Rendus Chimie, 9*(2), 207–213.

30. Frei, H. (2009). Polynuclear Photocatalysts in Nanoporous Silica for Artificial Photosynthesis. *CHIMIA International Journal for Chemistry, 63*(11), 721–730.

31. Alenezi, K. (2015). Solar Light-driven Reduction of CO2 on P-type Silicon Semiconducting Electrodes by Iron(0)pentaflourotetraphenylporphyrin. *International Journal of Electrochemical Science, 10,* 4279-4289.

32. He, D., Jin, T., Li, W., Pantovich, S., Wang, D., & Li, G. (2016). Photoelectrochemical CO2 Reduction by a Molecular Cobalt(II) Catalyst on Planar and Nanostructured Si Surfaces. *Chemistry – A European Journal, 22*(37), 13064-13067.

33. Agarwal, J., Johnson, R. P., & Li, G. (2011). Reduction of CO2 on a Tricarbonyl Rhenium (I) Complex: Modeling a Catalytic Cycle. *J. Phys. Chem. A., 115*(I), 2877–2881.

34. Huang, J., Du, X., Feng, Y., Zhao, Y., & Ding, Y. (2016). New Insights into Water Oxidation Reactions from Photocatalysis, Electrocatalysis to Chemical Catalysis: An Example of Iron-based Oxides Doped with Foreign Elements. *Physical Chemistry Chemical Physics: PCCP, 18*(15), 9918-9921.

35. Ollis, D. F., Pelizzetti, E., & Serpone, N. (1991). Photocatalyzed Destruction of Water Contaminants. *Environmental Science and Technology, 25*(9), 1522-1529.

36. Apte, S. K., Garaje, S. N., Naik, S. D., Waichal, R. P., Baeg, J., & Kale, B. B. (2014). Quantum Confinement Controlled Solar Hydrogen Production from Hydrogen Sulfide Using a Highly Stable CdS0.5Se0.5/CdSe Quantum Dot-Glass Nanosystem. *Nanoscale, 6*, 908-915.

37. Reprinted from Science Questions with Surprising Answers. Baird, C. S. (2013, July 3). *What is the color of the sun?* Retrieved January 3, 2018, from http://wtamu.edu/~cbaird/sq/2013/07/03/what-is-the-color-of-the-sun/.

38. Oleinick , N. L. (2011, June 9). *Basic Photosensitization*. Retrieved November 27, 2017, from http://photobiology.info/Oleinick.html.

39. Wikipedia. (2016, July 10). *Photosensitizer*. Retrieved November 27, 2017, from https://en.wikipedia.org/wiki/Photosensitizer.

40. Sahara, Go, Kumagai, Hiromu, Maeda, Kazuhiko, Kaeffer, Nicolas, Artero, Vincent, Higashi, Masanobu, Abe, Ryu, and Ishitani, Osamu. (2016). Photoelectrochemical Reduction of CO2 Coupled to Water Oxidation Using a Photocathode with a Ru(II)−Re(I) Complex Photocatalyst and a CoOx/TaON Photoanode. *Journal of the American Chemical Society.*

41. Louis, M. E., Fenton, T. G., Rondeau, J., Jin, T., & Li, G. (2016). Solar CO2 Reduction Using Surface-Immobilized Molecular Catalysts. *Comments on Inorganic Chemistry, 36*(1), 38-60.

42. Kumar, I. (2007). *Organometallic Compounds* (1st ed.). Meerut: Pragati Prakashan.

43. Wikipedia. (2017, August 29). *Organometallic Chemistry*. Retrieved October 09, 2017, from https://en.wikipedia.org/wiki/Organometallic_chemistry#Concepts_and_techniques.

44. Adapted from Wikipedia. (2017, November 18). *Potassium Ferrocyanide.* Retrieved January 3, 2018, from https://en.wikipedia.org/wiki/Potassium_ferrocyanide.

45. Macyk, W., Szaciłowski, K., Stochel, G., Buchalska, M., Kuncewicz, J., & Łabuz, P. (2010). Titanium(IV) complexes as direct TiO2 photosensitizers. *Coordination Chemistry Reviews*, *254*(21–22), 2687–2701.

46. Wikipedia. (2017, November 18). *Ferrocyanide*. Retrieved December 15, 2017, from https://en.wikipedia.org/wiki/Ferrocyanide.

47. De Angelis, F., Tilocca, A., & Selloni, A. (2004). Time-dependent DFT study of [Fe (CN) 6] 4-sensitization of TiO2 nanoparticles. *Journal of the American Chemical Society, 126*(46), 15024-15025.

48. Etcheberry, A., Simon, N., & Gérard, I. (2007). The Role of the Surface Chemistry on the Evolution of Kinetic of Hole Injection by $Fe(CN)_6^{3-}$ at n- InP. *ECS Transactions, 6* (2), 469-474.

49. Wikipedia. (2017, November 12). *Ferricyanide*. Retrieved December 15, 2017, from https://en.wikipedia.org/wiki/Ferricyanide.

50. Wikipedia. (2016, November 17). *Schrödinger Equation*. Retrieved November 24, 2017, from https://en.wikipedia.org/wiki/Schr%C3%B6dinger_equation.

51. Erbil, H. H. (n.d.). Part 1: A Simple Solution of the Time-Independent Schrödinger Equation in One Dimension. *Ege University, Science Faculty, Physics Department* Bornova - ZMIR 35100, Turkey.

52. Wikipedia. (2015, October 26). *Density Functional Theory*. Retrieved November 24, 2017, from https://en.wikipedia.org/wiki/Density_functional_theory.

53. *Density Functional Theory for Beginners.* (n.d.). Retrieved November 24, 2017, from http://newton.ex.ac.uk/research/qsystems/people/coomer/dft_intro.html.

54. Hohenberg, P., & Kohn, W. (1964). Inhomogeneous Electron Gas. *Physical Review, 136*(3B), B864–B871.

55. Clark, S. J. (2003, May 4). *The Hohenberg-Kohn Theorems*. Retrieved November 29, 2017, from http://cmt.dur.ac.uk/sjc/thesis_ppr/node12.html.

56. Kohn, W., & Sham, L. J. (1965). Self-Consistent Equations Including Exchange and Correlation Effects. *Physical Review, 140*(4A), A1133–A1138.

57. Goedecker, S., Teter, M., & Hutter, J. (1996). Separable dual-space Gaussian pseudopotentials. *Physical Review B, 54*(3), 1703–1710.

58. Blöchl, P. E. (1994). Projector augmented-wave method. *Physical review B, 50*(24), 17953.

59. Perdew, J. P., Chevary, J. A., Vosko, S. H., Jackson, K. A., Pederson, M. R., Singh, D. J., & Fiolhais, C. (1992). Atoms, molecules, solids, and surfaces: Applications of the generalized gradient approximation for exchange and correlation. *Physical Review B*, 46(11), 6671–6687.

60. Sholl, D., Steckel, J. A., & Sholl (2009). *Density Functional Theory: A Practical Introduction*. Hoboken: Wiley.

61. Monkhorst, H. J., & Pack, J. D. (1976). Special points for Brillouin-zone integrations. *Physical review B*, *13*(12), 5188.

62. Makov, G., & Payne, M. C. (1995). Periodic boundary conditions in ab initio calculations. *Physical Review B*, *51*(7), 4014.

63. VASP. (2009). *About VASP*. Retrieved November 24, 2017, from https://www.vasp.at/index.php/about-vasp/59-about-vasp.

64. ASE. (2017). *Atomic Simulation Environment*. Retrieved December 04, 2017, from https://wiki.fysik.dtu.dk/ase/.

65. VESTA. (2013) *Documentation.* Retrieved December 13, 2017, from http://jp-minerals.org/vesta/en/doc.html.

66. Avogadro. (2012) *Avogadro API Documentation.* Retrieved December 13, 2017, from http://avogadro.cc/api/dev/.

67. Desilvestro, J., Pons, S., Vrachnou, E., & Grätzel, M. (1988). Electrochemical and FTIR Spectroscopic Characterization of Ferrocyanide-modified TiO2 Electrodes Designed for Efficient Photosensitization. *Journal of Electroanalytical Chemistry and Interfacial Electrochemistry*, *246*(2), 411-422.

68. Iyemperumal, S. K., & Deskins, N. A. (2017). Activation of CO2 by Supported Cu Clusters. *Physical Chemistry Chemical Physics*, *19*(42), 28788-28807.

69. Garcia, J. C., & Deskins, N. A. (2012). Detailing Ionosorption over TiO2, ZrO2, and HfO2 from First Principles. *The Journal of Physical Chemistry C*, *116*(31), 16573-16581.

70. Park, J. Y., Lee, C. H., Jung, K. W., & Jung, D. W. (2009). Structure related photocatalytic properties of TiO 2. *Bulletin of the Korean Chemical Society*, *30*(2), 402-404.

71. Park, S. K., Lee, C. K., Lee, S. H., & Lee, N. S. (2002). Vibrational analysis of ferrocyanide complex ion based on density functional force field. *Bulletin of the Korean Chemical Society*, *23*(2), 253-261.

72. Ishiruji, F. H., Speziali, N. L., Vaz, M. G., & Nunes, F. S. (2010). Synthesis, crystal structure and properties of the cyano-bridged heteropolynuclear [Cu (meso)] 3 [Co (CN) 6] 2• 9.5 H2O compound. *Journal of the Brazilian Chemical Society*, *21*(7), 1195-1200.

73. Kareis, C. M., Lapidus, S. H., Her, J. H., Stephens, P. W., & Miller, J. S. (2012). Non-Prussian blue structures and magnetic ordering of Na2MnII [MnII (CN) 6] and Na2MnII [MnII (CN) 6]· 2H2O. *Journal of the American Chemical Society*, *134*(4), 2246-2254.

74. Albores, P., Slep, L. D., Baraldo, L. M., Baggio, R., Garland, M. T., & Rentschler, E. (2006). Crystal structure and electronic and magnetic properties of hexacyanoosmiate (III). *Inorganic chemistry*, *45*(6), 2361-2363.

75. He, P. (2013). *On the structure-property correlation and the evolution of Nanofeatures in 12-13.5% Cr oxide dispersion strengthened ferritic steels* (Vol. 31). KIT Scientific Publishing.

76. Machado, F. B., & Davidson, E. R. (1993). Binding energy of chromium hexacarbonyl. 2. Revisited with correlation effects. *The Journal of Physical Chemistry*, *97*(17), 4397-4403.

77. McClelland, B. W., Robiette, A. G., Hedberg, L., & Hedberg, K. (2001). Iron Pentacarbonyl: Are the Axial or the Equatorial Iron− Carbon Bonds Longer in the Gaseous Molecule?. *Inorganic chemistry*, *40*(6), 1358-1362.

78. Scapens, D., Adams, H., Johnson, T. R., Mann, B. E., Sawle, P., Aqil, R., ... & Motterlini, R. (2007). [(η-C 5 H 4 R) Fe (CO) 2 X], X= Cl, Br, I, NO 3, CO 2 Me and [(η-C 5 H 4 R) Fe (CO) 3]+, R=(CH 2) n CO 2 Me (n= 0–2), and CO 2 CH 2 CH 2 OH: a new group of CO-releasing molecules. *Dalton Transactions*, (43), 4962-4973.

79. Stock, A., Azran, O., Garden, B., Solaimanzadeh, J., Lo, W., & Jiang, J. (2012). Synthesis of fac-[Fe II (CN)(CO) 3 I 2]− and chemistry of the fac-[Fe II (CN) x (CO) 3 I (3− x)]− series (x= 1–3). *Inorganic Chemistry Communications*, *18*, 105-109.

80. Ladell, J. O. S. H. U. A., Post, B., & Fankuchen, I. (1952). The crystal structure of nickel carbonyl, Ni (CO) 4. *Acta Crystallographica*, *5*(6), 795-800.

81. Li, J., Noll, B. C., Schulz, C. E., & Scheidt, W. R. (2009). Comparison of Cyanide and Carbon Monoxide as Ligands in Iron (II) Porphyrinates. *Angewandte Chemie International Edition*, *48*(27), 5010-5013.

82. Van der Westhuizen, H. J., Basson, S. S., Leipoldt, J. G., & Purcell, W. (1994). The crystal structure of (AsPh 4) 2 [OsN (OH)(CN) 4]. *Transition Metal Chemistry*, *19*(6), 582-584.

83. Bruce, M. I., Rodgers, J. R., Snow, M. R., & Swincer, A. G. (1981). Cyclopentadienyl-ruthenium and-osmium chemistry. Cleavage of tetracyanoethylene under mild conditions: X-ray crystal structures of [Ru {η 3-C (CN) 2 CPhC [double bond, length as m-dash] C (CN) 2}(PPh 3)(η-C 5 H 5)] and [Ru {C [[double bond, length as m-dash] C (CN) 2] CPh [double bond, length as m-dash] C (CN) 2}-(CNBu t)(PPh 3)(η-C 5 H 5)]. *Journal of the Chemical Society, Chemical Communications*, (6), 271-272.

84. Rüegg, M., & Ludi, A. (1971). The structure and spectra of bis (ethylenediamine) nickel (II)-tetracyanopalladate (II), Ni (NH 2 CH 2 CH 2 NH 2) 2 Pd (CN) 4. *Theoretica chimica acta*, *20*(2), 193-202.

85. Kim, Y. J., Joo, Y. S., Han, J. T., Han, W. S., & Lee, S. W. (2002). Synthesis, structures and properties of bis (carbodiimido) complexes of Ni (II), Pd (II) and Pt (II). *Journal of the Chemical Society, Dalton Transactions*, (18), 3611-3618.

86. Schreckenbach, G. (1999). The 57 Fe nuclear magnetic resonance shielding in ferrocene revisited. A density-functional study of orbital energies, shielding mechanisms, and the influence of the exchange-correlation functional. *The Journal of chemical physics*, *110*(24), 11936-11949.

87. Kresse, G., & Furthmüller, J. (1999, March 29). *7.40 Mixing-tags.* Retrieved March 07, 2018, from http://cms.mpi.univie.ac.at/vasp/guide/node131.html#SECTION00094000000000000000.

88. *Chemical Bonds*. (2016, March 6). Retrieved March 7, 2018, from http://lamp.tu-graz.ac.at/~hadley/ss1/crystalbinding/bonds/bonds.php.

Appendices

Appendix A: Anatase (1 0 1) Surface Energy Calculation

Anatase slab total energy (24 Ti atoms, 48 O atoms) = E_{slab} = -640.22383584 eV
Anastase slab area = A = 10.4138549523149475 Å * 11.3997722454724268 Å = 118.715575 Å
Bulk TiO_2 total energy (4 Ti atoms, 8 O atoms) = E_{bulk} = -107.63772385 eV
Slab-to-bulk ratio = n = 24 Ti atoms/4 Ti atoms = 6

Surface energy = $E_{surf} = E_{slab} - n * E_{bulk} / (2 * A)$

E_{surf} = (-640.22383584 - 6*-107.63772385)/(2*118.715575) = 0.0235963447 eV/$Å^2$

E_{surf} = 0.0235963447 eV/$Å^2$ * 1.60218e-19 J/eV * 10^{10}Å/m * 10^{10} Å/m = 0.37805591551446 J/m^2

Appendix B: Molecules Tested

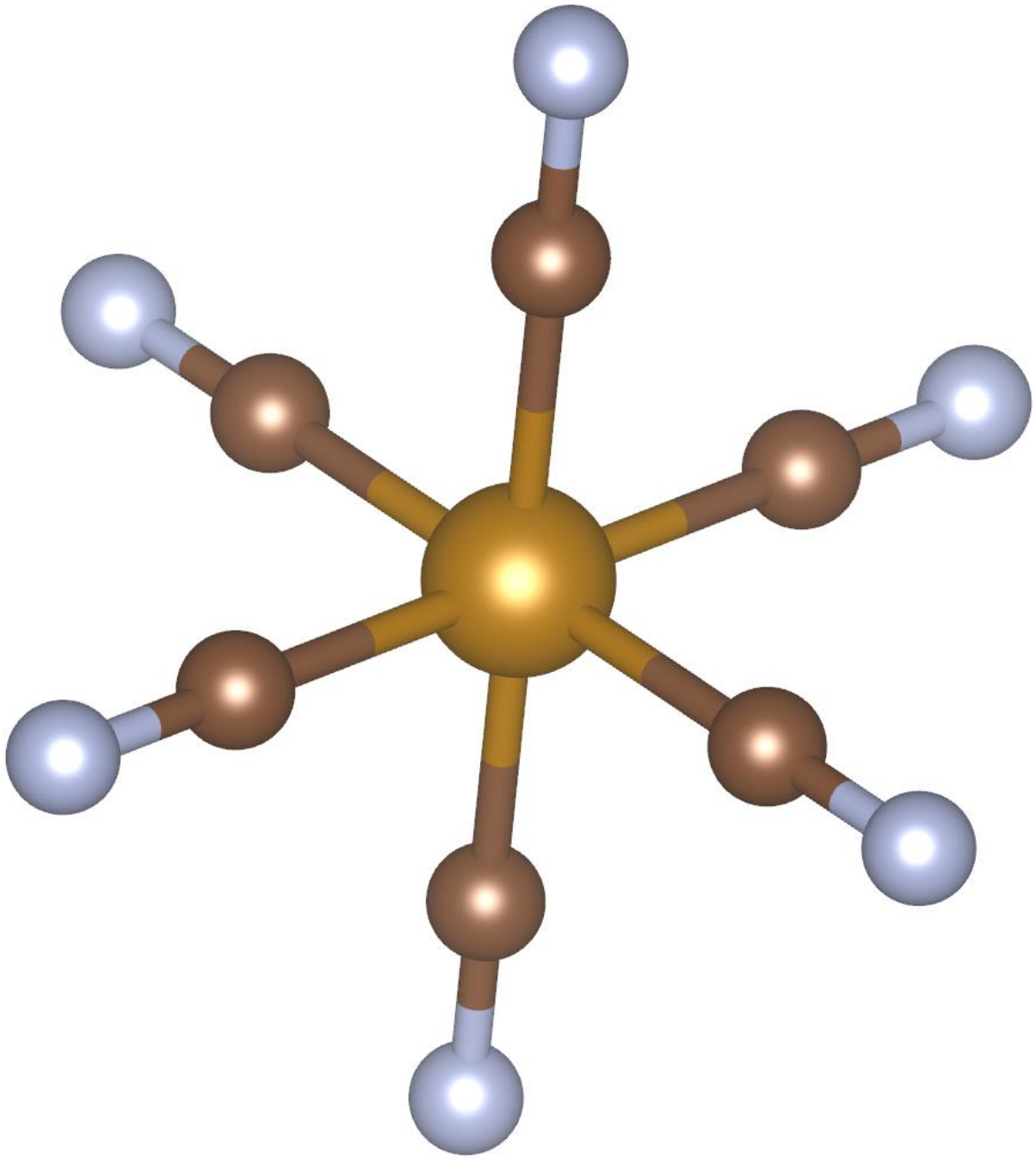

Figure B1:$Fe(CN)_6^{4-}$, Ferrocyanide.

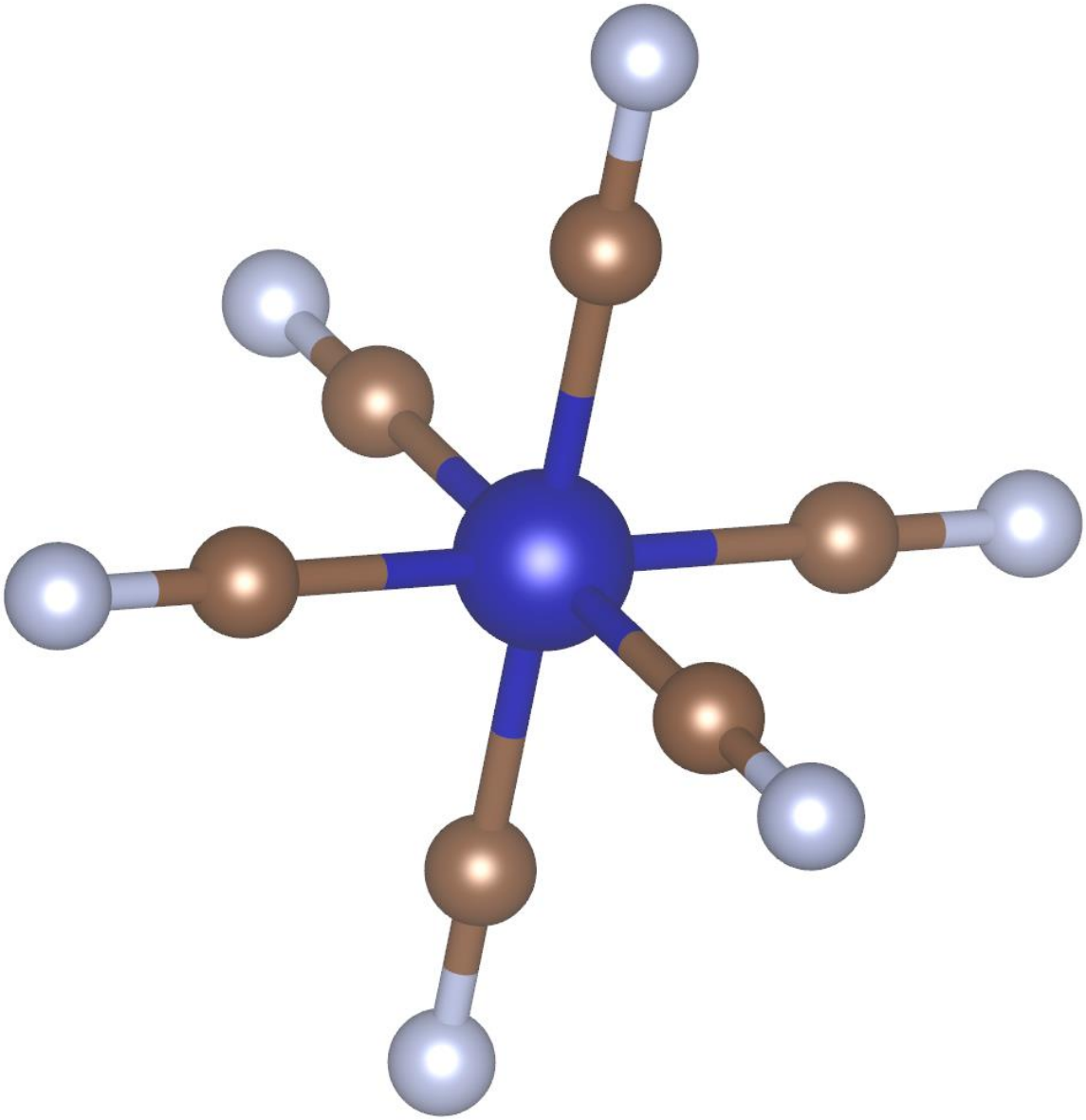

Figure B2: $Co(CN)_6^{4-}$, Hexacyanocobaltate.

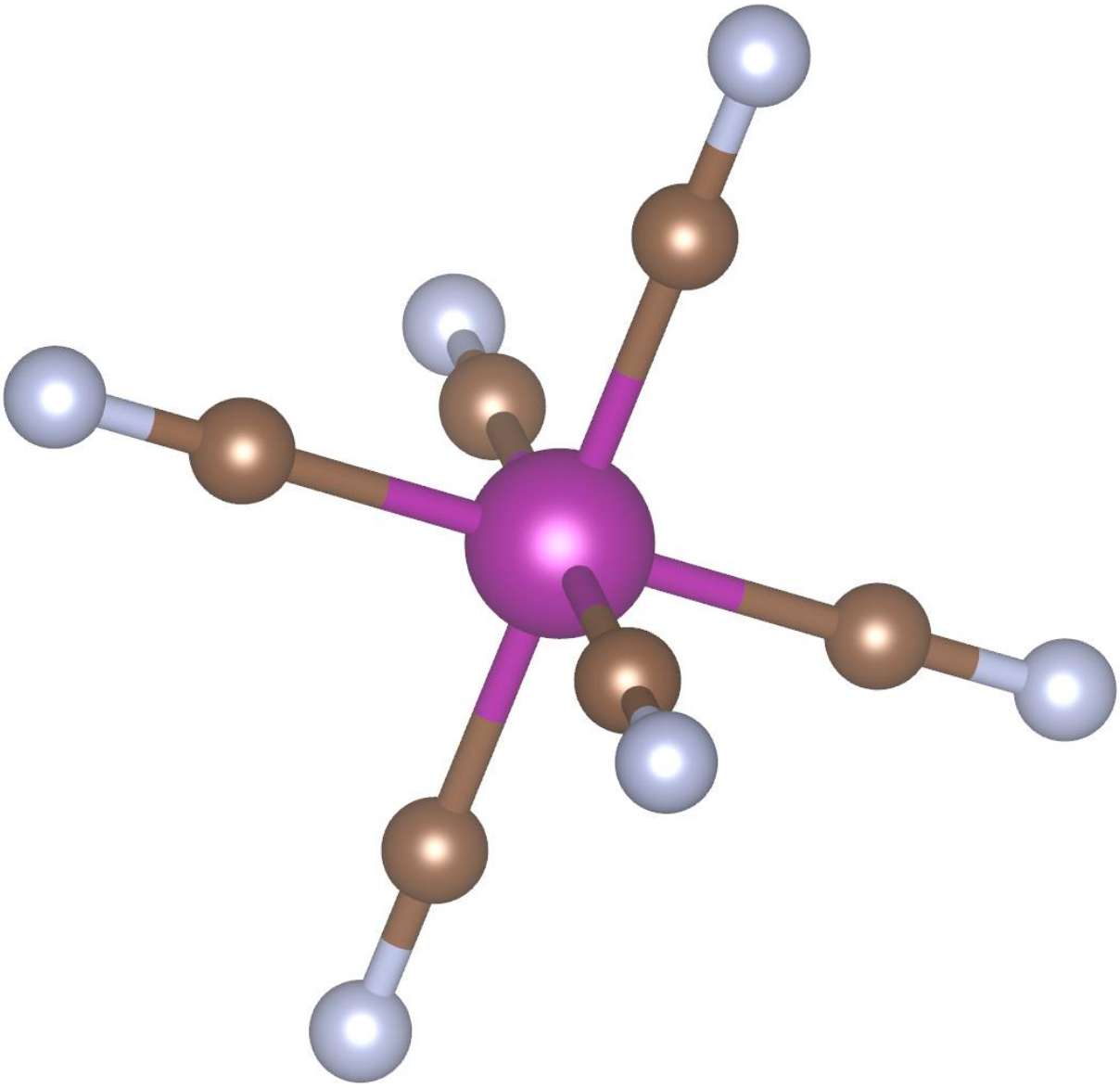

Figure B3: $Mn(CN)_6^{4-}$, Hexacyanomanganate.

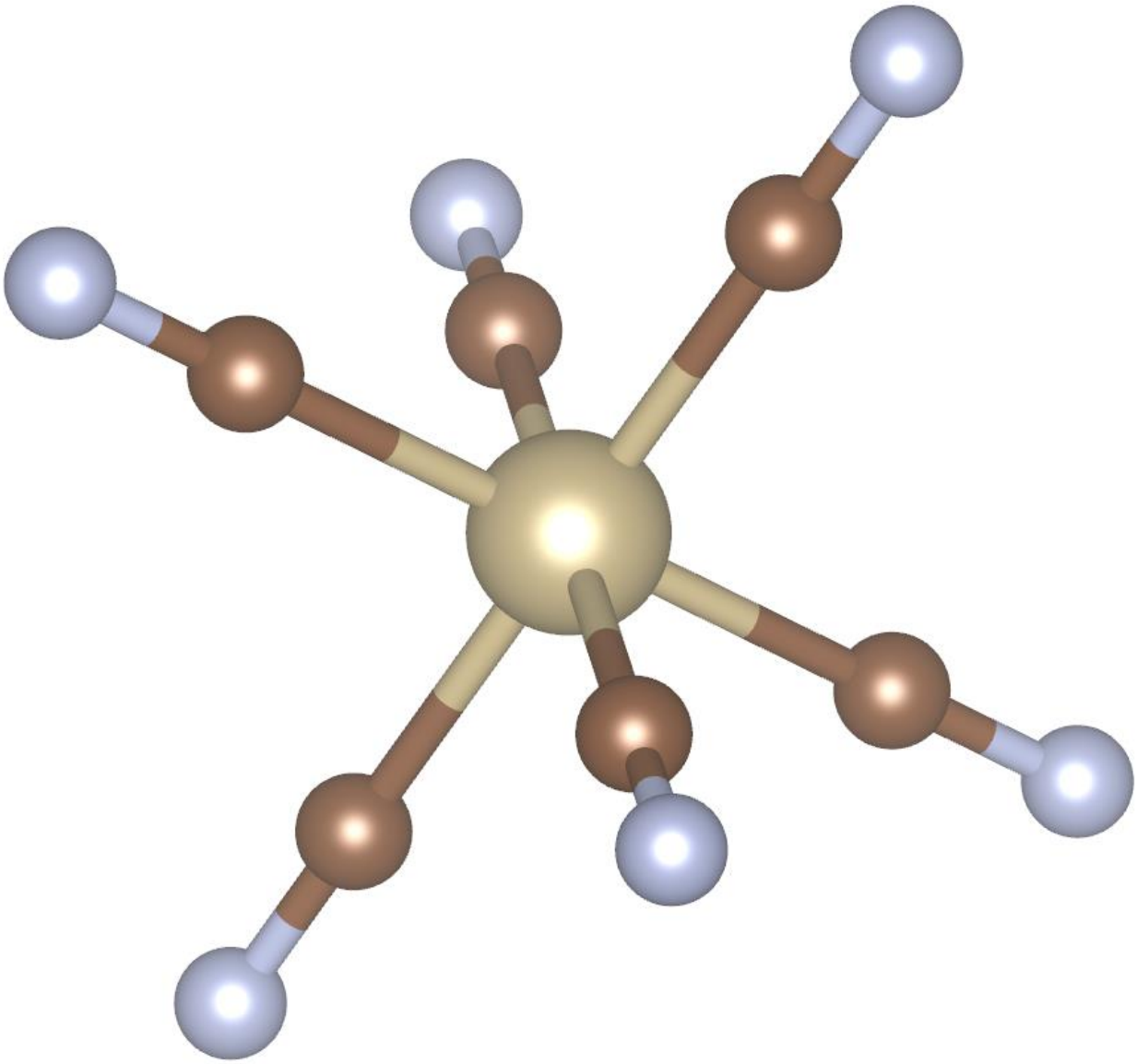

Figure B4: $Os(CN)_6^{4-}$, Hexacyanoosmiate.

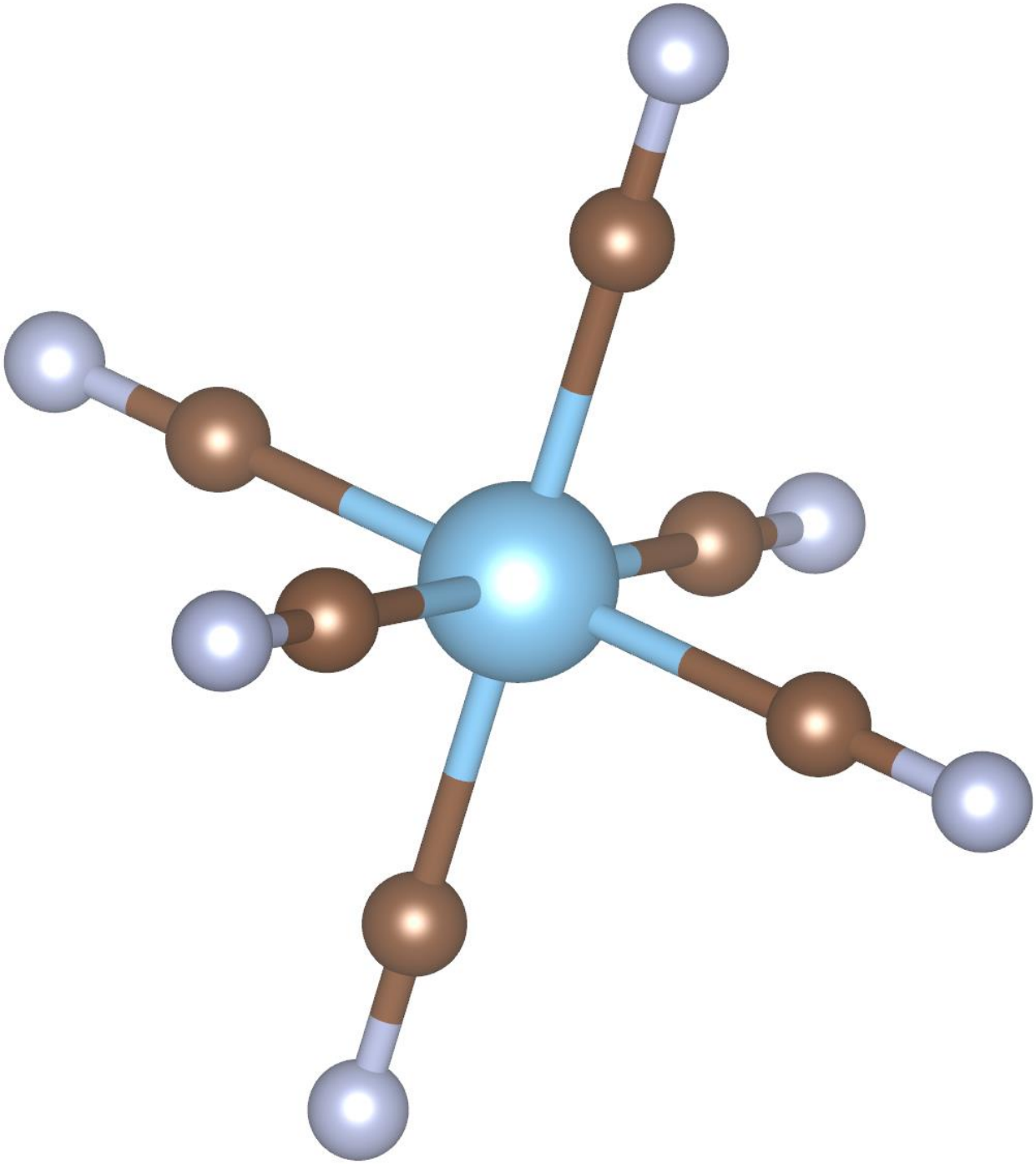

Figure B5: $Ti(CN)_6^{4-}$, Hexacyanotitanate.

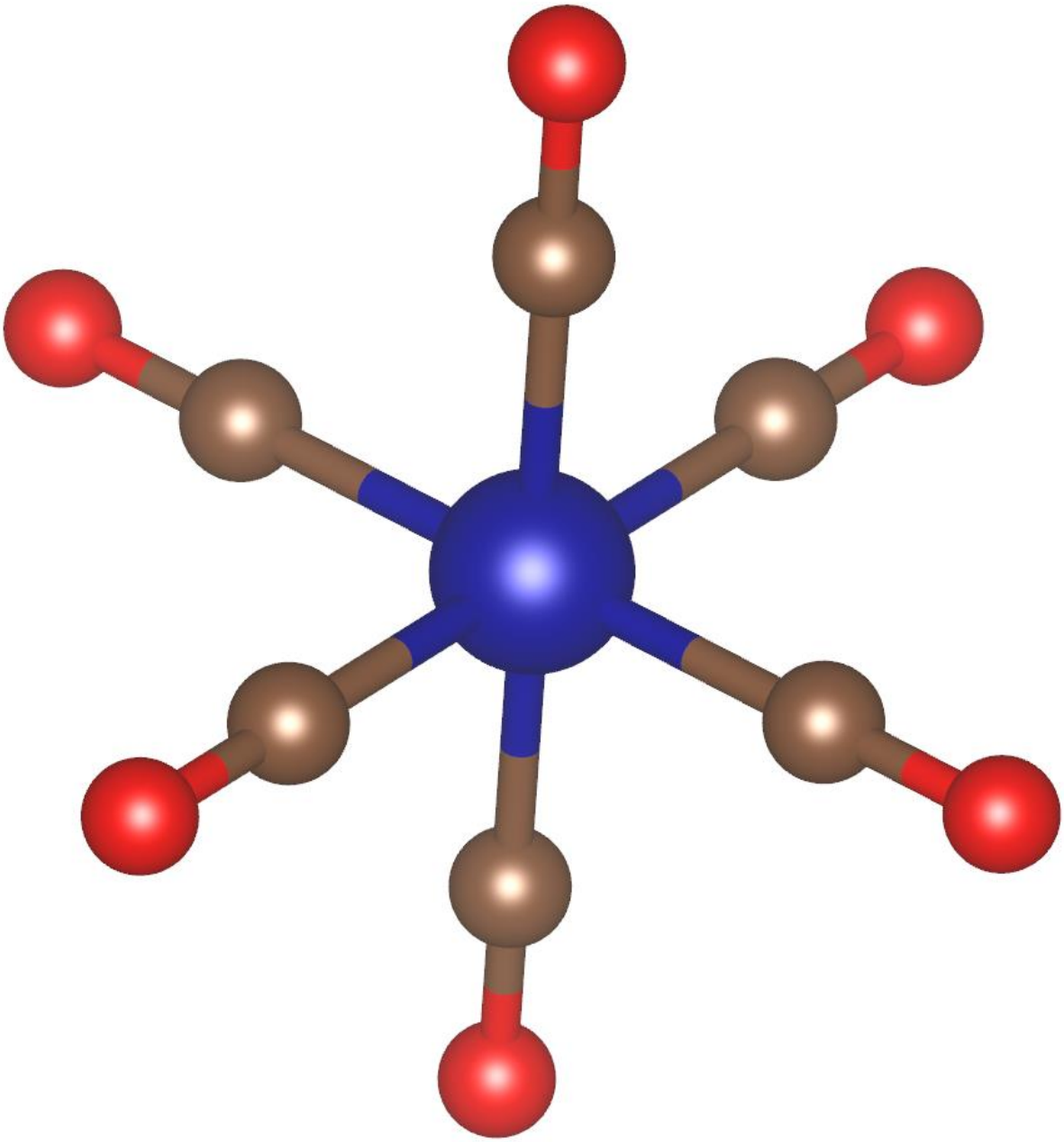

Figure B6: $Cr(CO)_6$, Chromium hexacarbonyl.

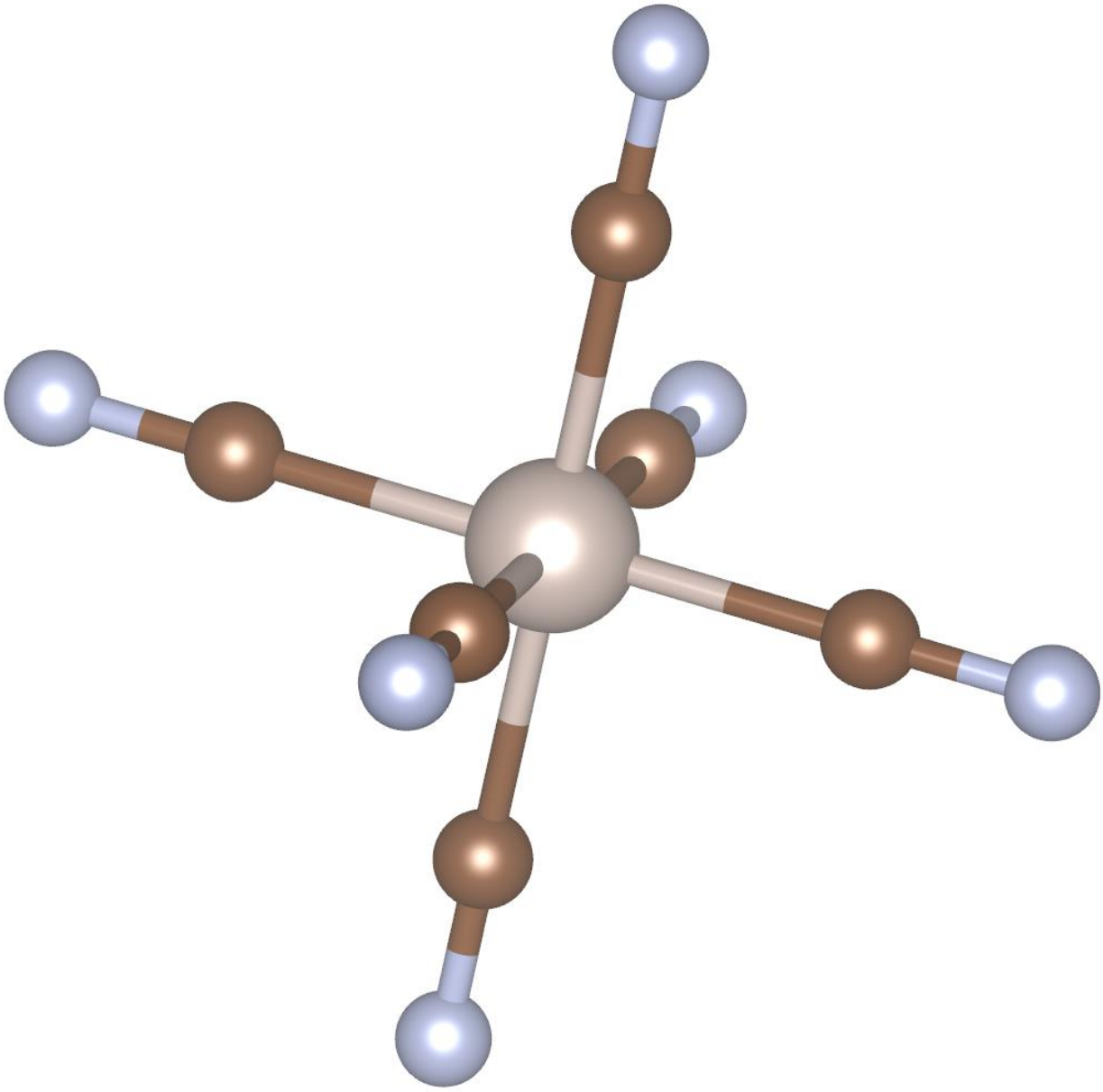

Figure B7: $Ru(CN)_6^{3-}$, Hexacyanoruthenate.

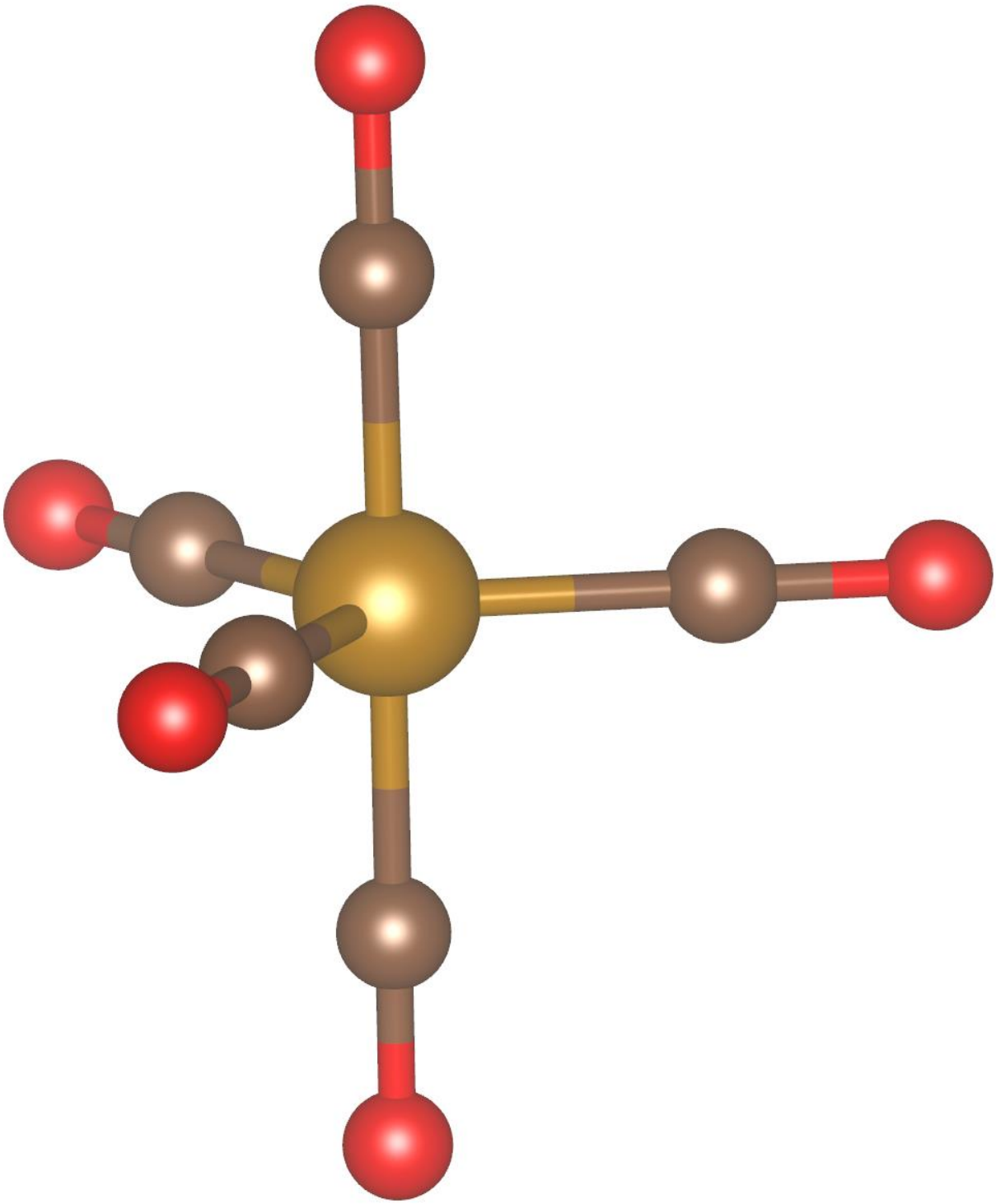

Figure B8: $Fe(CO)_5$, Iron pentacarbonyl.

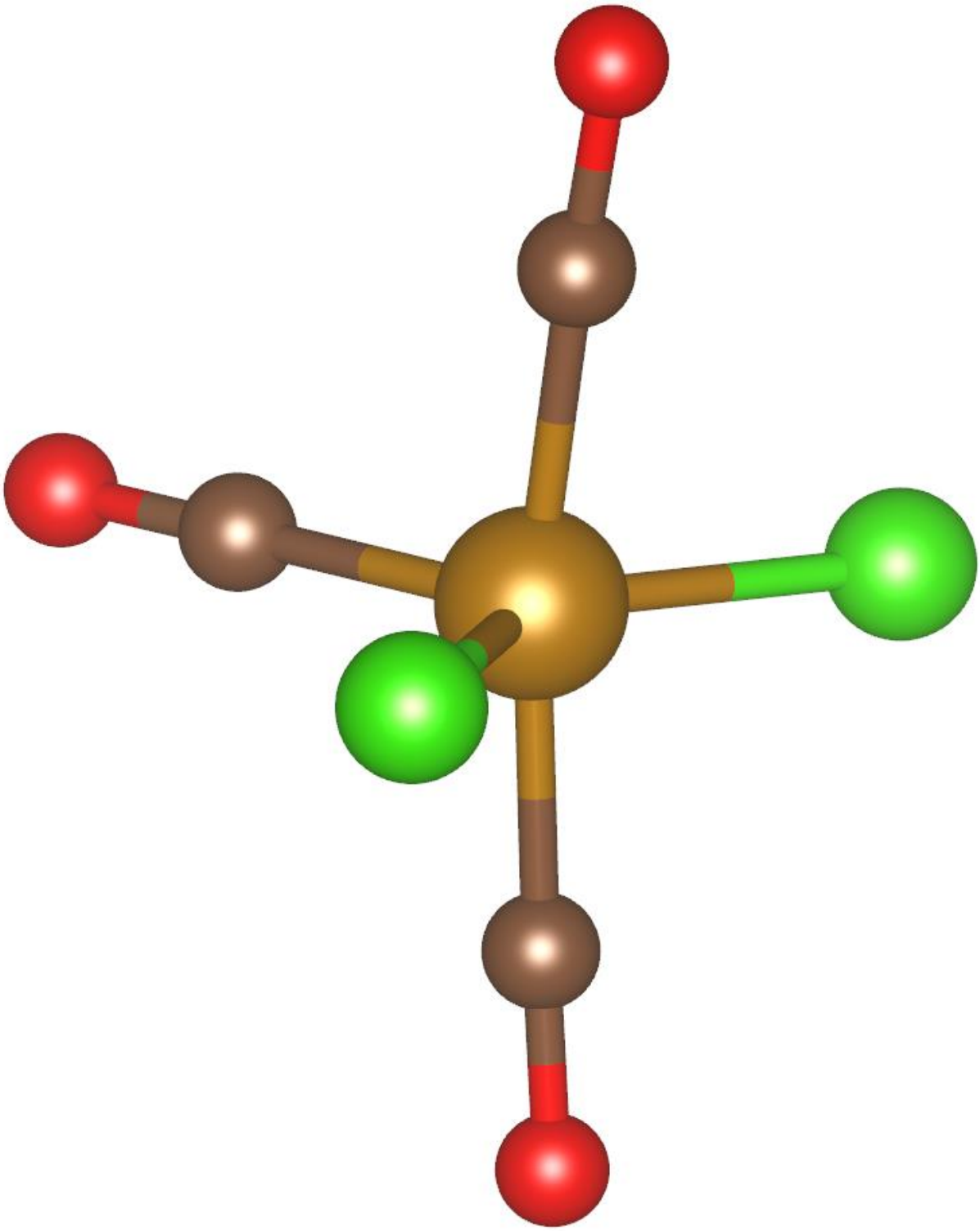

Figure B9: $Fe(CO)_3Cl_2$, Iron(II) tricarbonyl dichloride.

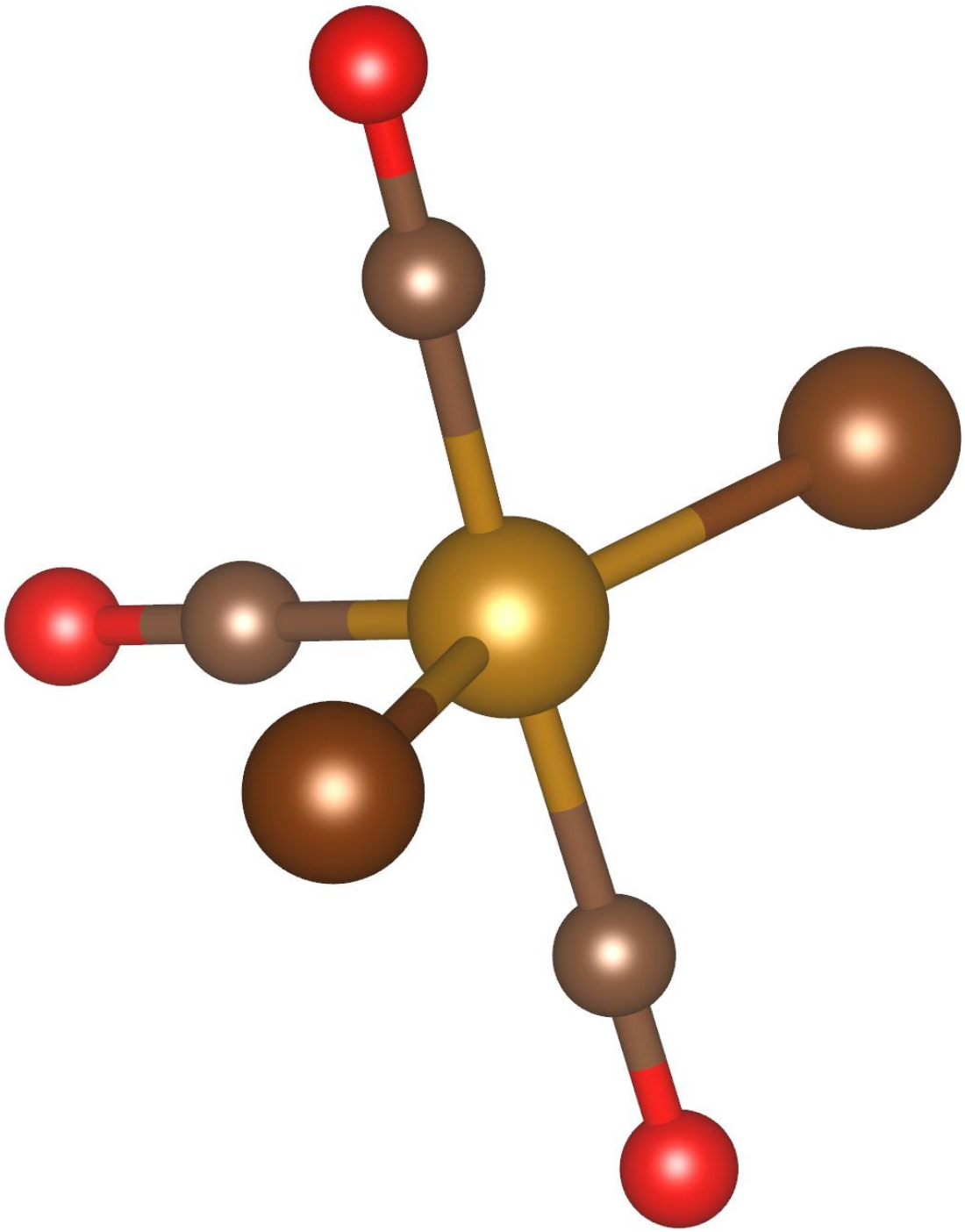

Figure B10: $Fe(CO)_3Br_2$, Iron(II) tricarbonyl dibromide.

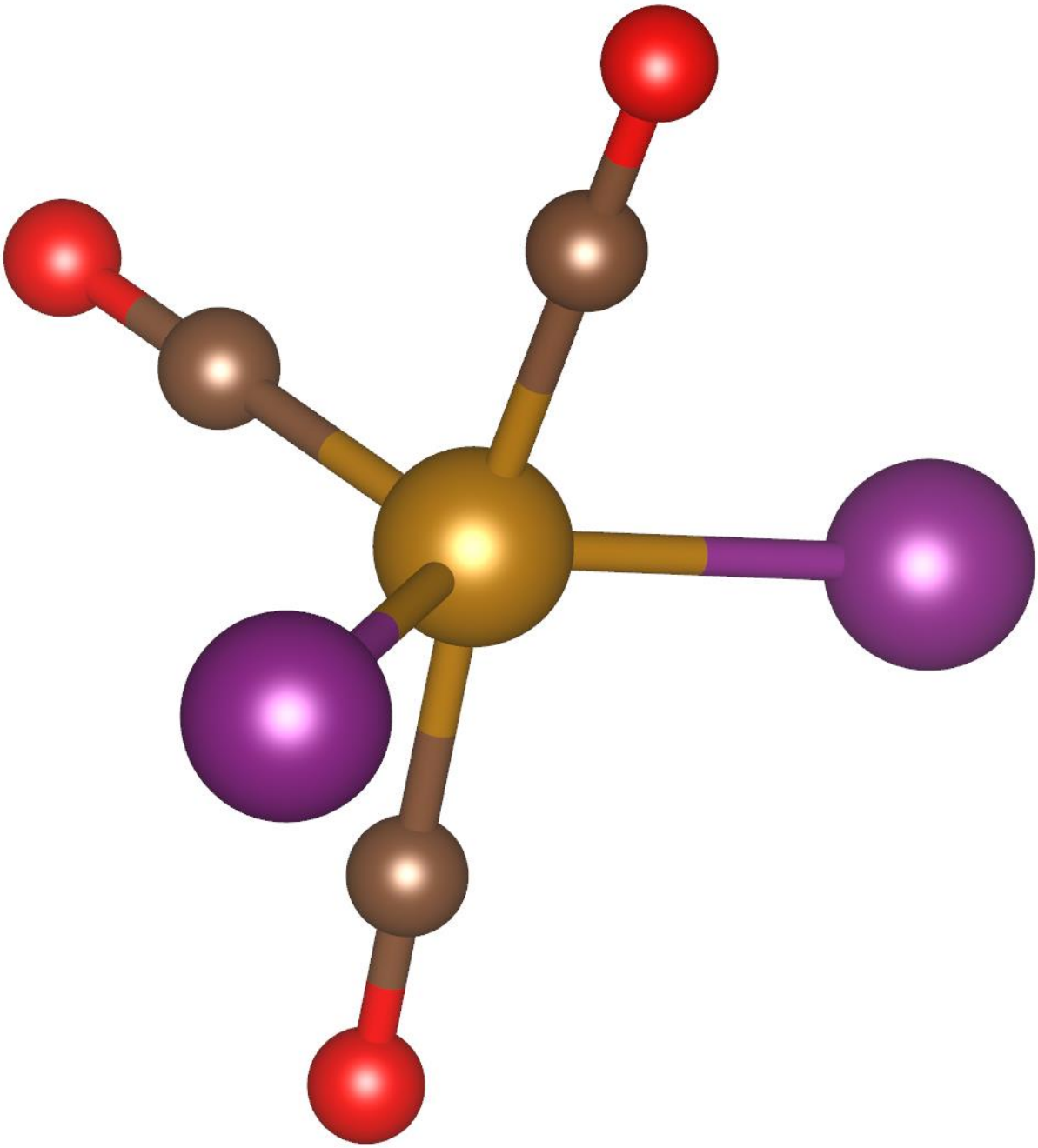

Figure B11: $Fe(CO)_3I_2$, Iron tricarbonyl diiodide.

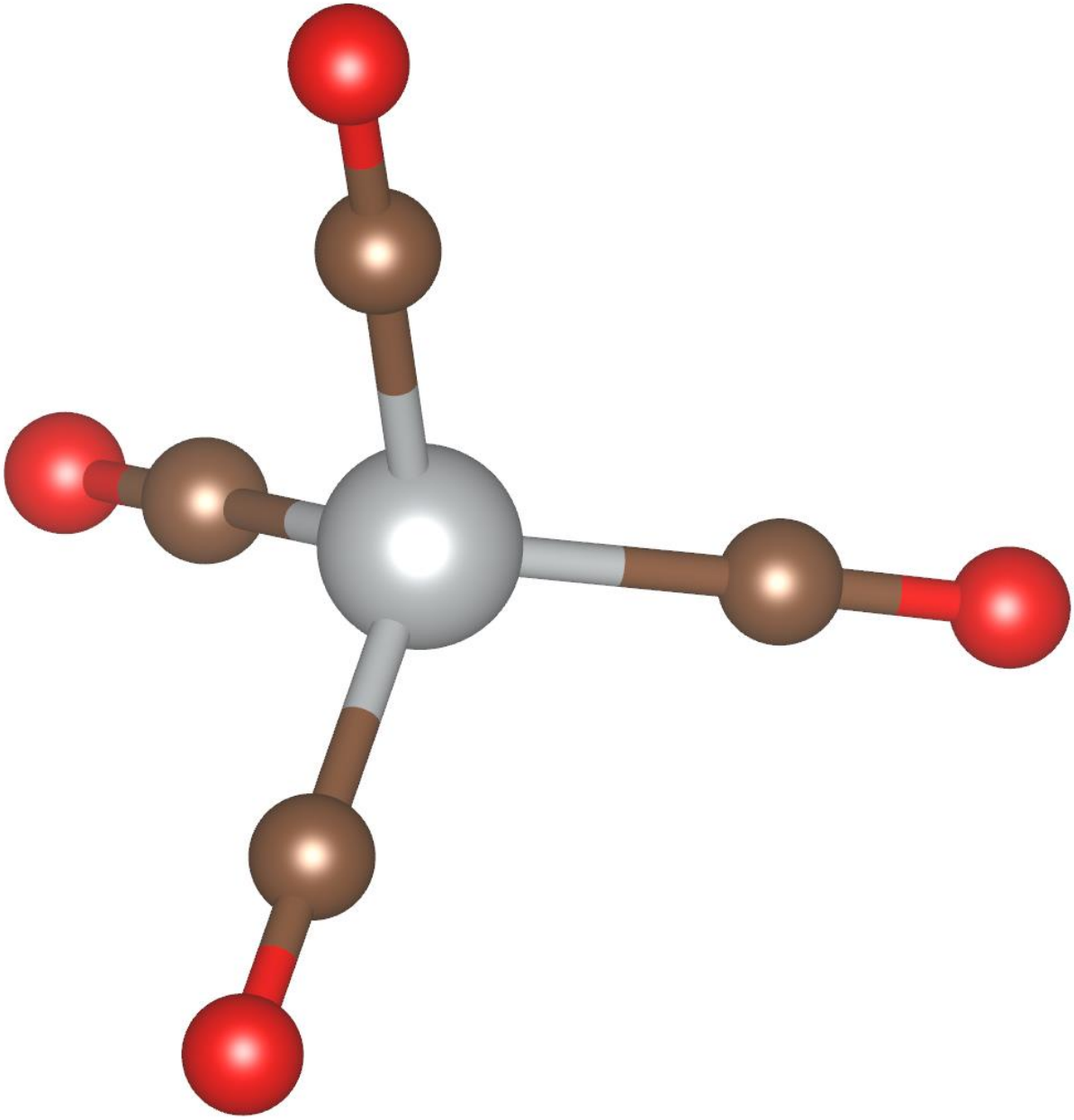

Figure B12: $Ni(CO)_4$, Nickel tetracarbonyl.

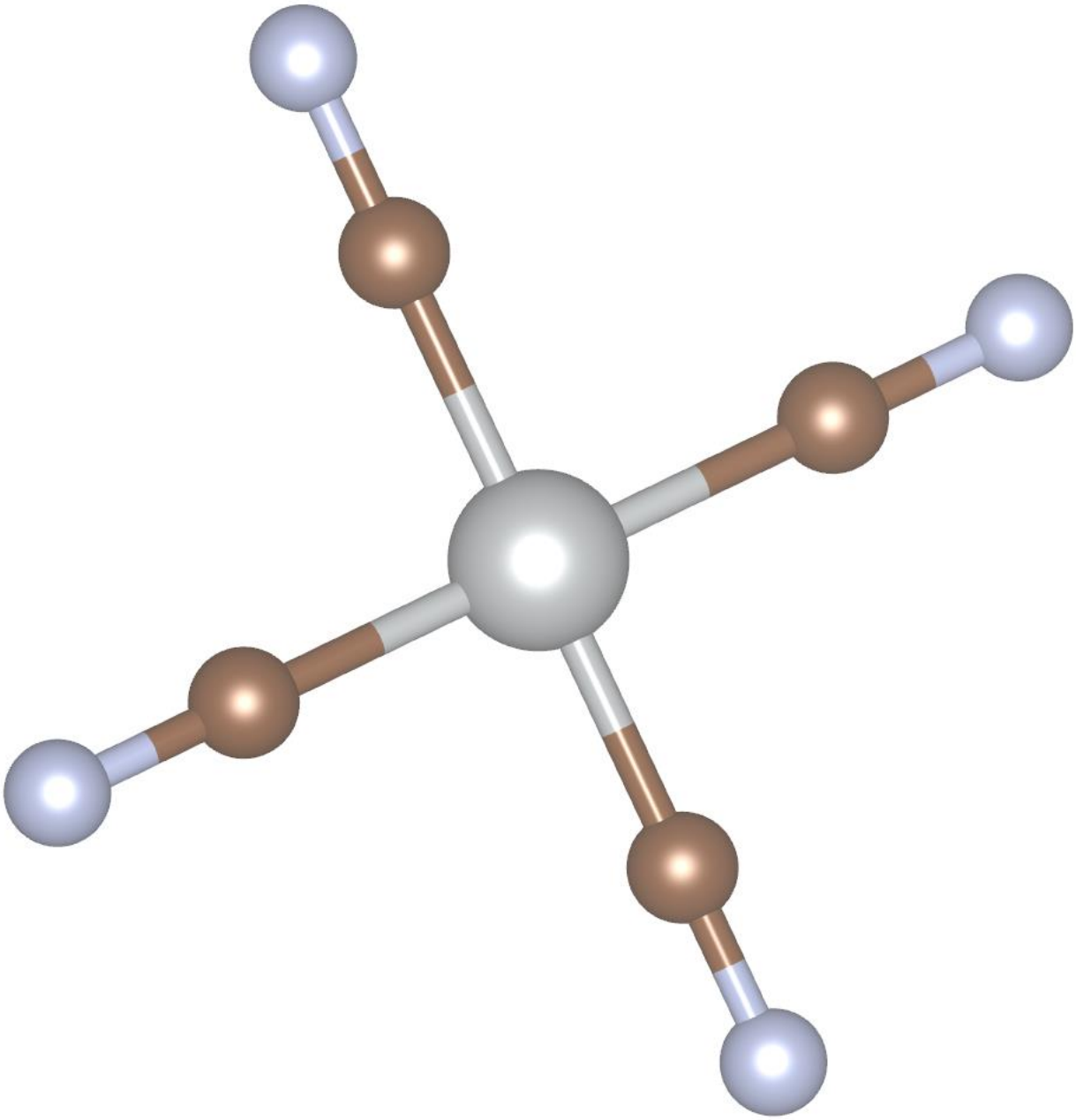

Figure B13: $Ni(CN)_4^{2-}$, Tetracyanonickelate.

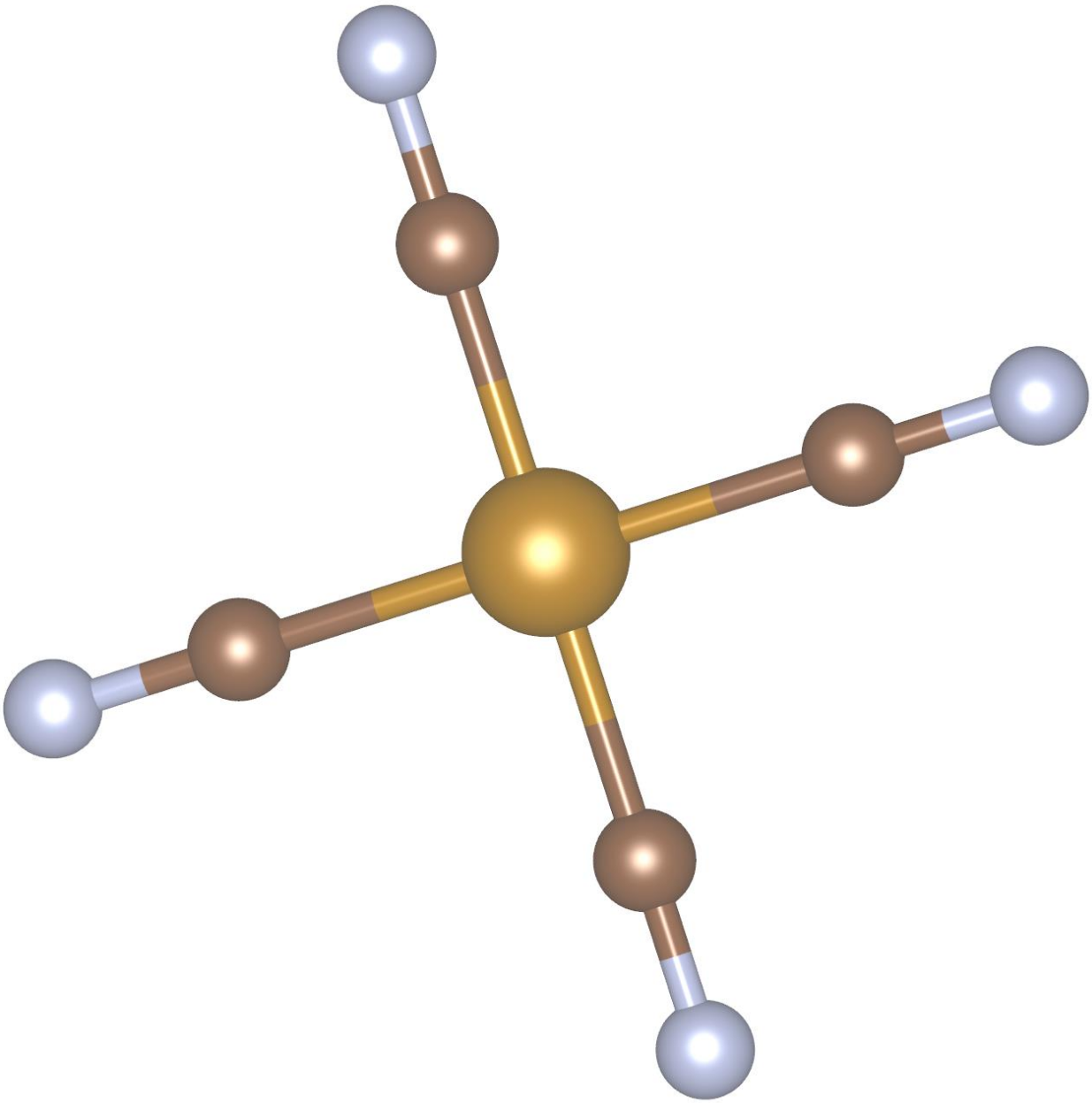

Figure B14: $Fe(CN)_4^{3-}$, Tetracyanoferrate.

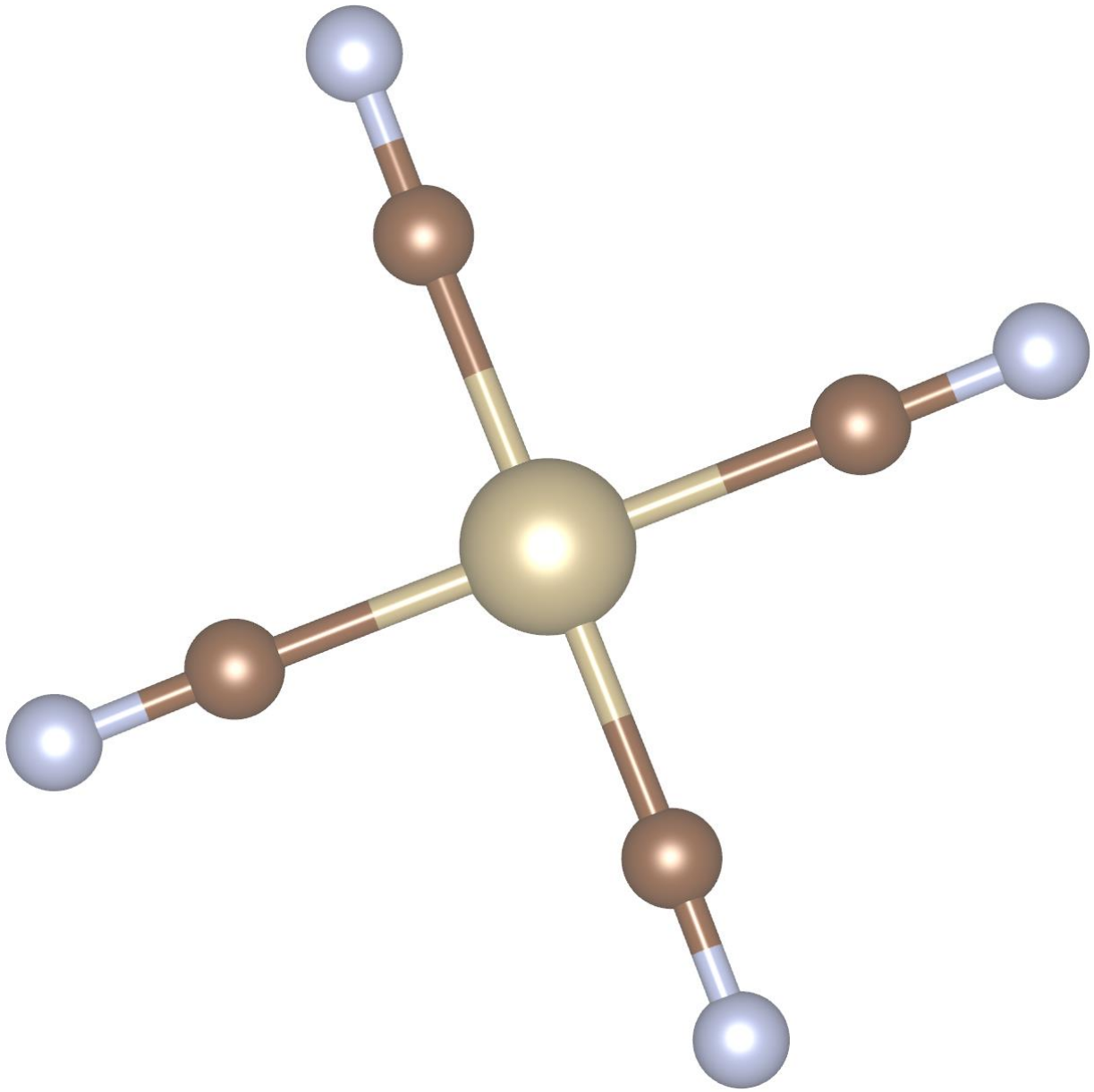

Figure B15: $Os(CN)_4^{3-}$, Tetracyanoosmiate.

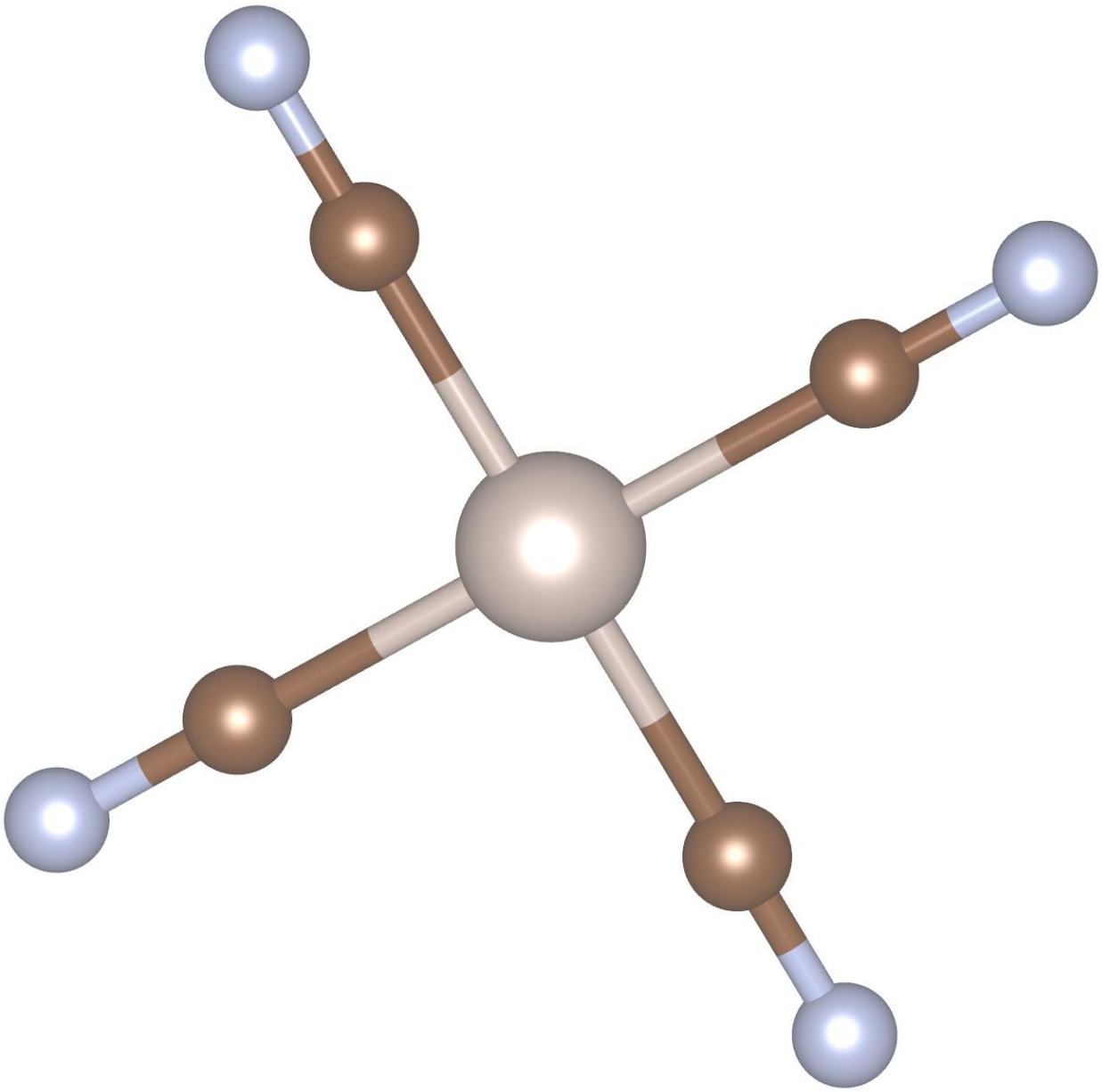

Figure B16: $Ru(CN)_4^{3-}$, Tetracyanoruthenate.

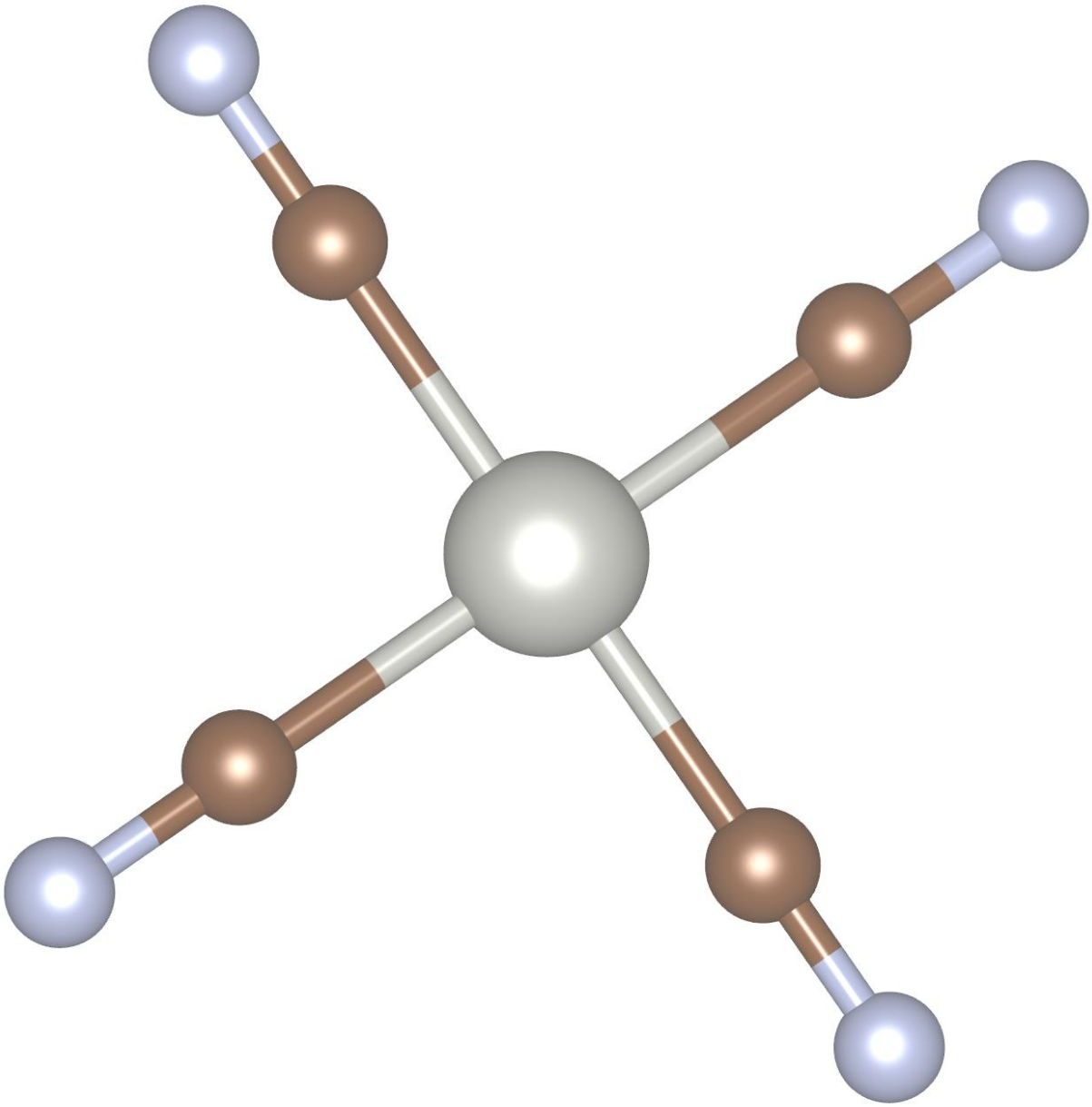

Figure B17: $Pd(CN)_4^{3-}$, Tetracyanopalladate.

Appendix C: Gas-Phase Density of States

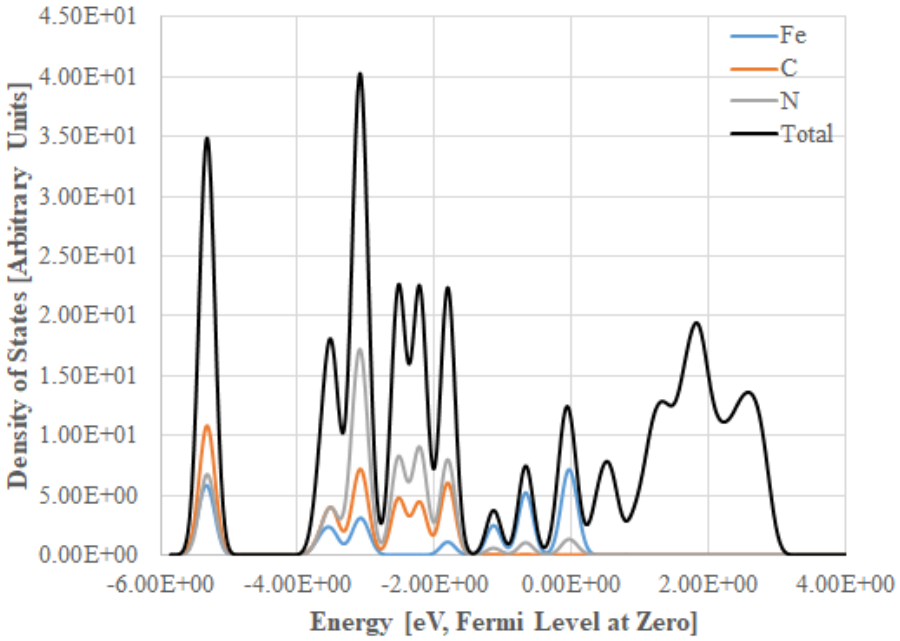

Figure C1: Calculated density of states for ferrocyanide, $Fe(CN)_6^{4-}$. Note the lack of gap between valence and conduction bands, which is clearly incorrect for a nonmetal.

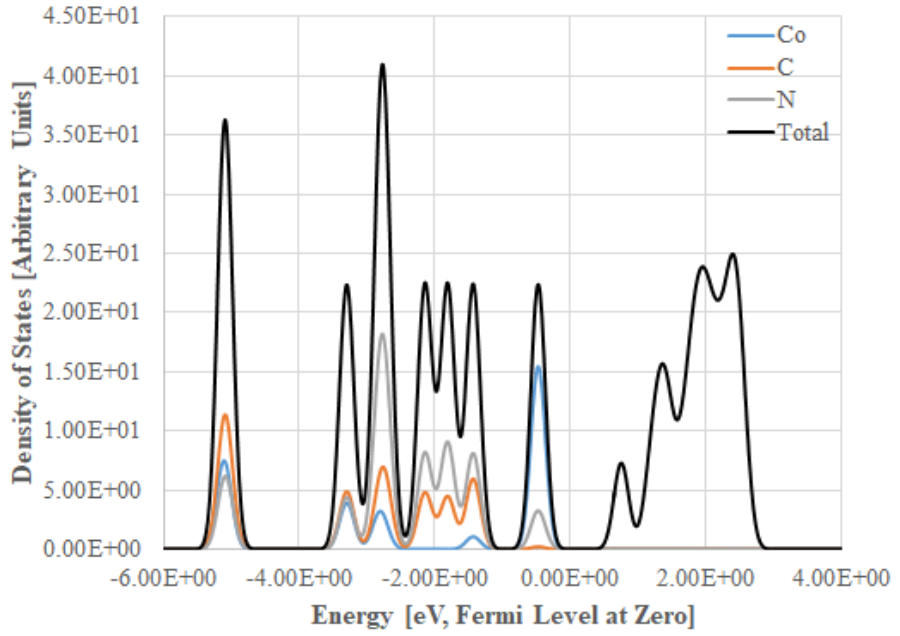

Figure C2: Calculated density of states for hexacyanocobaltate, $Co(CN)_6^{4-}$.

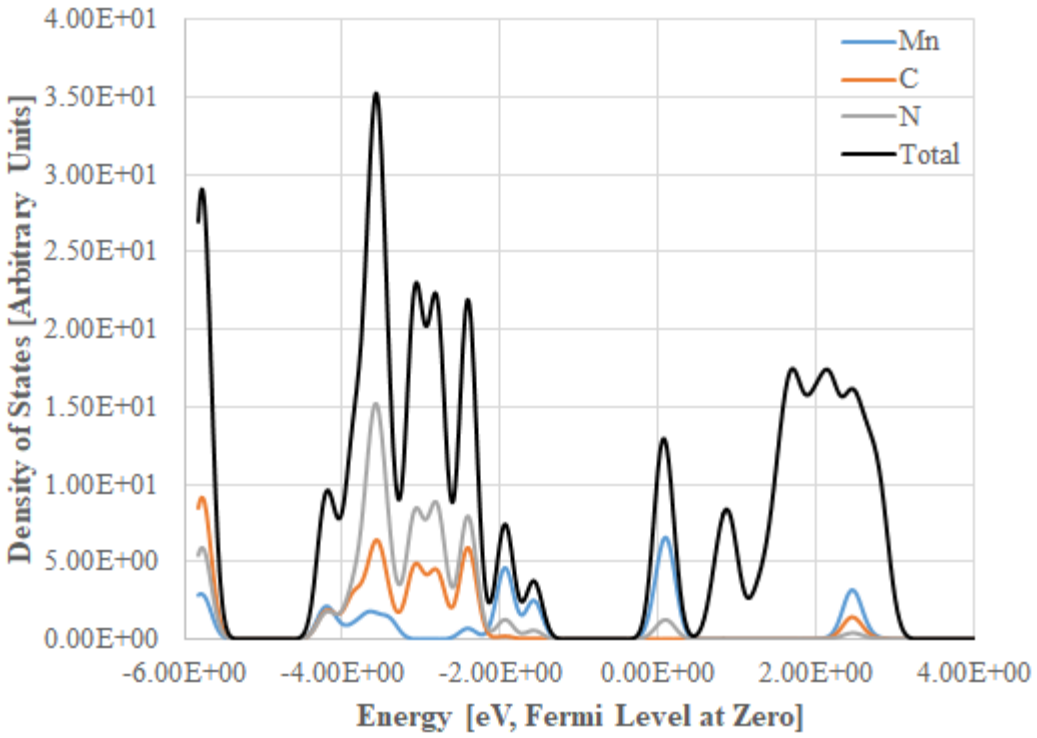

Figure C 3: Calculated density of states for hexacyanomanganate, $Mn(CN)_6^{4-}$. Note the lack of gap between valence and conduction bands, which is clearly incorrect for a nonmetal.

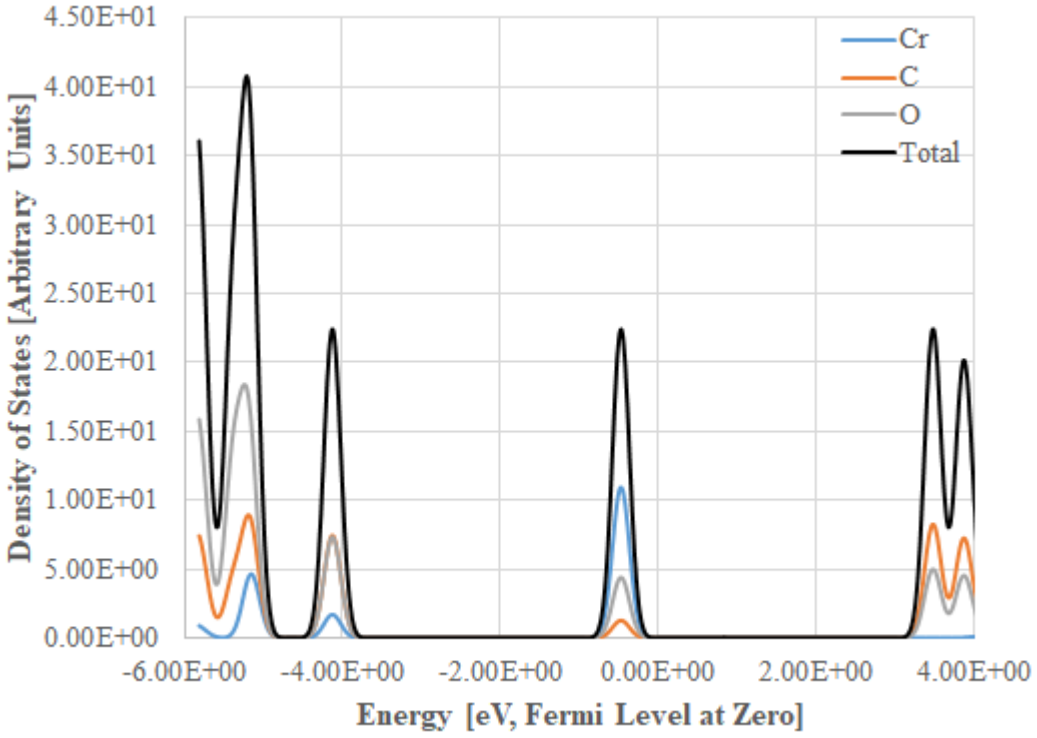

Figure C4: Calculated density of states for chromium hexacarbonyl, $Cr(CO)_6$.

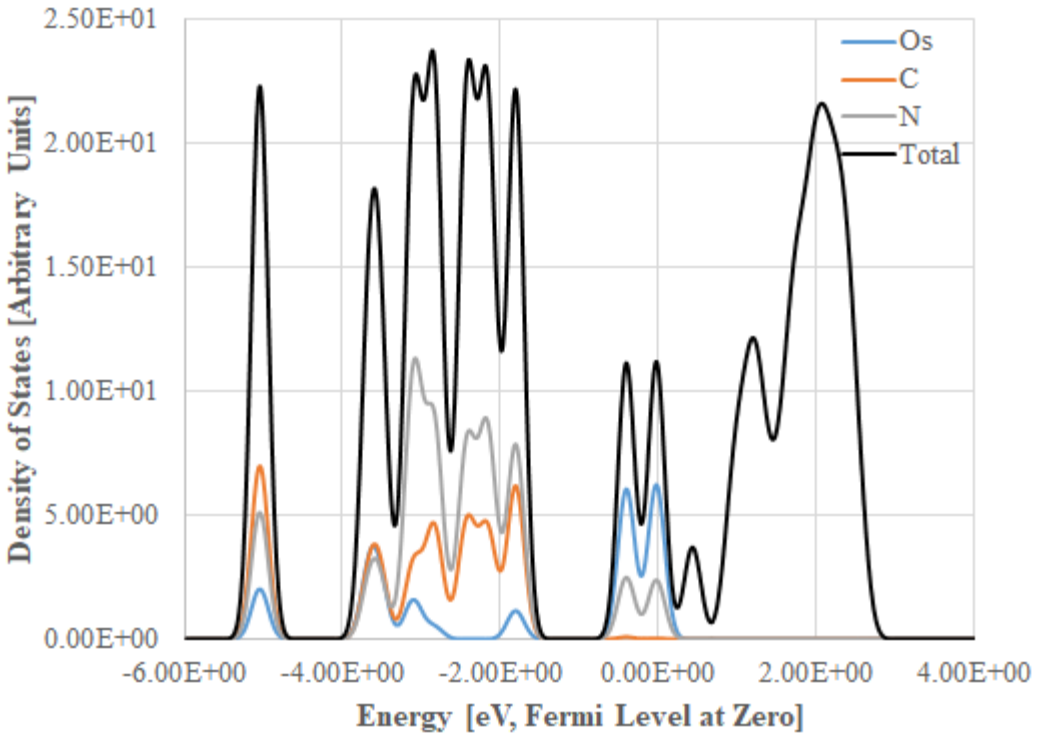

Figure C5: Calculated density of states for hexacyanoosmiate, $Os(CN)_6^{3-}$. Note the lack of gap between valence and conduction bands, which is clearly incorrect for a nonmetal.

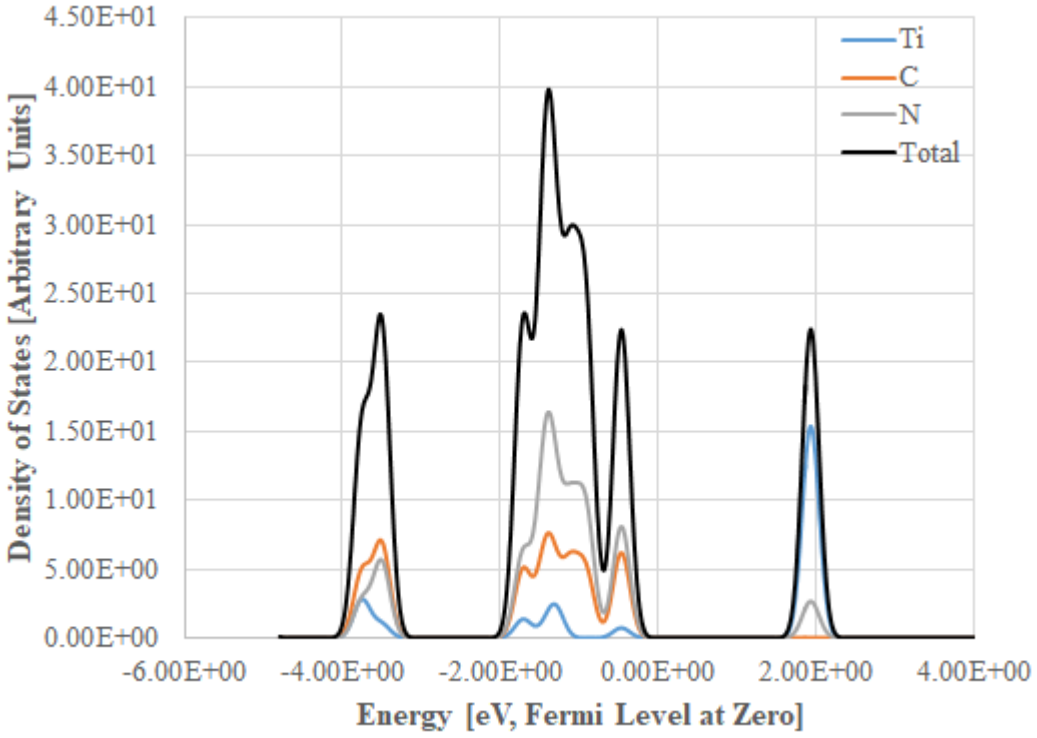

Figure C6: Calculated density of states for hexacyanotitanate, $Ti(CN)_6^{2-}$.

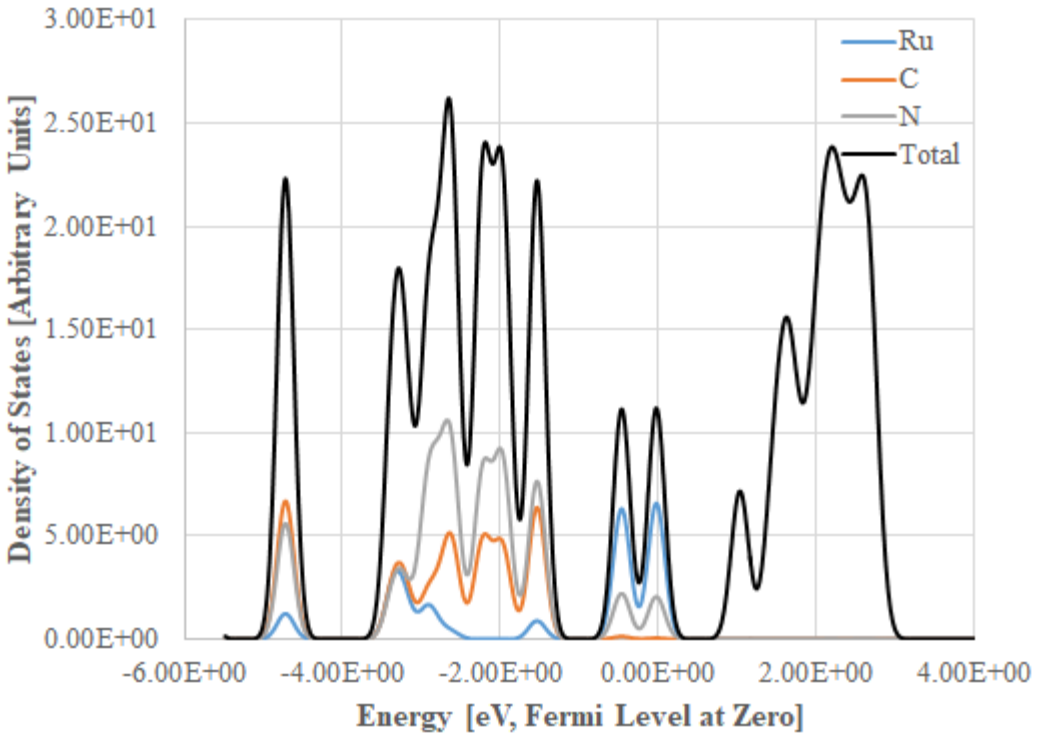

Figure C7: Calculated density of states for hexacyanoruthenate, $Ru(CN)_6^{4-}$. Note the lack of gap between valence and conduction bands, which is clearly incorrect for a nonmetal.

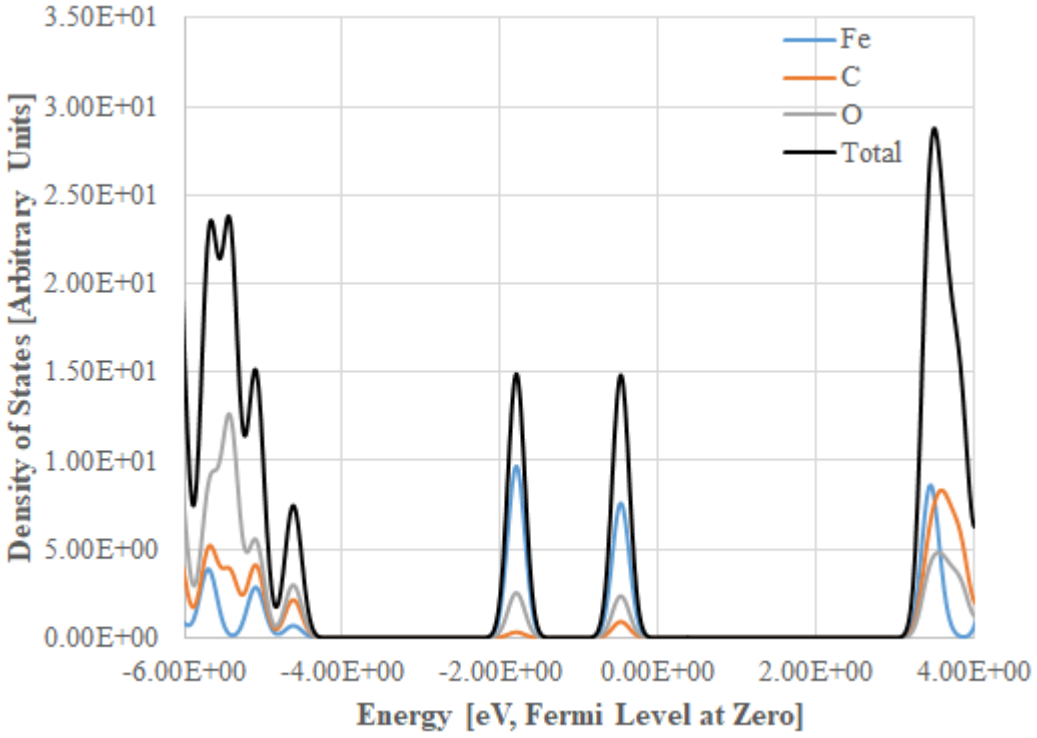

Figure C8: Calculated density of states for iron pentacarbonyl, $Fe(CO)_5$.

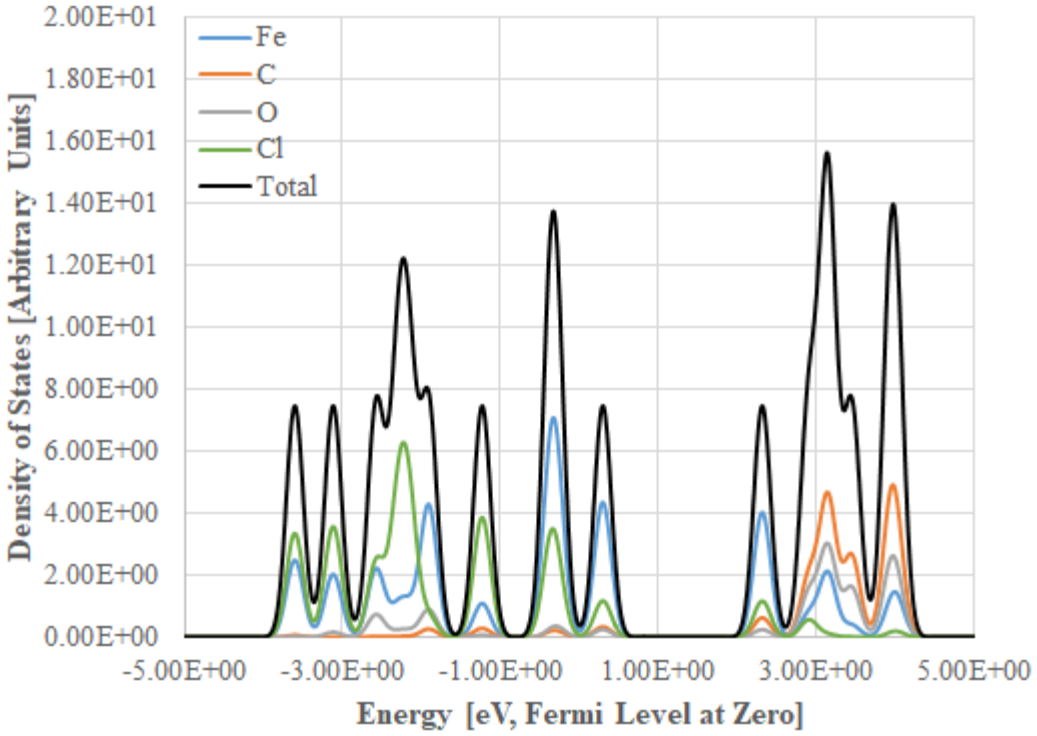

Figure C9: Calculated density of states for iron(II) tricarbonyl dichloride, $Fe(CO)_3Cl_2$. Note the lack of gap between valence and conduction bands, which is clearly incorrect for a nonmetal.

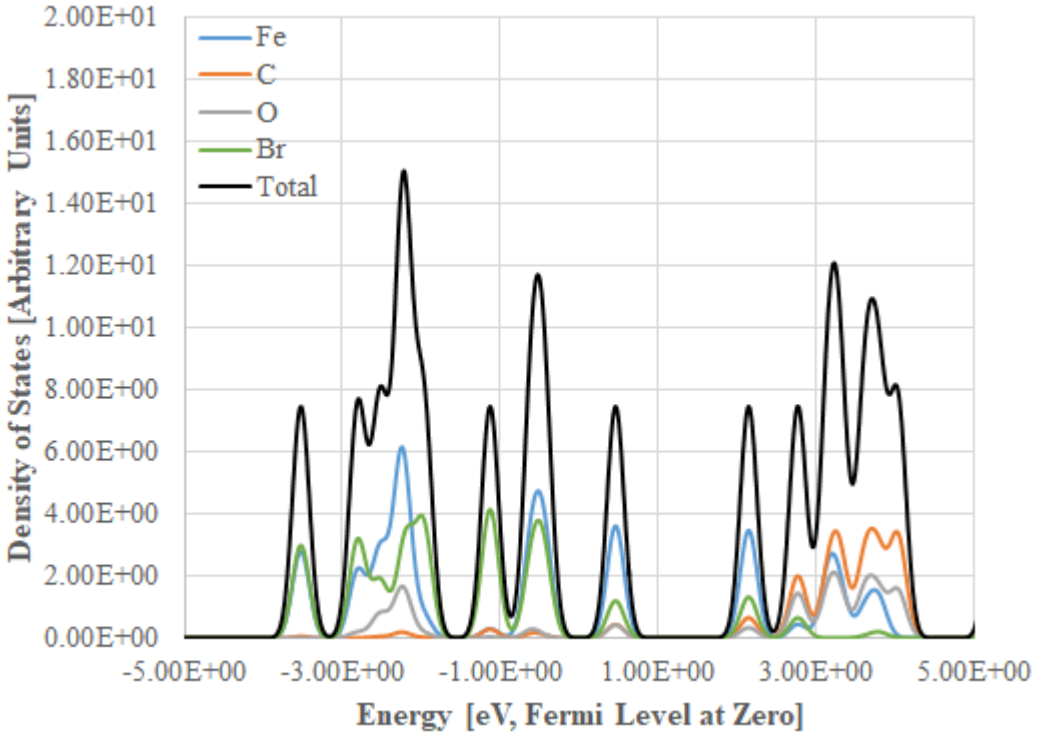

Figure C10: Calculated density of states for iron(II) tricarbonyl dibromide, $Fe(CO)_3Br_2$.

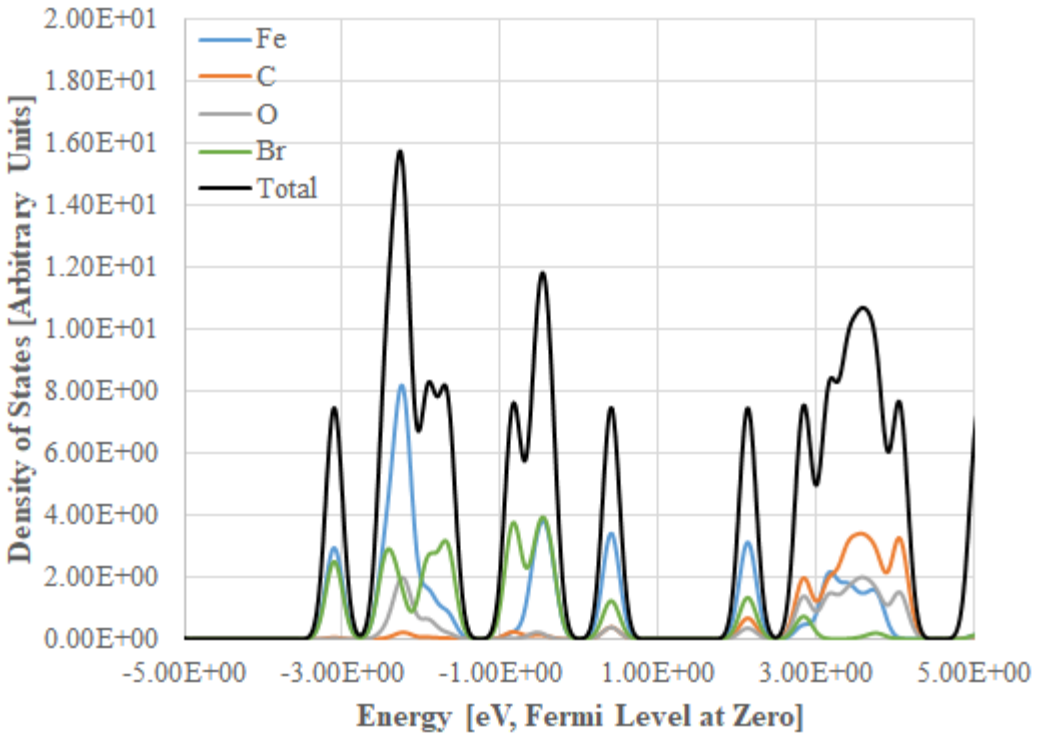

Figure C11: Calculated density of states for iron(II) tricarbonyl diiodide, $Fe(CO)_3I_2$.

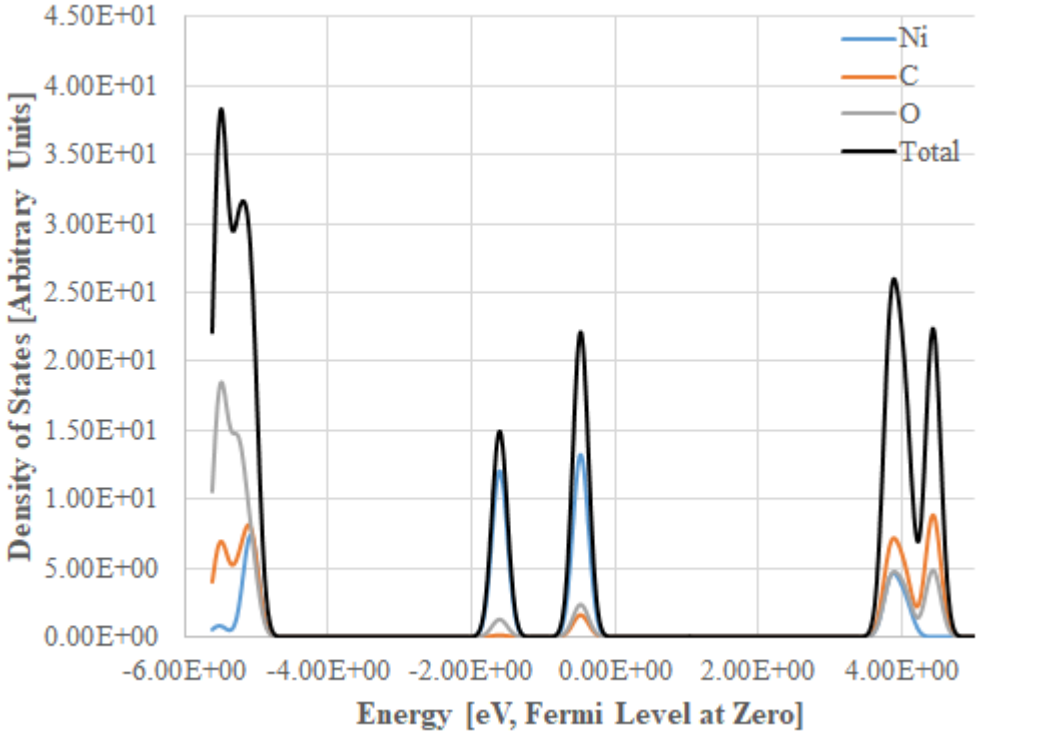

Figure C12: Calculated density of states for nickel tetracarbonyl, $Ni(CO)_4$.

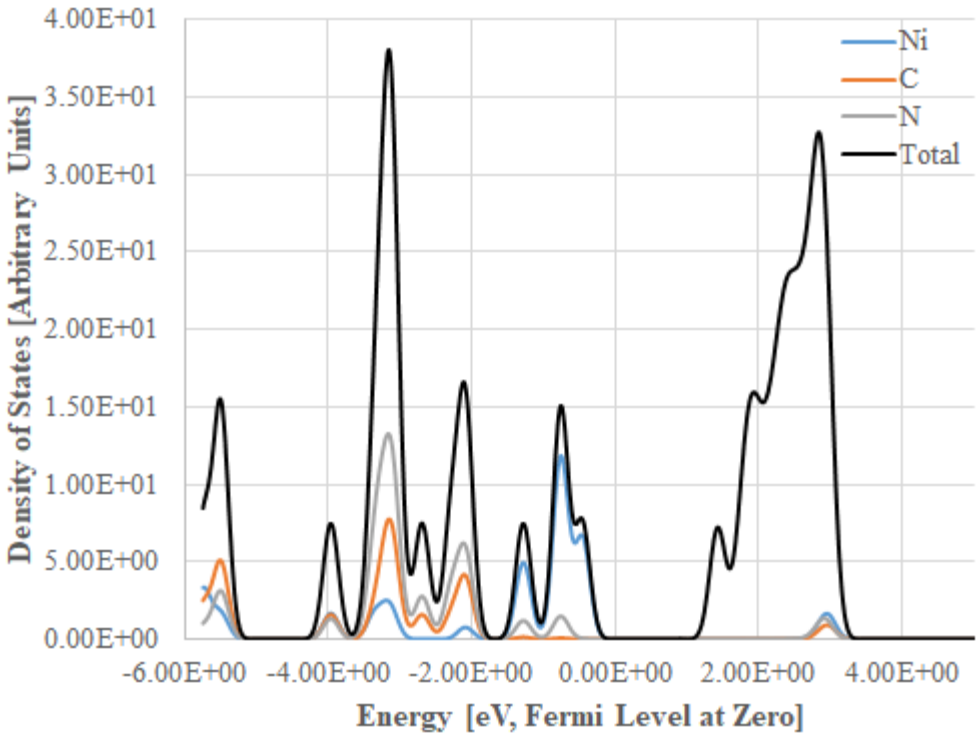

Figure C13: Calculated density of states for tetracyanonickelate, $Ni(CN)_4^{2-}$.

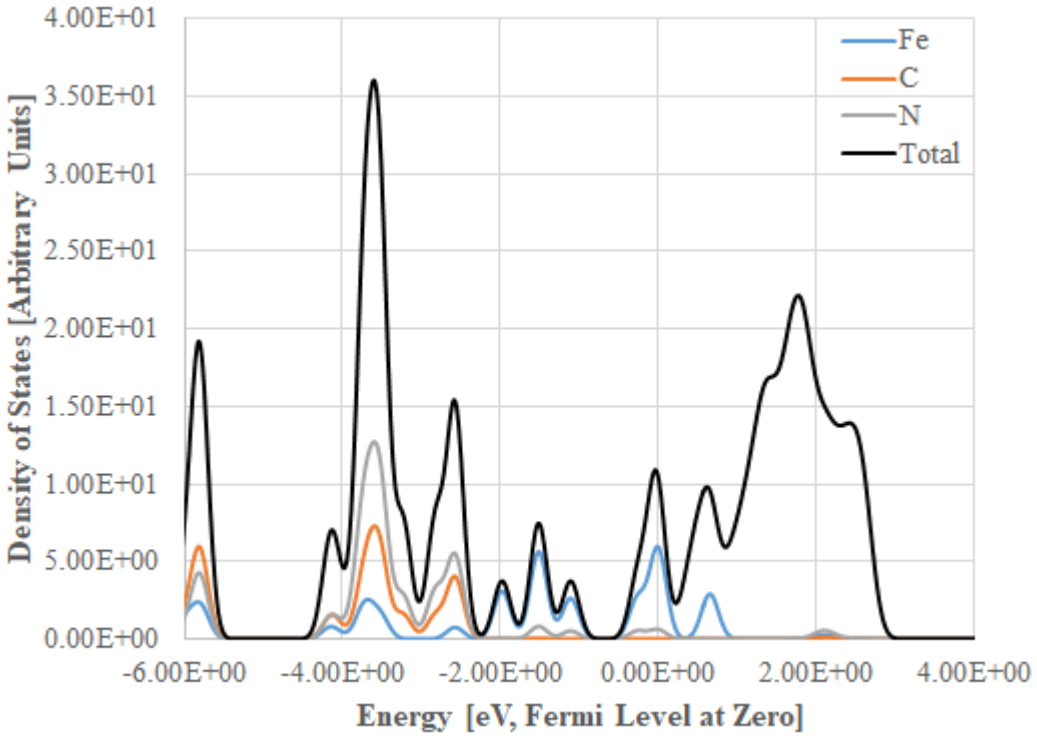

Figure C14: Calculated density of states for tetracyanoferrate, $Fe(CN)_4^{3-}$. Note the lack of gap between valence and conduction bands, which is clearly incorrect for a nonmetal.

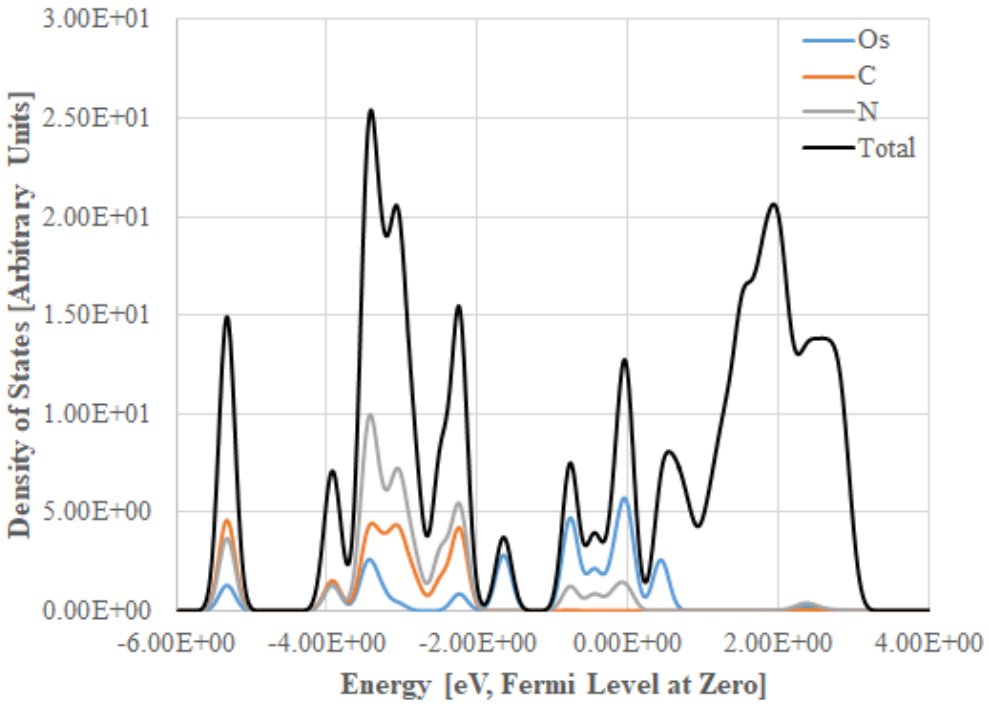

Figure C15: Calculated density of states for tetracyanoosmiate, $Os(CN)_4^{3-}$. Note the lack of gap between valence and conduction bands, which is clearly incorrect for a nonmetal.

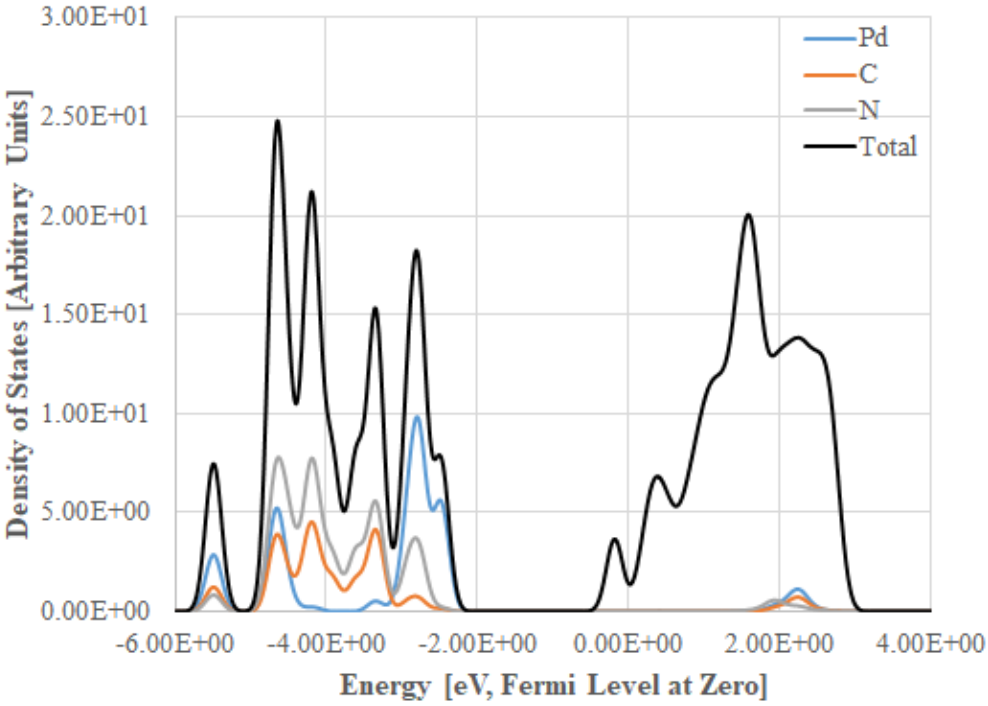

Figure C16: Calculated density of states for tetracyanopalladate, $Pd(CN)_4^{3-}$. Note the lack of gap between valence and conduction bands, which is clearly incorrect for a nonmetal.

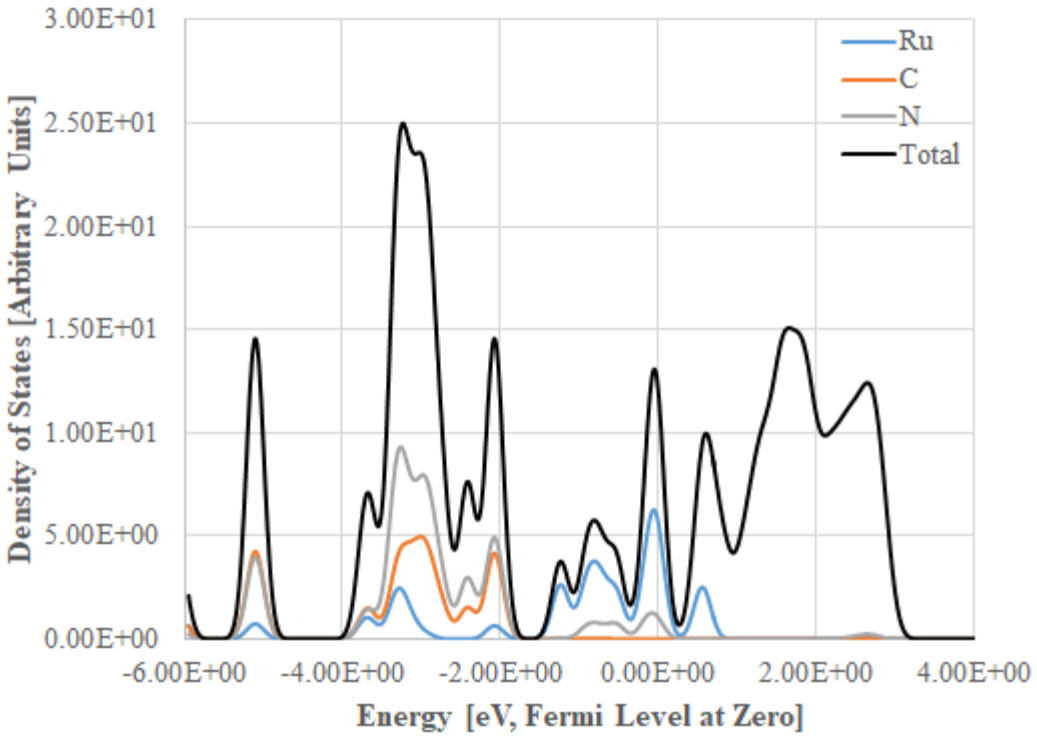

Figure C17: Calculated density of states for tetracyanoruthenate, $Ru(CN)_4^{3-}$. Note the lack of gap between valence and conduction bands, which is clearly incorrect for a nonmetal.